MEASUREMENTS OF FROST GROWTH ON LOUVERED FOLDED FINS OF MICROCHANNEL HEAT EXCHANGERS

By

TOMMY HONG

Bachelor of Science in Mechanical Engineering

Oklahoma State University

Stillwater, Oklahoma

2009

Submitted to the Faculty of the
Graduate College of the
Oklahoma State University
in partial fulfillment of
the requirements for
the Degree of
MASTER OF SCIENCE
December, 2011

MEASUREMENTS OF FROST GROWTH ON LOUVERED FOLDED FINS OF MICROCHANNEL HEAT EXCHANGERS

Thesis Approved:

Dr. Lorenzo Cremaschi

Thesis Adviser

Dr. Daniel E. Fisher

Dr. David G Lilley

Dr. Mark E. Payton

Dean of the Graduate College

TABLE OF CONTENTS

Chapter Page

LIST OF TABLES

Table Page

LIST OF FIGURES

Figure Page

CHAPTER I

INTRODUCTION TO MICROCHANNEL HEAT EXCHANGER

1.1 INTRODUCTION

In recent years, people have become more concern about issues related to global warming. Couples of methods are used to reduce the global warming are to develop more and more green technologies reducing the current energy consumption. The development and implementation of green technologies are currently beyond the reach due to the issue with reliability and expensive production cost. Alternately, a feasible way to reduce the effect of global warming is to improve the efficiency of current equipment.

In the residential sector, most of the energy consumption is used for space heating and cooling. One of the most commonly utilized HVAC units is air source heat pump. HVAC manufacturers are constantly aiming to improve the efficiency of their products, including heat pump units. There are couples of ways to improve heat pump unit, and the use of microchannel is one of the highly anticipated solutions known to the manufacturers. Microchannel heat exchanger has the potential to improve the performance and reduce the production cost.

The advantages of utilizing microchannel heat exchanger compared to conventional heat exchanger are as follows:

- Higher overall heat transfer coefficient
- Reduction in refrigerant charge
- Decrease the overall size of the unit
- Reduction in production cost

1.2 BACKGROUND

Microchannel heat exchangers have the potential to significantly improve the performance of air conditioning, refrigeration, and heat pump systems. The benefits of microchannel heat exchangers in air conditioning systems have been shown by numerous studies in the literature (Kim and Bullard 2002b, a; Garimella 2003; Jacobi et al. 2005). Because of their compactness and efficiency for heat exchange, microchannel heat exchangers have been recently adopted by the heat pump industry for residential and commercial applications. The use of these heat exchangers as evaporator in outdoor coil has subjected them to significant frost growth and frequent defrost cycles, which ultimately limit their heating performance during winter season (Kim and Groll 2003; Xia et al. 2006; Padhmanabhan et al. 2008).

Frosting is a transient phenomenon in which both heat transfer and mass transfer simultaneously take place. Causes by the low conductive thermal resistance of microchannel tubes, the fin base temperature is close to the local saturation temperature of the refrigerant and a larger temperature difference between air and fin surface occurs in microchannel heat exchangers. The augmented heat transfer rate of the microchannel heat exchanger is beneficial for high heating capacity during heating period. However, the compactness of the microchannels due to the folded fins, low fin temperature, and the fin surface characteristics might make them more vulnerable to early frost formation and rapid frost growth. The effective heating service time experienced by a heat pump unit with a microchannel outdoor coil is significantly reduced because of the air flow blockage caused by the frost. The unanimous consensus among researchers is that the design of folded fin used at microchannel heat exchangers for evaporator outdoor coils of heat pump systems must consider both steady state and transient performance under frosting conditions.

1.3 REPORT ORGANIZATION

This thesis is divided into a total of eight chapters that covers introduction, literature review, objective and scope of work, the experimental apparatus, validation of experimental apparatus, discussion of test results, and summary of the main findings and conclusion of this work. Chapter one introduces the background and organization of the thesis.

Chapter two summarizes the recent literature review on frost study conducted by other researchers. The literature review intended to study the information about parameters that affect the frost formation on microchannel heat exchanger, and test facility and instrumentation used by other researchers. The objectives and scope of this project are discussed in detail throughout chapter three.

Chapter four introduces the experimental methodology developed to conduct frost experiment to study different parameters that affect the performance of microchannel heat exchanger during frost formation. The experimental methodology covered design of experimental apparatus, integration of different instrumentations, and usage of data acquisition system to monitor and record the entire experiment.

The fifth chapter describes the data reduction and uncertainty analysis of the experimental apparatus. The data reduction was focused on derivation used to evaluate the heat transfer performance over different sample geometries and test parameters. The uncertainty analysis was performed on all instrumentations used during the experiments. In addition, the test protocol and test procedures are also discussed in this chapter.

To ensure that all instrumentation was installed and working properly, an experimental validation procedure was develop and conducted. This procedure and results are explained in detail in chapter six.

Chapter seven summarizes the test results. Seven different microchannel fin samples with different geometries were tested in different parameters. The influence of different geometries and test parameters are discussed in detail. Chapter eight summarizes the main findings and conclusion of this work.

CHAPTER II

LITERATURE REVIEW

2.1 INTRODUCTION

There are several parameters that affect frost formation on outdoor coils, such as air velocity, air humidity, air temperature, cold fin surface temperature, surface energy, and fin-base contact resistance. While several researchers have investigated frost formation on flat horizontal plates and conventional fin-and-tube coils, few researchers have undertaken similar efforts for microchannel coils in transient frosting cases. The geometry of folded fin microchannel coils and the presence of a porous layer of air and ice in addition to the normal air-side and refrigerant side parameters makes the theoretical analysis difficult (Ohkubo 2006). Therefore, most of the frost studies on microchannel heat exchanger are conducted through actual experimental works.

In this chapter, the summary of extensive studies through different papers done by other researchers is provided. This literature reviews are concentrated on the investigation for important parameters affecting the frost growth, methods used by other researchers to conduct the experiments, and techniques to measure the frost. This chapter is divided into two sections, the first one consists of the parameters that significant to frost growth and the second one explains the method to grow frost and techniques of frost measurement.

2.2 PARAMETERS THAT IMPACT FROST GROWTH

There are some parameters that are more significant to frost growth compare to others. In this section, literatures related to the development of frost growth were being reviewed to further analyze the parameters driving the frost growth on the microchannel fins. The following is the summary of the literature reviews.

Kodepudi and O'Neal (1988) conducted frost experiment on louvered finned tube heat exchanger. They were trying to investigate the effect of frost growth on finned tube heat exchanger with function of fin density, humidity, and face velocity of the air. They tested three different coil densities (14, 18, and 20 fpi-fin per inch), three relative humidity conditions (65%, 74%, and 80%), as well as two different face velocities of the air (0.66 m/s and 1.02 m/s [130 fpm and 200 fpm]). The experimental set up they used for the experiment was placing a whole finned tube heat exchanger coil in a wind tunnel. The coil is cooled by using 50% ethylene glycol-water mixture and the condition of the refrigerant inside the heat exchanger is controlled so it remained constant at 1 - 2°F. The wind tunnel is used to condition the air that exposed to the heat exchanger. The temperature of air is kept constant at 0°C (32°F), while changing the relative humidity and velocity of the air. The mass of accumulated frost is measured by using difference measured on absolute humidity before and after the test coil and numerically integrate this value over time to obtain the accumulated frost weight. The result of the experiment discovered that the factors that increase the frost accumulation over time are the increase in the fin density, the absolute relative humidity, and the face velocity of the air.

Kim and Groll (2003) compared the performance of microchannel coil and fin-and-tube coil when used as outdoor coil in a commercially available 3-ton heat pump. The coils that were tested in the heat pump unit are spine-fin heat exchanger which considered as the baseline in the test. This heat exchanger is being compared to two other heat exchangers; microchannel heat exchanger with 15 fins per inch (FPI), and microchannel heat exchanger with 20 FPI. The selection of the coils is based on the manufacturer recommendation, trying to provide equal capacity when operate using the heat pump unit. During the experiment, the microchannel coils have two configurations which are vertically placed and at 15°-angular placed. The air condition for the experiment is based on standard ARI cooling and heating/defrosting tests. The result of the cooling tests showed that all four microchannel heat exchanger configurations improved the overall performance of the heat pump unit ranging from 1% to almost 6% when compared to the baseline coil. On the other hand, the results of the heating tests showed that all four microchannel heat exchanger configurations reduced the overall performance of the heat pump compared to the baseline coil. The experiments showed that for heating mode, the vertical configuration and lower FPI provide better overall performance since less defrost cycles is needed.

Peng et al. (2003) investigated the behavior of an air-source heat pump operating under frosting/defrosting conditions. Parameters investigated during the experiments were the frost layer thickness, compressor suction/discharge pressures, fin temperature, heating capacity, power consumption, and fan electric current. The heat pump unit was tested under condition specified by Chinese standard JB/T 4329-2001 (similar to ARI 590-1998) which yields to 89.43±1.7% and 9 & 3.50±1.1% relative humidity, and -0.5±0.4°C & -3.2±0.5°C dry bulb temperature. The result of the experiments shows that during frosting condition cycle, there is a critical value of the frost thickness which is 0.24 mm (0.01 inch). Once the frost thickness exceeds the critical value, the compressor performance will start to reduce due to reduction of the airflow rate and the increase in fan power consumption ultimately reduces the COP of the heat pump unit. During the defrosting mode, the compressor on the heat pump experienced frequent on/off cycle due to the rapid drop of the suction pressure of the compressor which exceeding the low-pressure limit. The researchers implemented few modifications to the heat pump unit to prevent the suction pressure to fall below the low-pressure limit. These modifications proven to improve the defrost cycle compare to the original design of the heat pump. The researchers believe that there are still room of improvement to be made for the defrost mode.

Shin et al. (2003) conducted an investigation on the effect of surface energy on frost formation. The authors investigated three aluminum flat plates with three dynamic contact angles: 23, 55, and 88 degree. The plates were coated with a special advanced plasma polymerization technology for improvement of surface wettability. The surface characteristics played an important role during the first stage, the nucleation of frost which became weaker as frost grew. The result of the experiment showed that at high dynamic contact angle, the frost grew irregularly and in rough crystal shape on the surface during the initial frost deposition, resulting in high frost thickness and low frost density. On the other hand, for low dynamic contact angle, the frost grew uniformly and in regular crystal shape, resulting in low frost thickness and high frost density.

Xia et al. (2006) investigated the effect of water retention in louvered-fin microchannel evaporators through experimental works. They tested five microchannel coils under frosting, defrosting, and subsequent refrosting conditions. From fiberscope images, they noticed that the corner formed by two adjacent fins hindered drainage of the droplets during the defrosting period. During the subsequent frosting cycle, the droplets froze directly into ice, and their volume expanded. In addition to providing a site for future frost growth, droplets retained during the defrost cycles increased the pressure drop. This observation is quite important because existing frost models assume initial conditions of dry (or uniform) frost layers on the surface while in the actual case, preferential sites of frost nucleation occured due to water droplet residuals from the previous defrost cycles. Xia et al. also observed that the refrosting behavior became periodic after about four frosts and defrost cycles. They tested five microchannel heat exchangers circuited in cross-flow configuration, airflow was horizontal and the microchannel tubes were vertical. The fin geometries were in the following range: fin density from 12 to 24 fins per inch, fin depth from 16 to 70 mm (0.63 to 2.76 inch), fin width from 8 to 10 mm (0.31 to 0.39 inch), louvered angle of 23, 27 and 30 degree and louvered pitch of 1 to 1.4 mm (0.039 to 0.055 inch). Although their work is one of the first examples on showing the direct impact of water retention on frosting and defrosting performance, the heat exchangers used in their study did not span across various fin density or louver design to allow for careful isolation of the effects. In addition, the fact that more than one parameter was changed at a time makes it more difficult to extend their work to correlate with fin designs different from the ones presented in their work. Xia and co-workers suggested additional experiments to parametrically extend the geometric dimensions in the data set to better understand the flow-depth, water retention, and fin geometry effects.

Padhmanabhan et al. (2008) evaluated the peformance of a 4 ton heat pump unit with a microchannel coil as outdoor evaporator in comparison with a heat pump that had identical capacity with a fin-and-tube coil as outdoor evaporator. Both coils had identical envelope dimensions. Their experimental work compared the dry and wet conditions where the heat pump would go through an initial frost and defrost cycle, and followed by the evaluation of cyclic periodic conditions after several frost/defrost cycles. The parameters evaluated in their work were frost cycle time, the frost weight, estimated coil surface temperature, and heat capacity and energy efficiency ratio (EER). Additional tests were conducted by blowing Nitrogen to the front air-side face of the wet coil at the end of the defrost period to remove water droplets retained in the coil. Their results showed only slight improvements of the frosting time through the usage of Nitrogen. The Nitrogen blow off extend the frosting period only by 4% with respect to ordinary wet coil condtions. The comparison between fin-and-tube and microchannel coil showed that fin-and-tube coil doubled the time between defrost cycles and 13% lower EER on heat pump system using microchannel coil compare to the one using fin-and-tube coil. In completely dry initial conditions the frosting cycle time of microchannel coil was about 60% longer than the one observed after several cycles, in which the coil was in wet conditions at the beginning of each frosting cycle. This result suggested that the root causes of capacity and performance degradations are not caused by the water droplets retained in the louvered folded fins at the end of the defrost period.

2.3 TEST FACILITY AND TECHNIQUES OF MEASUREMENT USED TO STUDY FROST ON MICROCHANNEL HEAT EXCHANGER

A lot of experiments on frost have been carried out by different reserachers. In this section of literature review, literatures describing ways the frost experiments conducted as well as the measurement techniques were analized to provide more insight on the best and most efficient way to conduct the frost experiments.

Mao et al. (1991) conducted frost experiment on flush-mounted removable disks. They tried to investigate the thickness, density, and mass concentration of frost with the function of time and distance from the leading edge. The experimental setup for this test is by placing the aluminum plate (where the flush-mounted removable disks are placed) inside a rectangular duct. In the duct, air was fully developed, turbulent, warm, and humid flowed parallel to the aluminum plate that been cooled down. The frost thickness in the experiment is measured using laser beam. The mass of the frost is measured by removing the disk from the aluminum plate, placing it in a sealed container and then weight the frost (by excluding the mass of the disk and container). The frost density and mass concentration is later derived from the measured mass and thickness of the frost.

Tao et al. (1994) conducted frost experiment on finned heat exchanger surface with fins mounted both vertically and horizontally, where the airflow is parallel to the fin surface. Various different materials (aluminum, brass, plastic, and Teflon) were tested in this experiment with varying the Reynolds number and relative humidity of the air. They were observing the frost growth and particle size with function of time. The experimental setup for this test is by placing the fin seat on top of thermo-electric cooling (TEC) to cool down the fin temperature to -25°C (-13°F). On the other side of the TEC, a heat exchanger with water as coolant is attached to remove heat from the TEC. A small channel is used to supply fully developed airflow with room temperature to the fin. This whole assembly sat on a microscope that coupled with camera. In the experiment, pictures are constantly taken to observe the frost growth qualitatively and using a correlation is used to estimate the particle radius.

Thomas et al. (1999) conducted frost experiment on a set of aluminum fins. They estimated the frost thickness on the aluminum fins with function of the location on the fin. The experimental setup for this test is by mounting the aluminum fins on top of the aluminum base plate. This aluminum plate is cooled down with 15 thermoelectric cooling (TEC) and the heat from TEC is removed with an ethylene glycol cooled heat sink. The temperature of aluminum base plate is maintained at -37˚C (-34.6°F). The whole assembly is placed in a controlled chamber that provides desired airflow that blown across the fins. The ambient air is supplied at -15˚C and -16.2˚C (5°F and 2.84°F) with humidity ratio of 9.7×10^{-4} and 8.3×10^{-4}. Tests were run for one to six hours to let the fin reach steady state and accumulate frost all over the fin. The frost measurement is conducted by removing the fin from the aluminum base plate. For frost thickness measurement, the fin is placed in a pre-cooled fin holder where a fully automated laser scanning system (LSS) is used to scan the whole fin and estimate the frost thickness base on the location (x and y location). For the mass of the frost, the fin is put into a sealed container and uses a digital balance with high accuracy to find the accumulated frost weight.

Moallem et al. (2010) focused on frost growth on various custom made microchannel heat exchangers with dimension of 0.3 by 0.3 m (1 by 1 foot). This coil were tested in a low temperature wind tunnel specifically design to replicate outdoor air during winter condition based on AHRI standard. The AHRI standard specify that the air condition need to be 1.7°C dry bulb temperature and relative humidity of 82%. The wind tunnel is equipped with custom frost measurement devices to measure frost thickness and frost mass on microchannel coil. The frost thickness measurement was obtained by processing images that taken by CCD camera placed right in front of the fins. The frost pictures were automatically taken for every one minute and then these pictures are processed carefully by using image process software. This frost measurement process is rather lengthy and requires experienced operator. The frost mass measurement was obtained from the weight increment of the coil, which was ancored to a digital scale during the forsting operation. Another measurements taken during the experiment are the pressure drop across the coil and the capacity of the coil measured through the air side and refrigerant side.

Wu et al. (2011) conducted a frost study on a folded-louvered-fin, parallel flow microchannel evaporator. The frost study was done through experimental test on heat pump central air-conditioning system utilizing microchannel as evaporator. The tests were conducted for three different indoor and outdoor conditions: 20°C/15°C, 19.95°C /16.25°C, and 19.98°C /15.79°C (DB/WB) for indoor air condition, and 14.71°C/12.98°C, 16.25°C/16.09°C, and 14.07°C/11.27°C (DB/WB) for outdoor air condition. The main components of this experiment were a test section, a data acquisition system, and a microscopic image acquisition system (CCD camera). The data acquisition system was used to measure the indoor and outdoor air condition working in conjuction with DAQ system controlling the heat pump to simulate the desired air conditions. DAQ system also used to record the measurements such as the temperatures, pressure drop, and most importantly the images taken by CCD camera during the experiment. The main measurements taken during these tests are the frost images on the fins of microchannel and the temperature distribution across the microchannel fins. The frost images taken by CCD camera was processed using digital image processing techniques to quantitatively analyzed the frost growth. While data on the data on temperature distribution across the microchannel fins is collected using, 16 calibrated termocouples attached to the fins at different locations on the leeward side.

2.4 CONCLUSIONS FROM LITERATURE REVIEW

From the literature review it appears that there is a need to provide consistent transient frosting performance data sets for louvered folded fins adopted in microchannel heat exchangers.

This thesis describes a new experimental methodology to measure the frost mass and frost thickness, and their rate of increase during actual operation of the louvered fins in cold ambient. Fin surface temperature, heat transfer and air-side pressure drop across louvered folded fins were also measured during transient frosting cycles. The feasibility and repeatability of the measurements is demonstrated through a series of controlled laboratory experiments that highlight the effects of fin surface temperature, air face velocity, and air humidity on the local frost growth on louvered folded fins. The effect of fin geometry on the thermal hydraulic performance is introduced with more results, analysis, and correlations of fin geometry and fin surface energy with the frost growth characteristics are also presented in this thesis.

CHAPTER III

OBJECTIVES AND SCOPE OF WORKS

This thesis presents experimental work to investigate several parameters that influence frosting performance in microchannel heat exchangers. An experimental apparatus was designed, built, and calibrated to measure the frost performance of microchannel heat exchanger in heat pump application during heating mode. Uncertainties and validation of the measurement were also analyzed.

3.1 OBJECTIVES

There are several objectives to be achieved in this project. The first objective is to design, construct, and calibrate a new experimental apparatus for investigating frost on microchannel heat exchanger. This includes the new design of microchannel fin samples and a new procedure to obtain the samples from commercially available coils. The second objective is to design instrumentation for measuring frost parameters such as; frost mass and frost thickness, heat transfer rate of the fin sample, and air-side pressure drop during the frost experiment. The last objective is to investigate, isolate, and possibly quantify the impact of fin temperature, fin geometry, air face velocity, and air humidity on the frosting performance.

3.2 SCOPE OF WORK

The project tests seven different microchannel heat exchanger geometries at different fin temperatures. The microchannel geometries tested are summarized in Table 1. The test geometries used in the experiment are fin density, fin depth, and fin height. The variation of fin geometries affects the characteristic of frost growth on the microchannel coil because changes of fin geometries directly correlate with the heat transfer performance. The impact of fin geometry on frost formation and heat transfer performance is observed directly by varying one variable and fixing the other two. The comparison among fin sample 1, 2, and 3 used to identify the effect of fin density. The effect of fin height is observed from fin sample 3, 4, and 5. The effect of fin depth is identified from fin sample 6 and 7.

Table 1: List of Fin samples geometries and test conditions

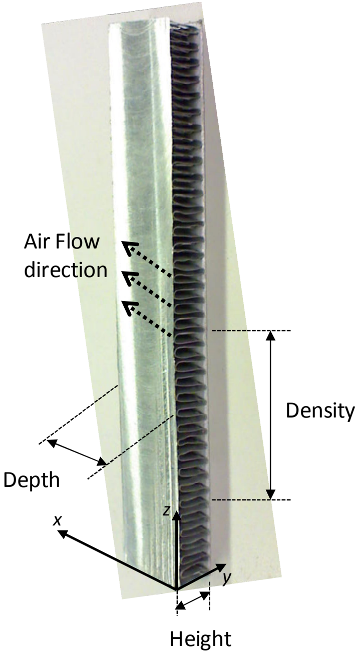

FIN SAMPLE	FIN DENSITY [fins per inch, FPI]	FIN DEPTH [mm] (inch)	FIN HEIGHT [mm] (inch)
1	10.4 (flat fin)	27 (1.063)	8 (0.315)
2	13.6	27 (1.063)	8 (0.315)
3	20.3	26 (1.063)	8 (0.315)
4	19.4	25 (0.984)	10 (0.394)
5	19.6	27 (1.063)	13 (0.512)
6	18.5	30 (1.181)	8 (0.315)
7	17.5	19 (0.748)	8 (0.315)

The operating conditions during the frosting measurement were carefully selected, such that the tested microchannel would operate in similar conditions as the outdoor coil in heating mode applications. The test conditions were also in agreement with the recommendations given in the

AHRI 210 standard for heat pump system performance rating (AHRI 2005). Table 2 provides the list of independent variables which were accurately controlled during the frosting experiments. The fin temperatures and air face velocity were selected from typical conditions of outdoor microchannel heat exchanger.

Table 2: Test condition for the frosting tests on microchannel heat exchanger

Independent parameters controlled during the frosting experiments	***Nominal value and tolerances during the frosting experiments***
Air side	
Entering air dry bulb temperature	1.67 ± 0.56°C (35 ± 1°F)
Entering air humidity ratio	0.0035 ± 0.0019 kg-water/kg-air (0.0041 and 0.003 kg-water/kg- air)
Initial entering air face velocity	1.5 m/s (295 fpm) ± 2.3% (0.8 m/s, 1.0 m/s, 1.2 m/s, and 1.6 m/s) [157 fpm, 197 fpm, and 315 fpm]
Fin sample side	
Fin surface temperature	-8 ± 0.23°C (-5°C and -11°C) [17.6 ± 0.41°F (23°F and 12.2°F)]

Frosting tests were conducted to investigate capacity degradation and rate of frost growth. Table 3 shows the test matrix for the experimental work. Every fin sample was tested with three different fin temperature conditions with air entering the fin sample at 1.7°C (35°F) dry bulb temperature and wet bulb temperature of 0.6°C (33°F), which yield entering relative humidity of about 82% and absolute humidity of 0.0035 kg-water/kg-air. The air face velocity on fin sample at the beginning of the test was set to 1.5 m/s (295 fpm) for fin sample 1, 2, 3, 6, and 7. The air face velocity was varied at 0.8, 1.2, and 1.6 m/s (157, 236, and 315 fpm) on fin sample 4. Fin sample 5 face velocity was set to 1 m/s (197 fpm). Additionally, the effect of humidity content in the air was investigated on sample 4 where the humidity ratio was varied from 72% to 92%.

Table 3: Summary of test matrix for the frosting test

FIN SAMPLE	FIN TEMPERATURE [°C](°F)	AIR RH (%)	AIR VELOCITY [m·s-1](fpm)	FIN DENSITY [fins per inch, FPI]	FIN DEPTH [mm] (inch)	FIN HEIGHT [mm] (inch)
1	-5 (23.0) -8 (17.6) -11 (12.2)	82	1.5 (295)	10.4 (flat fin)	27 (1.063)	8 (0.315)
2	-5 (23.0) -8 (17.6) -11 (12.2)	82	1.5 (295)	13.6	27 (1.063)	8 (0.315)
3	-5 (23.0) -7 (19.4) -8 (17.6) -12 (10.4) -13 (8.6)	82	1.5 (295)	20.3	26 (1.063)	8 (0.315)
4	-5 (23.0) -8 (17.6) -11 (12.2)	82	1.2 (236)	19.4	25 (0.984)	10 (0.394)
	-8 (17.6) -8 (17.6)	82	0.8 (236) 1.6 (315)			
	-8 (17.6) -8 (17.6)	72 92	1.2 (236)			
5	-5 (23.0) -8 (17.6) -11 (12.2)	82	1.0 (197)	19.6	27 (1.063)	13 (0.512)
6	-5 (23.0) -8 (17.6) -11 (12.2)	82	1.5 (295)	18.5	30 (1.181)	8 (0.315)
7	-5 (23.0) -8 (17.6) -11 (12.2)	82	1.5 (295)	17.5	19 (0.748)	8 (0.315)

CHAPTER IV

EXPERIMENTAL METHODOLOGY

4.1 INTRODUCTION

The literature review suggested that it is necessary to provide consistent transient frosting performance data sets for louvered folded fins adopted in microchannel heat exchangers. This thesis describes a new experimental methodology to measure the frost mass, frost thickness and their growth rate during the actual operation of the louvered fins in cold ambient. Fin surface temperature, heat transfer, and air-side pressure drop across louvered folded fins were also measured during transient frosting cycles. The feasibility and repeatability of the measurements are demonstrated through a series of controlled laboratory experiments. These experiments highlighted the effects of fin surface temperature, air face velocity, and air humidity on the local frost growth on louvered folded fins. The experimental methodology also introduced a new sample's design that was used throughout the experiments.

4.2 MICROCHANNEL FIN SAMPLE

The past experimental work by Moallem et al. (2010) suggests that the frost growth pattern on 1 ft × 1 ft (0.3 m × 0.3 m) microchannel coil under AHRI standard air condition is not uniform across the coil. The non-uniformity restricts the detail study of frost growth on microchannel. Therefore to grasp a better understanding of frost growth on microchannel fin a new experimental sample was developed. This new experimental sample is made from one column of louvered fins cut from commercially available microchannel coils. The tube of this one column of louvered fins was machine until a thin wall of metal attached to each side of the folded fins remained. The removal of microchannel tube is to eliminate the effect of different internal tube designs or microchannel ports. The vertical size of each fin sample was about 15.24 cm (6 inches), while the fin density, fin depth, and fin height determined by the original design of the microchannel coils from which the samples were cut. The following section covers the detail explanation on fin sample preparation and the design on the fin sample.

4.2.1 Fin Sample Preparation

The fin samples that tested in the experiment are fin samples cut out from commercially available microchannel coil. The process of making the fin samples required a detail and careful machining due to the fragility of the microchannel fins. In this section, detail description on preparing the fin sample is provided.

The first step to prepare the fin sample is to examine the manufacture coils that are going to be used as the sample. From the coils, all the fin columns are examined to determine which fin column is good to be used as the test sample. After finding which column will be used, both fin columns adjecent to it need to be cut as shown in Figure 1. Aside from cutting the fin columns, the fin sample also need to be cut to have vertical size of 15.24 cm (6 inches). This cutting process can be easily done using bandsaw. While cutting the columns of fin, ensure that the bandsaw blade is as close to the microchannel tube as possible as seen in Figure 1. This method will cut the unused fins at the same time clean the fin residue from the tube.

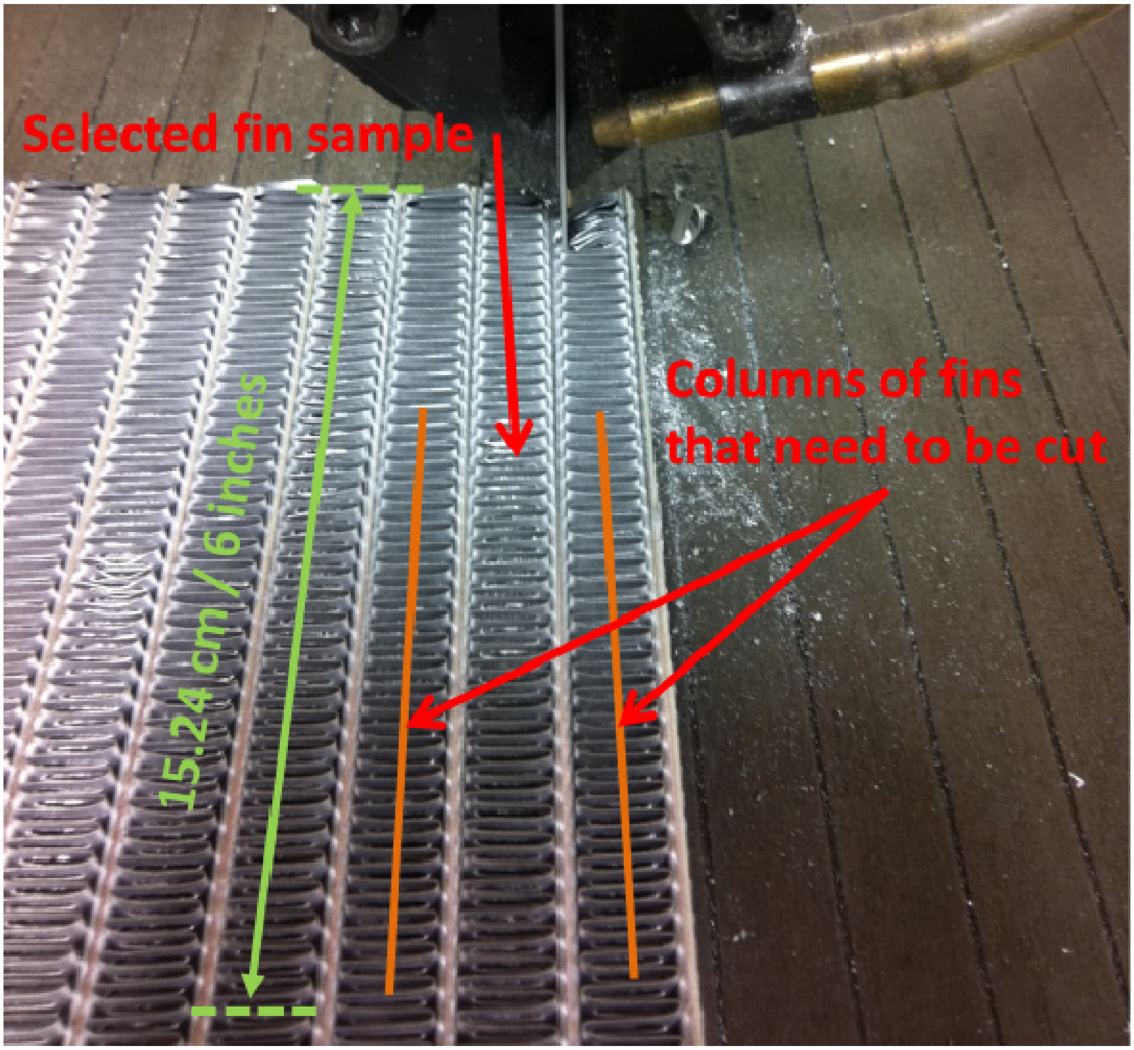

Figure 1: Step 1 of fin sample preparation

The second step was to machine down both of the tubes in between the fins until a thin wall or metal attached to each side of the folded fins. This machining process could be done by using milling machine. Before milling the sample tubes, tools needed to be prepared in advance are thin needles and sharp end mills bit with square end configuration. The needles were used to ensure that while machining the tubes, the sample stay flat on the vice of the milling machine. These needles were placed in between the fins under the microchannel tube and put on the vice of the milling machine as shown in Figure 2. While clamping the sample, make sure that the clamping force is good enough to keep the sample on the vice but at the same time not too much to damage the fin sample.

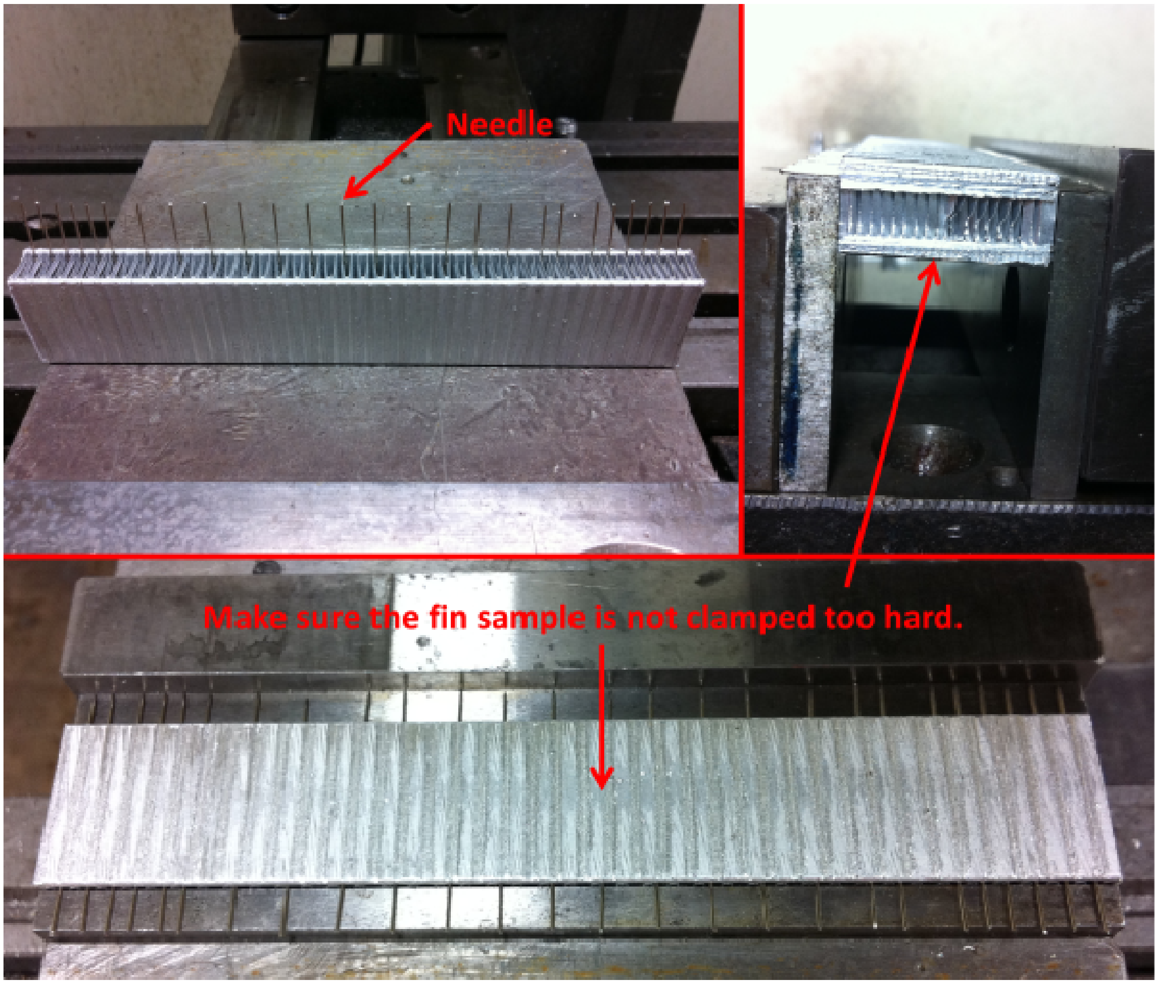

Figure 2: Step 2 of fin sample preparation

The sharp end mill bit were important because it will prevent damaging the fin sample during the cutting process and produced flat & mirror finish. When doing the milling on the fin sample, couple of the first cuts on the sample can be done with 0.254 mm (0.01 inches) depth but afterwards the depth of cutting should be reduce to 0.127 mm (0.005 inches) to prevent cutting too deep into the tubes. Towards the end of the process when the microchannel tubes getting really thin, the depth of the cut should be reduced to (0.0254–0.0508 mm) 0.001-0.002 inches until all the surface of the sample become flat and clean. The finished fin sample can be seen in

Figure 3. This milling process needs to be done frequently to get a good sample for the experiment.

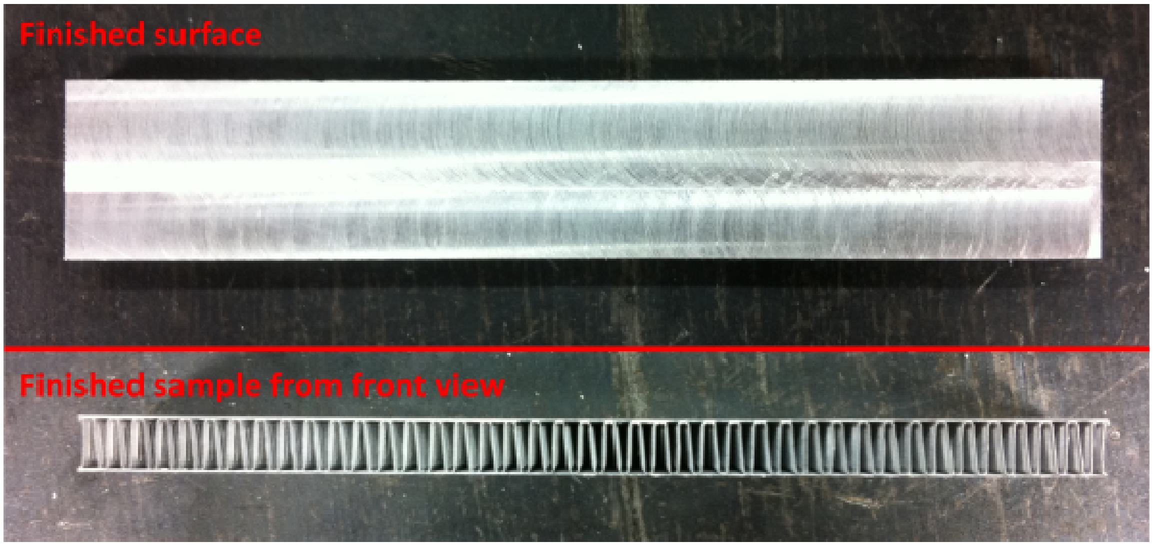

Figure 3: Finished fin sample

4.2.2 Fin Sample Design

The fin sample is designed to allow the measurement of fin temperature. As seen in Figure 5, the fin sample cut from the microchannel coil was placed in between two aluminum plates (¼ inches thickness). These aluminum plates provided proper housing for the thermocouples and the plates were attached to the fin sample by using thermal epoxy (Duralco 132-IP-1). The plates were cut to have the exact same sizes as the fin sample and four small grooves were cut out from the aluminum plates for placing the thermocouple wires. Four thermocouples are placed in between the aluminum plate and fin sample wall as shown in Figure 4. This fin surface temperature will be referred as the fin temperature (T_{fin}) throughout this thesis. It is obvious that the actual fin surface temperature along the edge of the fins varies depending upon the location in the fin and is a result of the local heat and mass transfer processes at the interface between frost and aluminum fins. Additional reinforcement was applied to strengthen the bond between the fin sample and aluminum plates. The reinforcement was by using epoxy (J-B Weld) at both top and bottom of the sample.

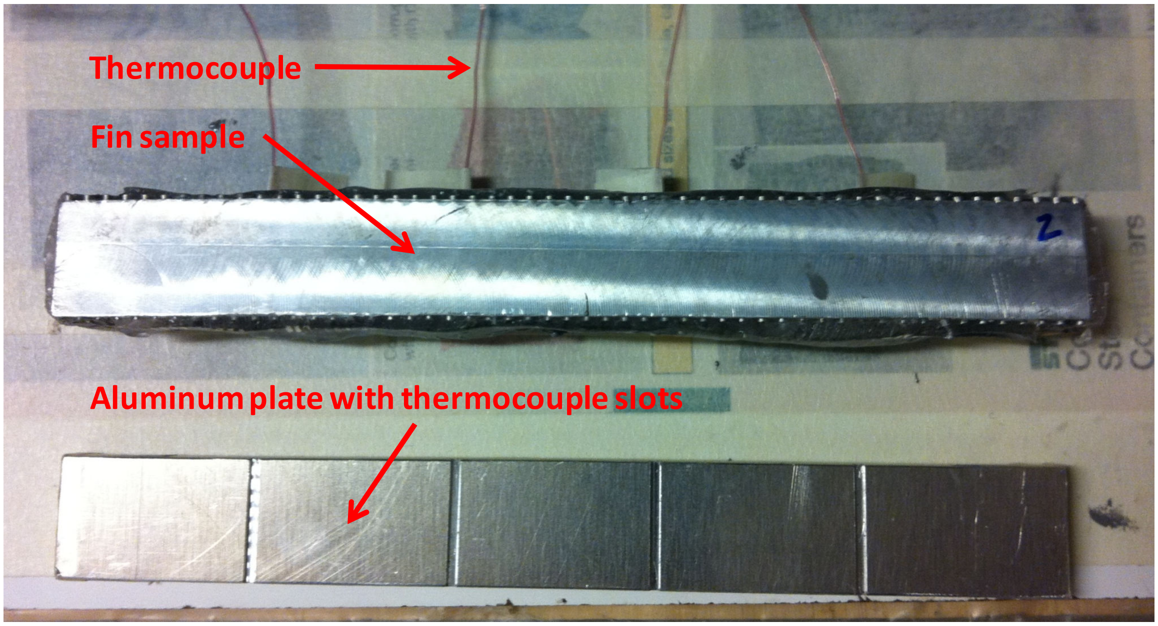

Figure 4: Fin sample with 4 thermocouples at each side

When frost started to accumulate on the fins, the air flow blockage could potentially become severe. To eliminate a systematic error during the measurements of the air-side pressure drop across the fin sample in frosting conditions, the air steam should not be allowed to by-pass the fin sample through micro cracks and small fissure around the perimeter of the sample. To eliminate the risk of air by-pass the fin sample, a plexi glass was installed at the inlet and outlet of the fin sample as shown in Figure 5. The prevention of air by-passing the fin sample when frost accumulates on the heat transfer surface was the key factor to achieve good repeatability of the measurements.

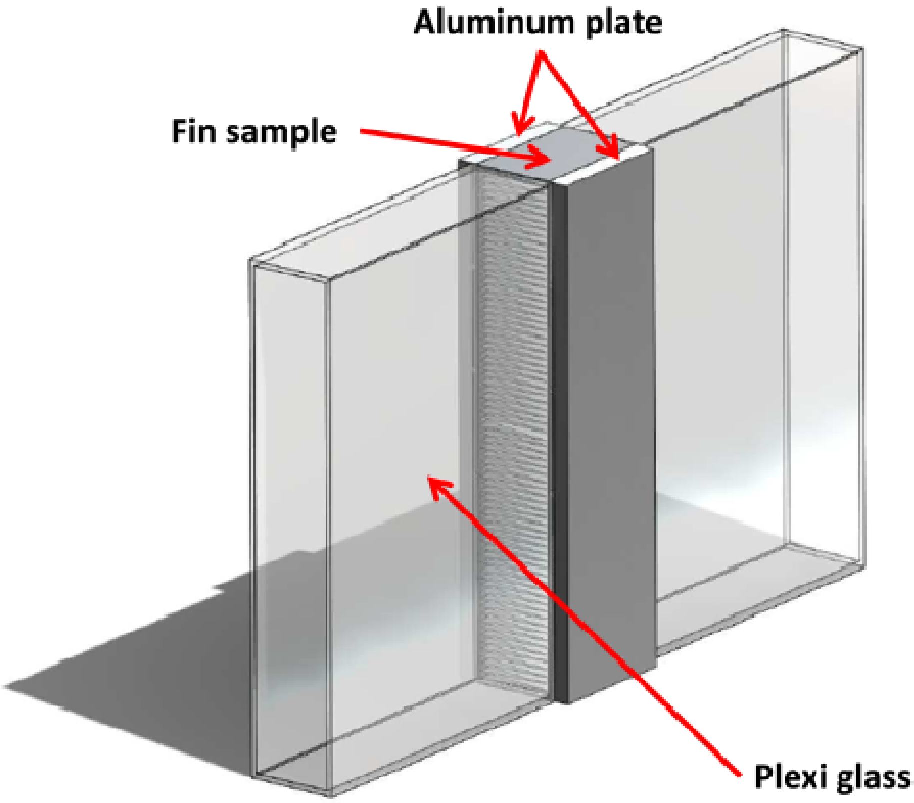

Figure 5: Fin sample with plexi glass

4.3 DESCRIPTION OF TEST SETUP

A test set up was designed and built in laboratory to investigate the thermal performance and frost deposition for microchannel heat exchanger. The basic layout of the test facility and the components are described in this chapter. The facility was designed to control the test condition specified in Table 3.

As seen in Table 3, the frosting test was conducted by controlling the ambient air condition and the fin sample condition. The ambient air is controlled in the airflow loop as seen in Figure 6. The airflow loop is a closed loop wind tunnel with equipment and censors to control and monitor the air condition inside the tunnel. The fin sample is conditioned with the cooling loop as seen in Figure 7. The cooling loop is a custom setup function to cool and maintain the fin sample condition throughout the experiment.

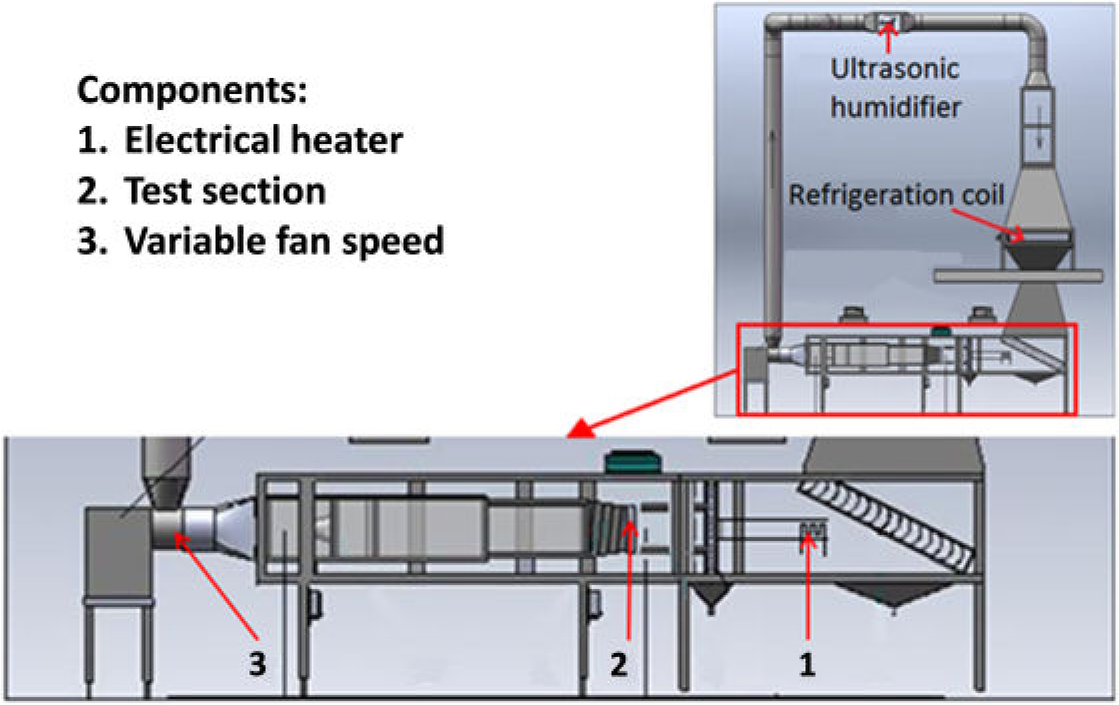

Figure 6: Airflow loop (Redrawn after Moallem et al (2010a))

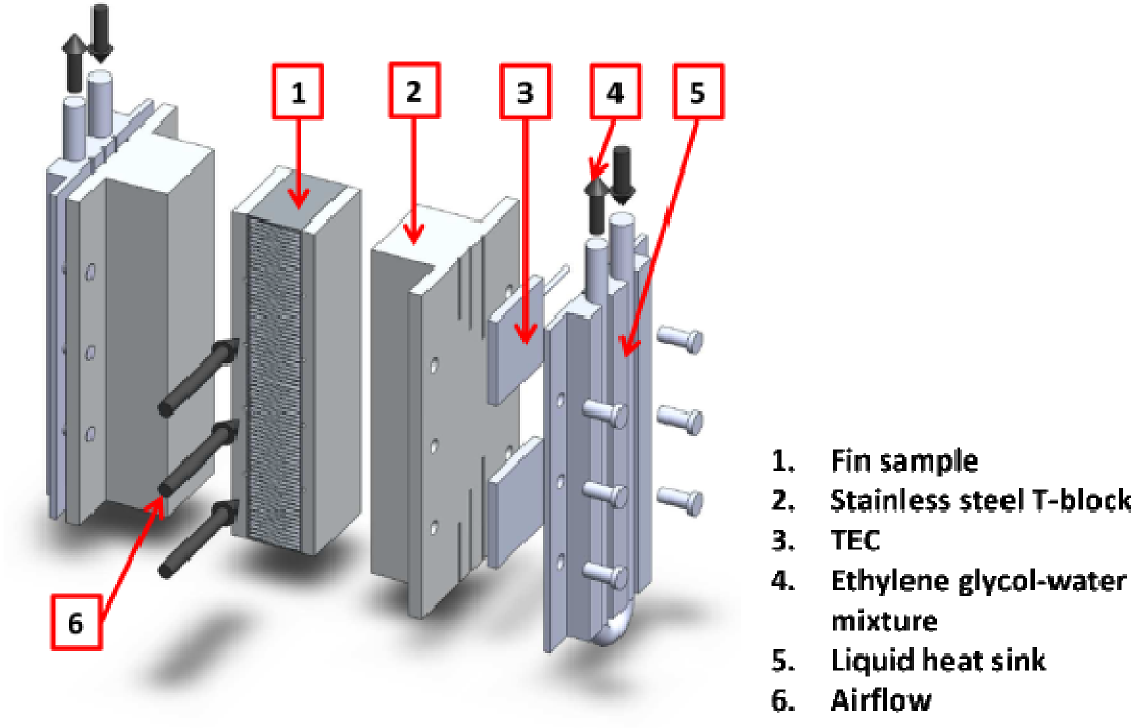

Figure 7: Cooling loop

4.4 EXPERIMENTAL APPARATUS

The experimental apparatus mainly consisted of two main sections (airflow loop and cooling loop) with two auxiliary loops (chiller loop and heat sink loop). The overall airflow loop and the cooling loop can be seen in Figure 6 and Figure 7. The cooling loop is located in the test section (2) in airflow loop. The airflow loop is utilized to condition the air inside the tunnel to simulate ambient air at winter condition. Main components such as refrigeration coil, variable speed fan, electrical heater and ultrasonic humidifiers are used to cool and condition the air to the desired condition. Additionally, the cooling loop is used to cool the fin sample simulating the condition of outdoor coil during heating mode. The cooling loop is mainly consisting of Thermal Electric Cooling or known as TEC with custom design stainless steel T-block and liquid heat sink. The chiller loop is utilized to provide cooling for airflow loop, while the heat sink loop is utilized to provide cooling for cooling loop. In the following sections, two main loops and two auxiliary loops will be presented.

4.4.1 Airflow loop

The airflow loop is a custom wind tunnel built for controlling air to desired condition. This wind tunnel has a square cross sectional area of 2 feet × 2 feet and span about 109 inches long. The tunnel is a close loop duct system equipped with ultrasonic humidifiers, refrigeration coil, electrical heater, and a centrifugal variable speed fan. The overall schematic of the airflow loop is shown in Figure 6. The airflow loop is utilized to control the inlet air condition within a narrow range as specified in the standard AHRI 210 for heat pump system performance rating (AHRI 2005). The inlet air must be controlled at 1.67/0.56°C (35/33°F) dry bulb/wet bulb temperature, unless otherwise specified. This air condition yields the air relative humidity of 82% during the experiment. The air face velocity at the inlet is controlled with a variable speed fan with a range of 0.8 to 1.5 m/s (157 to 295 fpm). The detail of ambient air condition can be seen in Table 3.

4.4.1.1 Control of airflow loop

The control schematic that I adapted to control the air inside the wind tunnel is shown in Figure 8. The set point condition of the air at the inlet of the fin sample is represented by point 4. The air was cooled when it passed through the fin sample, thus the temperature decreased and the humidity content in the air was reduced shown as point 5. The location of point 5 in Figure 8 can be varied depend on the capacity of the tested fin sample. The cold air that leaves the fin sample is being recirculated again inside the wind tunnel. This air is being heated up from point 5 to point 1 due to the heat gain caused by temperature difference between the air inside the tunnel and the air around the tunnel at approximate 23.89°C (75°F). Additionally, the pressure difference between inside the tunnel and surrounding also caused infiltration. Point 1 is the estimated air condition before the humidifiers. From point 1 to point 2, there is humidification process to increase the humidity content of the air before the refrigeration coil. The rate of humidification process can be adjusted by controlling the number of humidifiers that operates in the DAQ system at any given time during the experiment. Between point 2 and point 3, the heat in the air was removed by the refrigeration coil. This coil is directly connected to a low temperature chiller. The amount of the cooling can be adjusted by changing the high precision valve that regulates the amount of refrigerant flowing to the cooling coil. The air is then heated by a variable output electrical heater to control the air to the set point of 1.67/0.56°C (35/33°F) dry bulb/wet bulb temperature. °

During the experiment, the control schematic must be adjusted to compensate for sudden change in the air condition. The adjustment can be done by modifying any of these three methods:

1. Adjusting the number of operating humidifiers (0 to 4) through the DAQ system. This adjustment is used to regulate the moisture in the air.
2. Adjusting the amount of refrigerant flowing to the refrigeration coil. This adjustment is used to regulate the amount of heat removal from the air, which translates to alteration in both air dry bulb temperature and the moisture content in the air.
3. Adjusting the power to the electrical heater. This adjustment is used to regulate the amount of heat addition into the air to modify both dry bulb temperature and moisture content in the air.

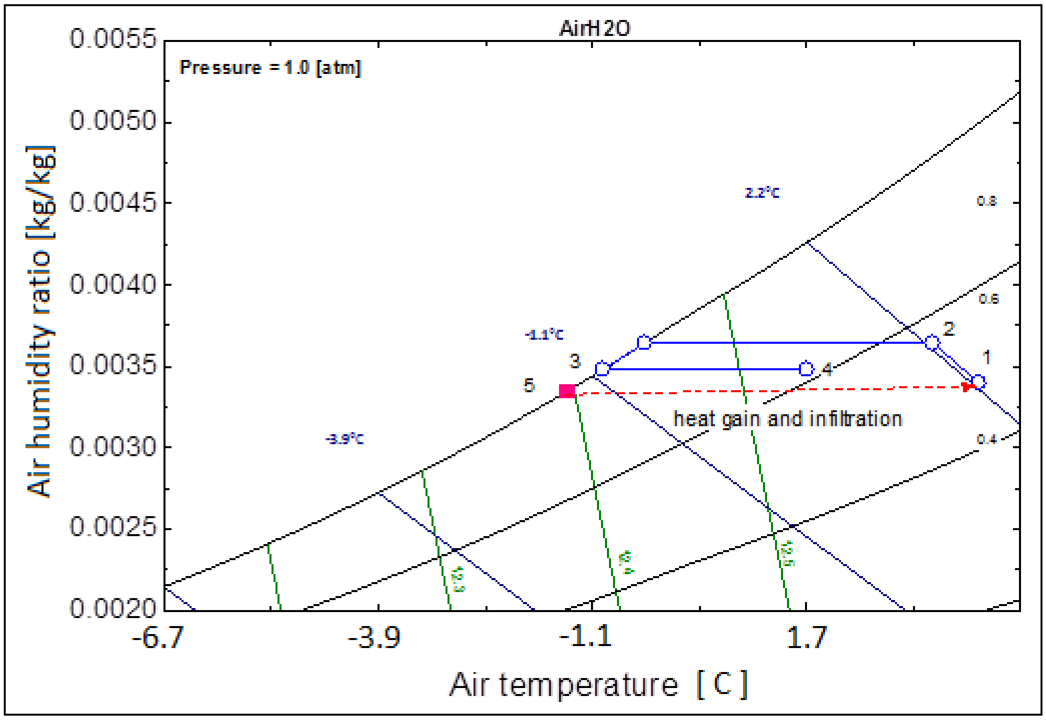

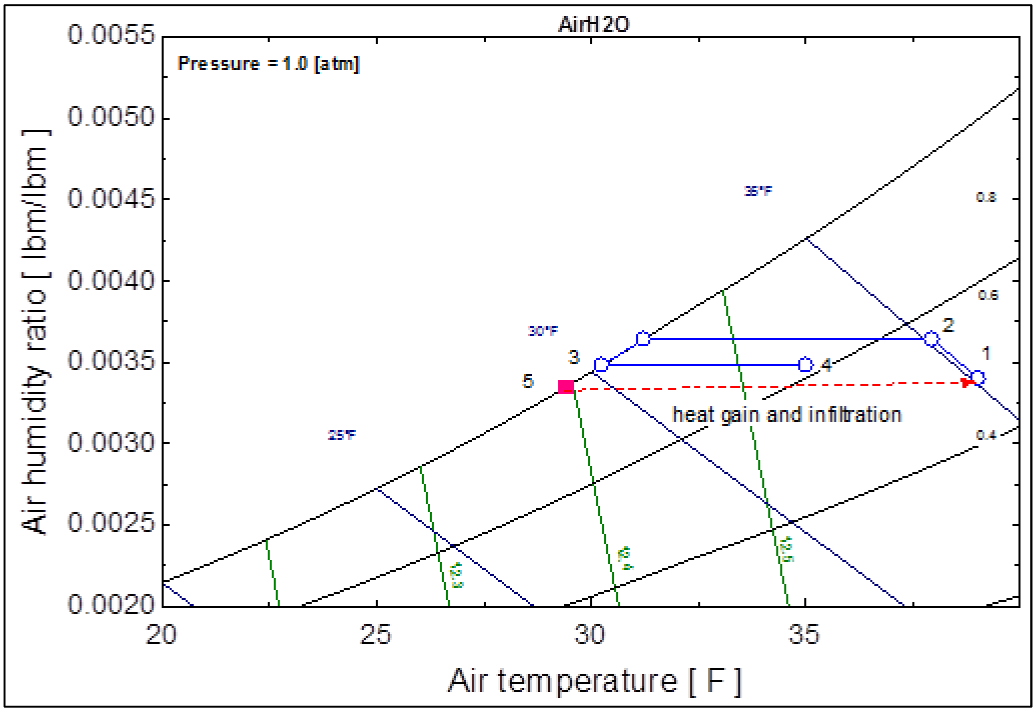

Figure 8: Schematic of controlling ambient air in the airflow loop (Redrawn after Cai S. (2009))

4.4.2 COOLING LOOP

The cooling loop is test apparatus used to cool and maintain the condition of the fin sample. During the test, the fin temperature was controlled below freezing temperature to form frost. To cool down the fin sample, a method originally proposed by Thomas et al. (1999) was adopted. Thermal-Electric Cooling or TEC was installed to remove heat from the fin sample and to control the fin temperature during frosting. Four 44 watts (150.13 Btu/hr)-capacity TECs were used to cool the fin sample, two attached at each side of the fin sample as shown in Figure 7. The amount of heat transfer from the fin sample to the liquid heat sink was accurately controlled by variable power transformers connected to each TEC independently. Ethylene Glycol was circulated inside the liquid heat sink removing heat from the test apparatus. Two custom made stainless steel T-shape blocks were inserted between the fin sample assembly and the TECs. The T-blocks were machined to nearly the same depth as the fin sample assembly to provide uniform heat flux perpendicular to the fin assembly walls. Each TEC was instrumented with six thermocouples, three on the hot side and three on the cold side, to monitor the cooling load of the device. The air flows into the fin sample along the x-direction as shown in Figure 9. Heat is removed from the air stream by the louvered fins and it is laterally transported along the y-direction by the T-blocks. The entire device was assembled in a compact test assembly, as shown in step (3) of Figure 9. Then the test assembly was mounted inside the low temperature wind tunnel as shown in step (4), and exposed to frosting ambient conditions during the tests.

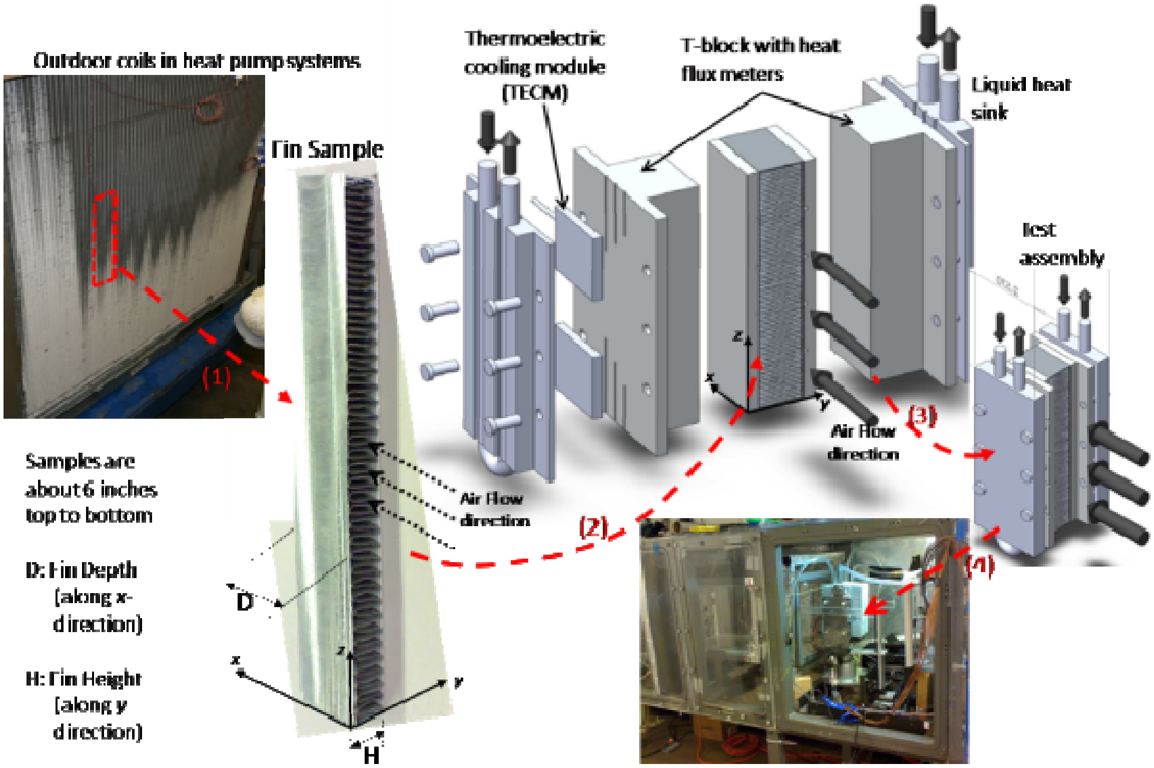

Figure 9: Procedure for the preparation of the test assembly set up inside the wind tunnel

Even though the temperature gradient was quite small, foam insulation boards were installed around the T-blocks to minimize the heat gain to the fin sample during the frosting experiments. The un-insulated and insulated test apparatus are shown in Figure 10 (a) and (b), respectively. The apparatus was mounted on an adjustable mechanical vice that was modified ad-hoc for these experiments with adjustable springs as shown in Figure 10 (a). The springs redistribute the contact pressure along both surfaces of the fin sample assembly and the vice provides sufficient pressure on the fin sample to allow heat conduction across the surfaces in mechanical contact during the frosting periods. The vice was opened to detach the fin sample at the end of the frosting period in order to quickly measure the weight of the frost accumulated on the fins.

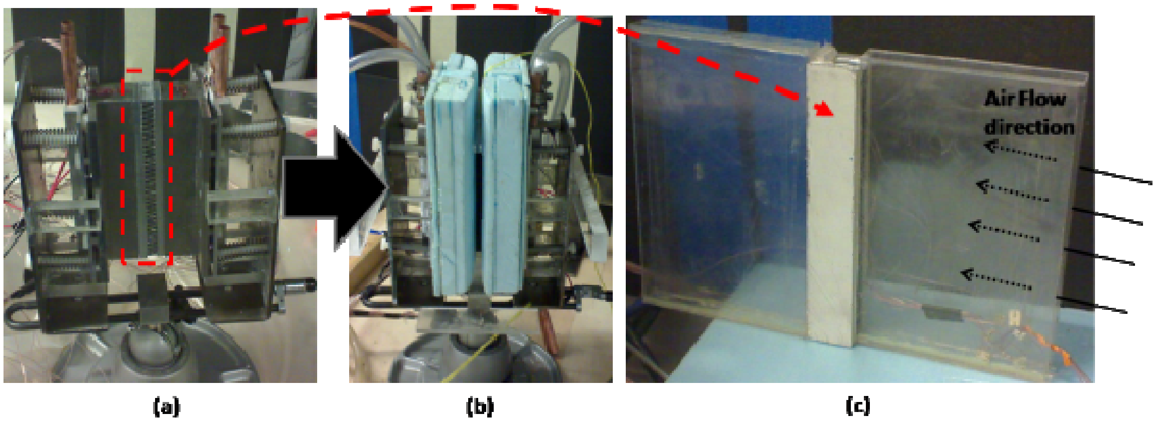

Figure 10: Photo of the test assembly mounted on the modified vice with springs (a) un-insulated test apparatus; (b) insulated test apparatus; and (c) zoom of the fin sample attached to transparent plastic channels at the inlet and at the outlet of the fin sample with respect to the air flow direction

4.4.3 CHILLER LOOP

The chiller loop is utilized to provide cooling to the airflow loop. The overall schematic of chiller loop can be seen in Figure 11 with blue solid line. As seen in the figure, the chiller loop is directly connected to the low temperature chiller. The model number of this chiller is CPCW-12LT/TC2-1-9X2 from Cooling Technology. This low temperature chiller supplies up to 2.0 tons capacity with leaving temperature of -31.67°C (-25°F). The process fluid in the hydronic loop of this chiller is Dynalene HC 40, while R404A refrigerant is used in the compressor side of the chiller. The chiller is equipped with recirculating pump that supply up to 6 to 8 gpm with pressure rise between 25 to 30 psi (172.4 to 206.8 kPa). This chiller is equipped with integrated temperature controller which can be used to set the leaving fluid temperature.

This chiller is directly connected to refrigeration coil used to provide cooling to the air in the airflow loop. Additionally, one plate frame heat exchanger is installed in the chiller loop. This plate frame heat exchanger is used to exchange heat between the refrigerant in the chiller loop and the heat sink loop.

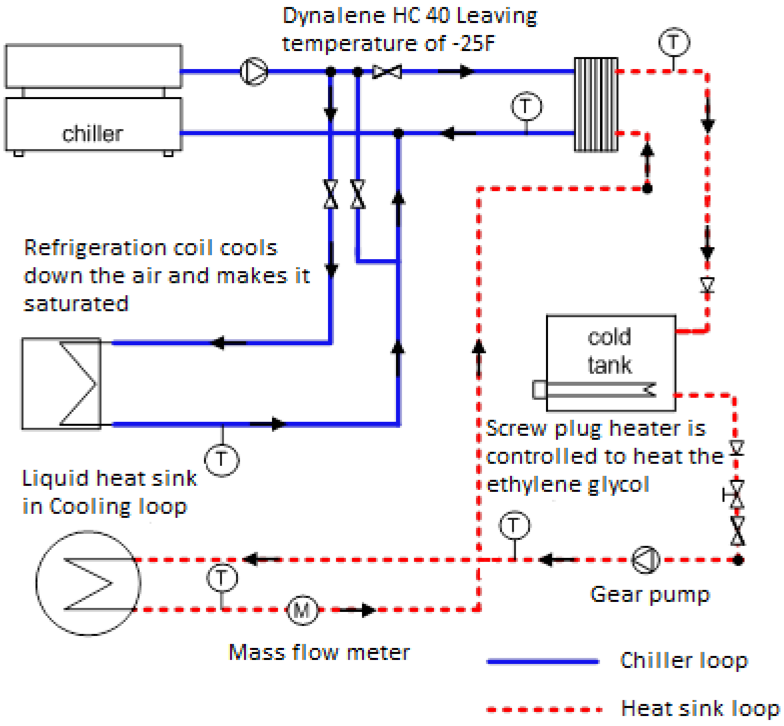

Figure 11: Chiller loop and heat sink loop (Redrawn after Cai S. (2009))

4.4.4 HEAT SINK LOOP

The heat sink loop is designed to provide cooling to the heat sink in the cooling loop. The heat sink loop consists of one plate frame heat exchanger, a gear pump, and a cold reservoir as seen in Figure 11 with red dash line. As mentioned in the previous section, the refrigerant in the heat sink loop is cooled by the chiller loop utilizing the plate frame heat exhanger. The main refrigerant in this loop is ethylene glycol 50/50 mixture.

The parameters that can be controlled in this loop is the fluid temperature and flow rate to the heat sink in the cooling loop. There are multiple methods that can be used to control the fluid temperature; adjusting the set point temperature in the chiller, adjusting the ammount of refrigerant flow from the chiller loop to the plate frame heat exchanger, and utilizing PID controller that made in the DAQ system to control the screw plug heater in the cold tank reservoir. The flow rate of the refrigerant inside the loop can be controlled by utilizing PID controller in the DAQ system. The PID controller is used to adjust the input frequency to the Variable Frequency Drive (VFD) that regulate the RPM on the pump and alter the flow rate.

4.5 INSTRUMENTATION AND DATA ACQUISITION SYSTEM

This section contains a brief description of the instumentation, the data acquisition system, and the various measurement and control devices installed throughout the test apparatus.

4.5.1 Thermocouple

Thermocouple is used in the experiment to measure the dry bulb temperature of air at the inlet and outlet of the fin sample, surface temperature of the fin sample, and surface temperature of TEC (cold side). T-type thermocouples from Omega are used for all of the temperature measurement. Considering the possibility of a non-uniform measurement, the measurement of each parameters was done by using multiple thermocouples/thermocouple grids. The number of thermocouples used, nomial range, and acuracy of each measurement are shown in Table 4.

Table 4: Thermocouple readings

Measured parameter	Number of thermocouples	Nominal range	Accuracy
Fin temperature	8	-4 to -12°C (24.8 to 10.4°F)	± 0.43°C (0.77°F)
Inlet dry bulb temperature	3	2.22 to 1.11°C (36 to 34°F)	± 0.67°C (1.21°F)
Outlet dry bulb temperature	8	3 to -11°C (37.4 to 12.2°F)	± 0.28°C (0.50°F)
TEC surface temperature (Cold side)	12	-8 to -14°C (17.6 to 6.8°F)	± 0.63°C (1.13°F)

Each of the thermocouples was calibrated within their operating range using NesLab Instruments Inc. constant temperature bath chiller model RTE-140. One of the termocouples calibrations for fin temperature measurement can be seen in Figure 12.

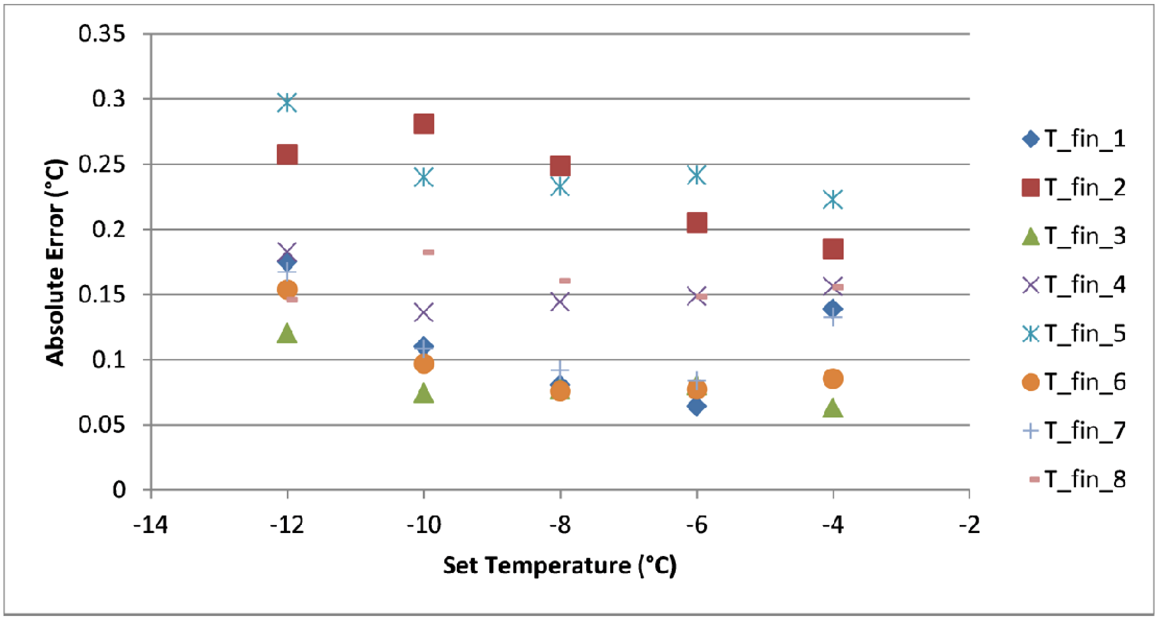

Figure 12: Fin temperature calibration

4.5.2 Dew point meter

The dew point temperatures of the air at the inlet and outlet of the sample were measured by using chilled mirror dew point meters. The dew point meters were selected from TTI Instruments, Inc. with model number of GE OP-D-1-0-A-A-1-0-0 of General Eastern Optica Series. The operating range of this device is between 0 to 50°C (32 to 122°F) with accuracy of ±0.2°C (0.36°F). The output of the device is 4 to 20 mA and 0 to 5 VDC signal to the DAQ system. The chilled mirror dew point meter requires additional sampling of the air to measure the dew point temperature. The sampling of the air is done by using Sample System Module (SSM) with model number of P40230968. This SSM consists of a vacuum pump, flow meter, and flow control valve which is enclosed in moisture resistance housing. The sampling airflow rate is about 0.5 ft^3/hr.

4.5.3 Air face velocity

The air face velocity in the experiment was estimated by measuring the air volumetric flow rate across the fin sample as shown in Equation (1).

$$V = \frac{Q}{A} \tag{1}$$

Where :

- V = Air face velocity (m/s or ft/min)
- Q = Air volumetric flow rate (m^3/s or ft^3/min)
- A = Fin frontal area (m^2 or ft^2)

Air volumetric flow rate was estimated from the static pressure difference across the nozzle that installed in a custom build tunnel as seen in Figure 13. This tunnel was designed and built according to ASHRAE standard 41.2.

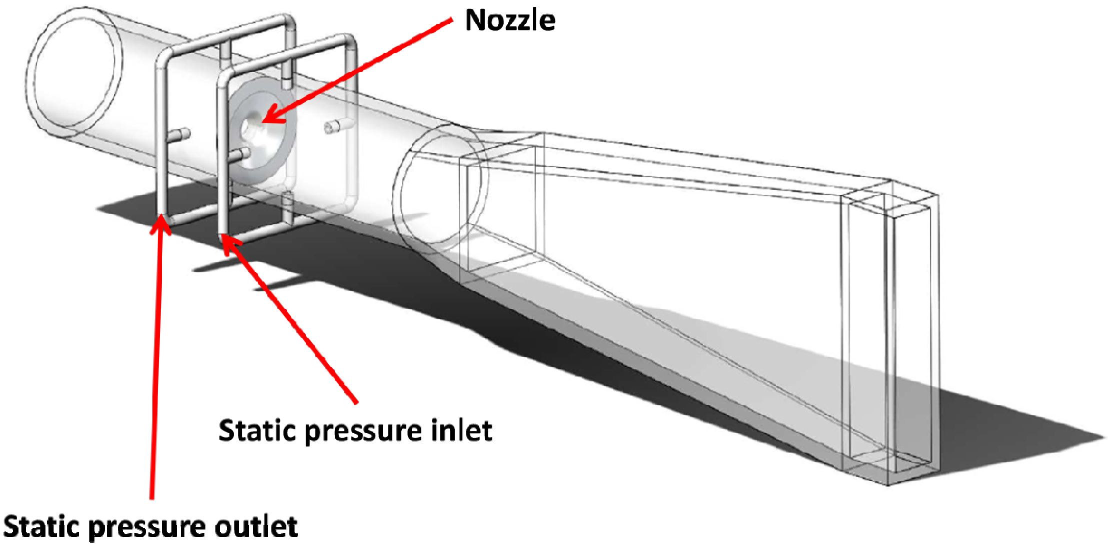

Figure 13: Flow nozzle

The pressure difference between before and after the nozzle was measured by differential pressure transducer Setra model 264 as seen in Figure 14. The operating range of the pressure transducer is between 0 to 450 Pascal (0 to 1.81 inch H_2O) with accuracy of ±40 Pa (0.16 inch H_2O).

Figure 14: Differential pressure transducer

In-house checking of the pressure transducer was conducted by comparing the pressure readings with the ones of a high precision manometer that had accuracy of ±4.98 Pa (0.02 inch H_2O). The results are shown in Figure 15 and the pressure transducer seemed to be shifted by a constant value of 40 Pa (0.16 inch H_2O) with respect to the manometer. This was a source of systematic error that was present in the air flow measurements. At the beginning of the test this systematic error had negligible impact on the absolute value of the air flow measurement. The error became significant toward the end of the frosting tests for which the measured pressure difference across the nozzle was about 30 Pa (0.12 inch H_2O). It should be noticed that since the error was constant throughout the entire flow rate range, the relative drop of pressure differential which corresponded to the drop in the air flow rate across nozzle, did not have such error. Thus, the relative comparison of initial and final velocity did not have this source of systematic error in it.

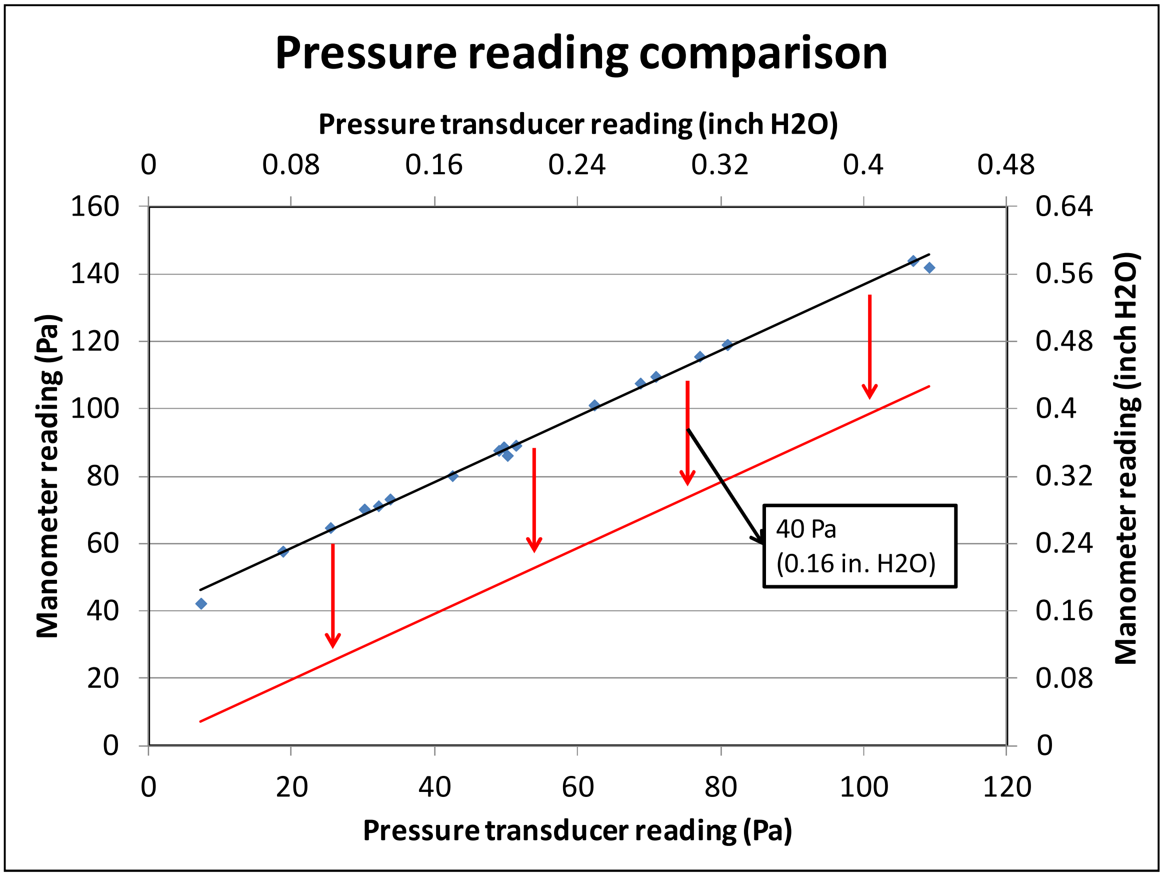

Figure 15: Pressure reading comparison between pressure transducer and manometer

4.5.4 Differential pressure transducer

A differential pressure transducer from Setra was used to measure the static pressure drop across the fin sample during the frosting experiment. The static pressure was measured at both inlet and outlet of the sample using static pressure tap as shown in Figure 16. The model of the differential pressure transducer is 264 as seen in Figure 14. The operating range of the pressure transducer is between 0 to 623 Pascal (0 to 2.50 inch H_2O) with accuracy of ±6.23 Pa (0.03 inch H_2O).

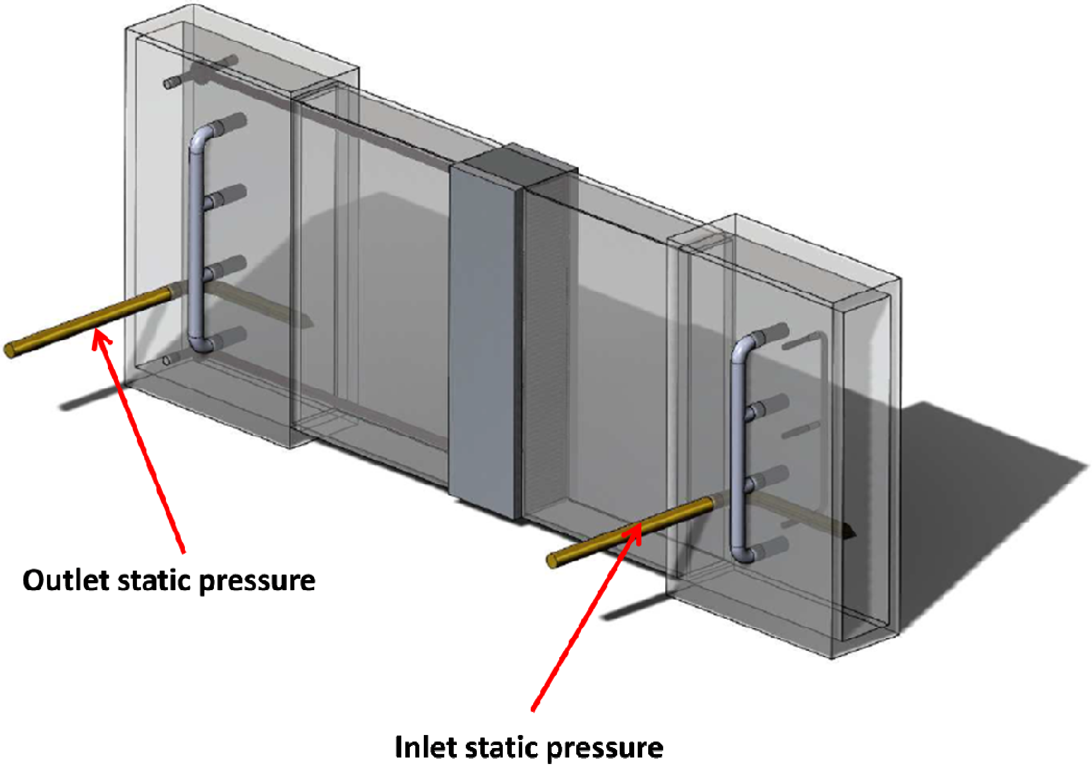

Figure 16: Pressure drop across the fin sample

4.5.5 Frost thickness

The frost thickness provides information about the frost grew pattern and the type of frost that grew on the fin sample. It also identifies the location at which the airflow blockage occurred that ultimately stop the heat transfer process. Frost thickness was measured with a magnifying high resolution short focus CCD (Charge-Coupled Device) camera that has a borescope probe extending about 1 meter (3 feet) inside the wind tunnel. The probe tip of the borescope was installed at the front of the fin sample. The value of frost thickness was obtained by scaling high resolution images using special imaging computer software (iView PC). The distance between two adjacent fins was used as reference dimension and the fin edge in initial (dry) conditions was selected as starting point, that is, as reference for the frost thickness, as shown in the example of Figure 17 for the “start test” image. Figure 17 shows the images from the CCD camera at various instances during the frosting period, but it should be emphasized that this figure is only for illustrative purpose. The actual measurements were made on a much larger scale by using magnified high resolution photos of the frost on the fin sample. Figure 17 depicts well the concept of the methodology adopted for the frost thickness measurements. The cold base plates attached on the sides of the fins were maintained at constant fin temperature throughout the test period, and heat was continuously extracted from the fins along the transverse direction by the two TECs mounted on each side of the fin sample assembly. The power supplied to the TECs was controlled in order to keep T_{fin} constant during the entire frosting period. The second photo in Figure 17 shows the onset of frosting at about 2 minutes. After 5 minutes the frost profile became more defined, and then it continued to advance until 21 minutes, approximately the end of the test since the fin sample was completely covered with frost. Frost grew mainly perpendicular to the fin surfaces and the CCD camera captured digital photos every 1 minute. From these observations, it was emphasized that the growth of frost was in two directions: the main direction was perpendicular to the fin surfaces and the second direction was perpendicular to the fin leading edge toward the CCD camera. The frost growth in the direction perpendicular to the fin surface was prevalent during the initial frosting period. Some frost grew from the side tube wall along the horizontal direction, but it was mainly the frost growth in the main direction that was responsible for the air flow blockage of the coil. The main advantages of this technique were that it was not invasive and it did not interfere with the frost growth process. The data reduction of frost thickness from the digital photos requires considerable time and experience of the operator. Further details on the measurements of the frost thickness using this imaging technique are provided in the papers by Moallem et al. (2010a, b).

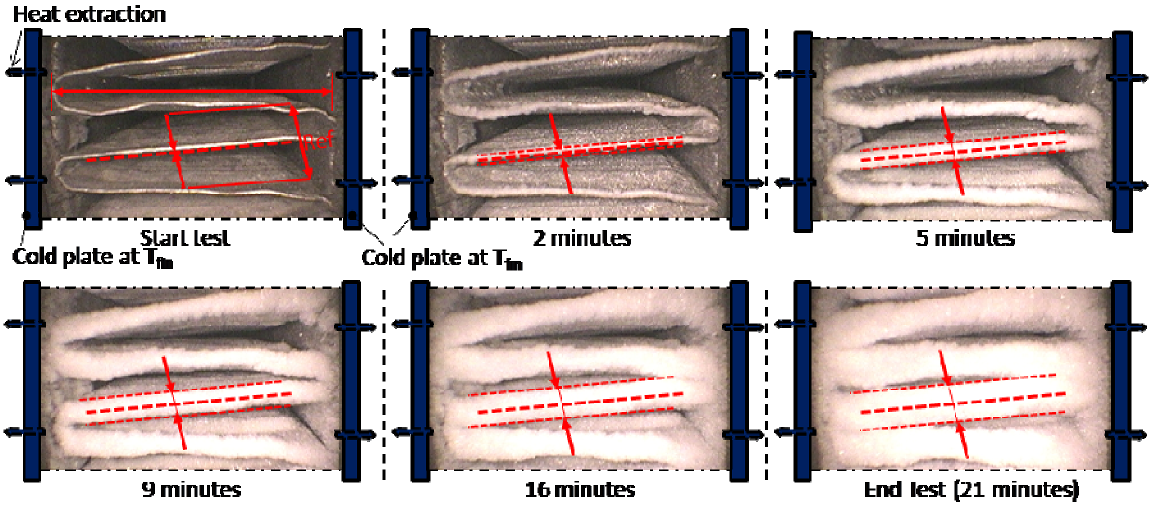

Figure 17: Frost thickness measurement

4.5.6 Frost weight

The accumulated frost on the fin sample during the frosting experiment was weighted at the end of the test to measure the weight of frost accumulated during the experiment. At the end of the test, the fin samples were quickly removed from the vice and the weight was measured using a high precision digital scale (iBalance 401). For each sample, the weight with frost was compared to the initial weight of the sample (in dry conditions) so that the weight due to frost accumulated on the fins could be accurately determined. During the weighing process, no water droplet was found on the sample which indicates that there was no frost melted. The accumulated frost on the fin sample can be used to identify the amount of water that stay on the fin sample. The accuracy of frost weight measurement is ±0.2 gram.

4.5.7 Data acquisition system

All of the measurements were taken using a Fluke® 2680 data logging acquisition system. The data looging acquisition system can hold from 1 to 6 analog modules. These modules are used to measure DC volts, AC volts, ohms, temperature, frequency, and DC current. In the experiment, the module is mainly used to measure DC volts and temperatures.

Couple of instrumentations such as differential pressure transducer requires power excitation. To provide low power voltage control signals, control boards PCI-DAC 6703 and PCI-DAS 6025 from Measurement Computing® were used.

LabView® ver.8.5 is the software used to communicate with the DAQ hardware. It is graphical programming software used to read, store, and visualize the measurement. LabView was selected for the data acquisition system because of its stability, high sampling rate, ease to use, and graphical interface.

A program was written in the LabView to record quantities, calculate the derived quantities, control the test facility, and plot the data. The recorded quantities in the experiments are the dry bulb temperatures (inlet and outlet of the fin sample), fin temperature, and TEC surface temperature (cold side). The derived quantities are humidity ratio of the air (inlet and outlet of the fin sample), pressure drop across the nozzle, and pressure drop across the fin sample. The air humidity ratio was calculated by applying equations obtained from ASHRAE fundamental with dew point temperature and dry bulb temperature as input variables. The pressure drop/pressure difference was calculated by applying the equation obtained from calibration process. The control on the test facility is only utilized to control the flow rate and temperature of ethyln glycol in the heat sink loop.

The main benefit of using LabView program for the frost experiment is its ability to plot the data simultaniously. The graphical representation of the data during the experiment assisted the people who conduct the frost experiment making necassary adjustment to control the quantities within the specified condition (e.i. inlet air condition, and fin sample).

CHAPTER V

DATA REDUCTION AND UNCERTAINTY ANALYSIS

5.1 INTRODUCTION

In this section, the data reduction and uncertainty analysis at the heat transfer performance are discussed in more details. The heat transfer performance was evaluated over various fin geometries, and parameters such as fin temperature, air condition, and air face velocity. The heat transfer rate of the microchannel fin sample was computed using two different methods. The first method is calculated from the air side or enthalpy method, and the second method is calculated from the conduction side or conduction method. These two methods of estimating the heat transfer rate will be discussed in more detail later in this section.

5.2 TEST PROCEDURE

All experimental tests were conducted with the fin sample initially in dry condition. The fin sample assembly was left at room temperature overnight to achieve dry surface condition. Then, the assembly was installed into test apparatus and the air stream in the wind tunnel was set to 1.7/0.6°C (35/33°F) dry bulb/wet bulb temperature in about 4 to 5 hours with the air velocity at 1.5 m/s (295 ft/min). Once the wind tunnel reached steady state conditions, the experiment can be conducted. The first step for the test procedure was to cool down the fin sample to the desire fin temperature by using TECs. At the same time, the fan was turned off to ensure that the test result was solely dependent on fin temperature eliminating any effects caused by the warm air while cooling the sample down. This period is defined as pull down period (the first 2 to 4 minutes) which can be observed in Figure 5 - 1. After the pull down period, the fin temperature (T_{fin}) would reach the set point temperature and at the same time, the timer for the frosting cycle was initiated and the fan was turned on. During this pull down period, no visible amount of frost was measured on the fins, and the fan was kept at constant RPM throughout the entire test. This method of testing was preferred over a constant air velocity method since it was closer to the actual operation of the outdoor evaporator coils in air-source heat pump systems. The constant fan frequency method will result in decrease of the air inlet velocity resulting from the flow blockage on the fins once frost started to accumulate on the fin sample. According to the ASHRAE standard 41.2, the lower limit of the air velocity that could be measured with our flow nozzle was 0.7 m/s (138 ft/min). However, in order to extend the frosting period and detect a clear difference between the various frosting times, the frosting period was extended beyond the low air flow limit and up to the point at which the air flow across the fin sample was equal to or below 0.4 m/s (79 ft/min). This is approximately 26% of the initial face velocity.

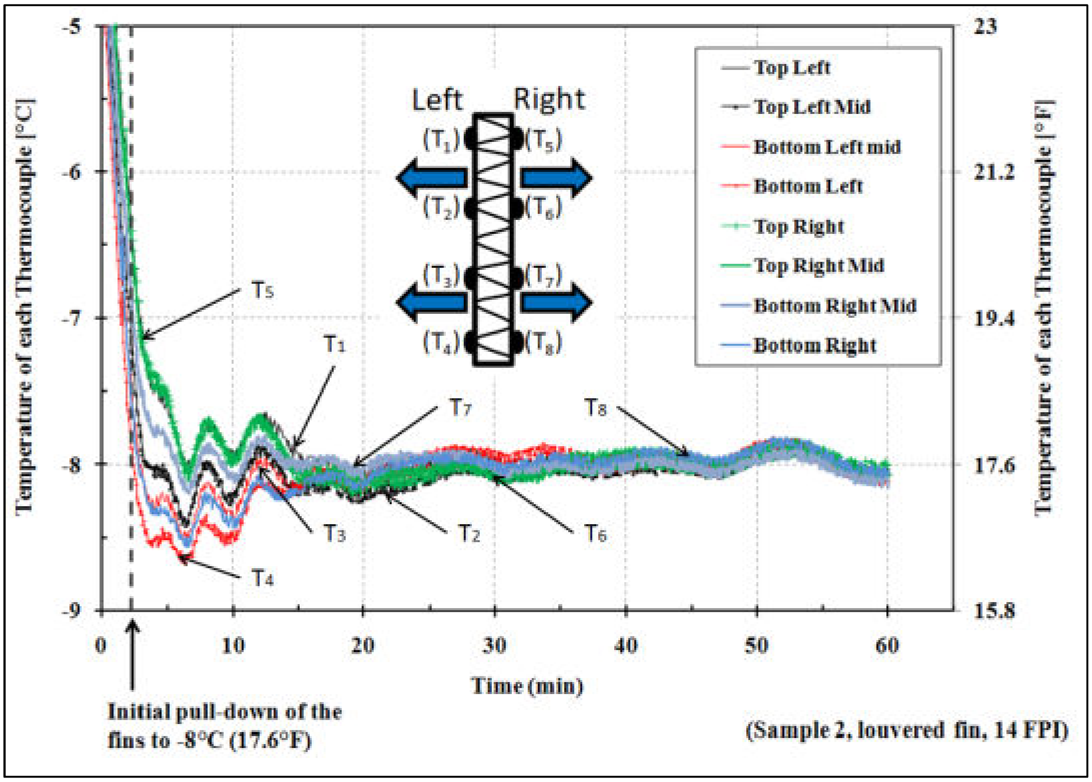

Figure 5 - 1: Example of the control of the fin temperature (Tfin) during frosting operation and pull down period of the fin sample to the set point temperature of -8°C (17.6°F) for the frosting experiment

5.3 DATA REDUCTION

As mentioned earlier, the data reduction in the experiment is mainly to investigate the heat transfer performance of the microchannel fin sample. The fin sample heat transfer rate is estimated using two different methods; enthalpy method and conduction method. The intention of utilizing two different methods is to validate the experimental setup and to ensure the estimated heat transfer rate is accurate. Several parameters used need to be estimated, i.e. mass flow rate, humidity ratio, total thermal resistance, and heat gain in the conduction side.

5.3.1 Heat transfer rate using enthalpy method

The heat transfer rate for the fin sample was calculated through enthalpy method which utilized the air side. The heat transfer rate from the air side is separated into two parts. The first part is calculating the sensible heat transfer rate, and the second part is the latent heat transfer rate. Sensible heat transfer rate is the heat transfer rate due to the change in dry bulb temperature which can be calculated by using Equation (2).

$$q_{air,sensible} = \dot{m}_{air} \cdot C_p \cdot \Delta T_{air} = \dot{m}_{air} \cdot C_p \cdot (T_{in} - T_{out})_{air} \qquad (2)$$

Where :

- $q_{sensible}$ = Sensible heat transfer rate (Watt)
- $\dot{m}$ = Mass flow rate (kg/s)
- C_p = Specific heat of air (J/kg-K)
- T_{in} = Dry bulb temperature at inlet (°C)
- T_{out} = Dry bulb temperature at outlet (°C)

Latent heat transfer rate is the heat transfer rate due to the change in state (e.g. liquid to gas) which can be calculated by using Equation (3).

$$q_{air,latent} = \dot{m}_{air} \cdot h_w \cdot \Delta W_{air} = \dot{m}_{air} \cdot h_w \cdot (W_{in} - W_{out})_{air} \qquad (3)$$

Where :

- Q_{latent} = Latent heat transfer rate (Watt)
- $\dot{m}$ = Mass flow rate (kg/s)
- h_w = Enthalpy of the condensate (J/kg)
- W_{in} = Humidity ratio at inlet (kg-water/kg-air)
- W_{out} = Humidity ratio at outlet (kg-water/kg-air)

The submission of both sensible heat transfer rate and latent heat transfer rate yields the total heat transfer rate that the sample produced as shown in Equation (**4**).

$$q_{air,total} = q_{air,sensible} + q_{air,latent} \tag{4}$$

Several parameters used in the heat transfer calculation are measured during the experiment. These parameters are the dry bulb temperature at the inlet (T_{in}) and outlet (T_{out}) of the sample. Three other parameters in the experiment are derived paramter. The humidity ratio at inlet (W_{in}) and outlet (W_{out}) are derived from the dew point temperature measurement. Another derived paramter is the air mass flow rate ($\dot{m}_{air}$), derived from the measured air volumetric flow rate. As for the air specific heat (C_p) and enthalpy of condensate (h_w), they are constant parameters dependent on the condition of the air.

5.3.1.1 Humidity ratio calculation

The air humidity ratio at inlet and outlet of the fin sample were directly calculated by the LabView program using equations from ASHRAE Fundamental. Humidity ratio (W in kg-water/kg-air) can be calculated by using the saturation pressure (p_{ws} in Pascal) and total pressure (p in Pascal) as shown in Equation (**5**).

$$W = 0.621945 \cdot \frac{p_{ws}}{p - p_{ws}} \tag{5}$$

The saturation pressure (p_{ws} in Pascal) is calculated from the dew point temperature or saturation temperature (T in Kelvin) as shown in Equation (**6**).

$$ln(p_{ws}) = C_1/T + C_2 + C_3 \cdot T + C_4 \cdot T^2 + C_5 \cdot T^3 + C_6 \cdot T^4 + C_7 \cdot ln(T) \tag{6}$$

Where:

- C_1 = -5.6745359 E+03
- C_2 = 6.3925247 E+00
- C_3 = -9.6778430 E-03
- C_4 = 6.2215701 E-07

- $C_5 = 2.0747825$ E-09
- $C_6 = -9.4840240$ E-13
- $C_7 = 4.1635019$ E+00

5.3.1.2 Mass flow rate calculation

The mass flow rate is calculated using the volumetric flow rate. As mentioned in the previous section, the air volumetric flow rate is estimated by taking the measurement of static pressure difference across the nozzle installed in the tunnel. The air volumetric flow rate (Q) in the experiment was calculated by using Equation (7) as a function of measured static pressure drop across the nozzle (Δp_{nozzle}).

$$Q = 1.414 \cdot Y \cdot \sqrt{\Delta p_{nozzle}/\rho} \cdot C \cdot A \tag{7}$$

Where :

- Q = Air volumetric flow rate (m^3/s)
- Y = Expansion factor
- Δp_{nozzle} = Static pressure difference across the nozzle (Pascal)
- ρ = Air density (kg/m^3) = 1.273 kg/m^3 taken at T = 1.667°C
- C = Nozzle discharge coefficient = 0.955[1]
- A = Area of cross section of the nozzle [m^2] (ft^2) = 7.13E-05 m^2 (0.000767 ft^2)

The Expansion factor (Y) is a function of pressure drop across the nozzle as seen in Equation(**8**).

$$Y = 1 - (0.548 + 0.71 \cdot \beta^4)(1 - \alpha) \tag{8}$$

Where:

- β = Ratio of nozzle exit diameter to approach duct diameter

$$\beta = \frac{D_{nozzle}}{D_{chamber}} = \frac{9.525\ mm}{57.15\ mm} = 0.1667 \tag{9}$$

---

[1] Table 4 in ANSI/ASHRAE 41.2-1987 (RA92)

- α = Ratio of nozzle throat total pressure to nozzle entrance total pressure

$$\alpha = 1 - \left[\frac{\Delta p}{\rho_x \cdot R \cdot (t_x + 273.2)}\right] \tag{10}$$

Where:

- Δp = Static pressure difference between before and after the nozzle (Pa)
- ρ_x = Air density (kg/m^3) = 1.273 kg/m^3
- R = Gas constant (287.1 J/kg-K)
- t_x = Air dry bulb temperature (°C) = 1.667°C

The mass flow rate ($\dot{m}$) is calculated by using the volumetric flow rate (Q) and air density (ρ) as shown in Equation (**11**).

$$\dot{m} = V \cdot A \cdot \rho = Q \cdot \rho \tag{11}$$

5.3.2 Heat transfer rate using conduction method

The heat transfer rate of the fin sample was calculated using conduction method. The heat transfer rate from the conduction side was separated into two parts. The first part was calculating the conduction heat transfer neglecting the heat gain, and the second part was the heat gain due to the temperature difference between the fin temperature and inlet air temperature. The heat transfer from conduction across the metal plates on the sides of the fin sample was calculated by assuming a quasi-steady state heat conduction process. The heat transfer is calculated by taking the temperature gradient between the fin temperature (T_{fin}) and cold side temperature (T_{cold}) as seen in Figure 18. This temperature difference along with the total thermal resistance (ΣR) of materials between the two temperatures readings were used to calculate the heat transfer rate ($q_{conduction}$) as shown in Equation (12).

$$q_{conduction} = \frac{\Delta T}{\Sigma R} = \frac{T_{fin} - T_{cold}}{\Sigma R} \qquad (12)$$

Where :

- $q_{conduction}$ = Heat transfer rate using conduction method (Watt)
- ΔT = Temperature difference (°C or K)
- T_{fin} = Temperature of the fin (°C)
- T_{cold} = Temperature of cold side of TEC (°C)
- ΣR = Total thermal resistance between the two temperature readings (1.58 K/Watt)

–

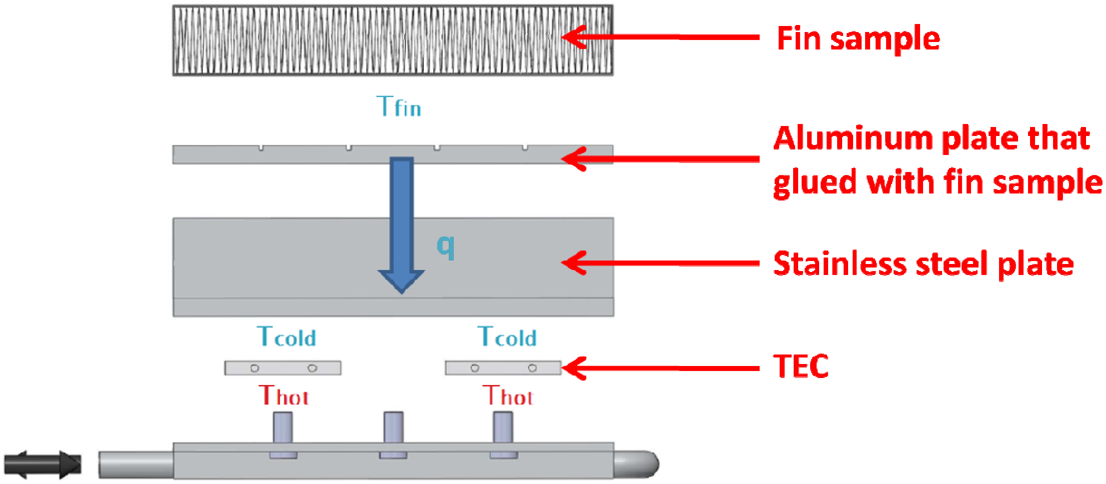

Figure 18: Conduction heat transfer

The $q_{conduction}$ above was used to calculate conduction heat transfer for each of TEC. Therefore the overall conduction heat transfer for the fin sample is the total of all four TECs' heat transfer rate.

The heat gain due to the temperature difference between the inlet air temperature and the fin temperature was investigated by conducting calorimeter test. The heat gain due to the temperature difference is summarized in Equation (13).

$$q_{conduction,gain} = (T_{air\ inlet} - T_{fin}) * 0.248 + 0.304 \qquad (13)$$

Where:

- $q_{conduction,gain}$ = Heat gain due to the temperature difference (Watt)

- $T_{air\ inlet}$ = Temperature at the inlet of the fin sample (°C)

- T_{fin} = Temperature of the fin (°C)

The total heat transfer using conduction method can be calculated using Equation (14).

$$q_{conduction,total} = q_{conduction} - q_{conduction,gain} \quad (14)$$

Several parameters used in the heat transfer calculation are measured during the experiment. These parameters are the fin temperature (T_{fin}), TEC surface temperature (T_{cold}), and dry bulb temperature at the inlet of the sample (T_{in}). While total thermal resistance (ΣR) for conduction heat transfer and the heat gain due to temperature difference between fin temperature and ambient temperature are estimated through calorimeter test which will be explained in detail in the next chapter.

5.4 UNCERTAINTY ANALYSIS

Data logger from Fluke and LabView real time data acquisition system were used to record and store the experimental data. The experimental conditions were monitored at all times by LabView Real Time control module. The sampling rate of the DAQ system is for every 4 seconds and the average values of the operating parameters were calculated from the collected data. The amount of the measurement samples was statistically large enough to reduce the error from noise, random fluctuation of the sensor output signals, and sensors response time. The measured parameters and corresponding accuracies are summarized in Table 5.

Table 5: Accuracy of instrumentations for the frost experiments

Instrumentations	Nominal range	Accuracy
Inlet air dry bulb temperature	1.11 to 2.22ºC (34 to 36°F)	± 0.67°C (1.21°F)
Inlet air dew point temperature	-0.3 to -1.6 ºC (31.46 to 29.12°F)	± 0.2°C (0.36°F)
Outlet air dry bulb temperature	3 to -11°C (37.4 to 12.2°F)	± 0.28°C (0.50°F)
Outlet air dew point temperature	-0.3 to -4.9°C (31.46 to 23.18°F)	± 0.2°C (0.36°F)
Fin temperature	-4 to -12°C (24.8 to 10.4°F)	± 0.43°C (0.77°F)
TEC surface temperature (cold side)	-8 to -14°C (17.6 to 6.8 °F)	± 0.63°C (1.13°F)
Pressure difference (flow nozzle)	0 to 450 Pa (0 to 1.81 in.H_2O)	± 40 Pa (0.16 in.H_2O)
Pressure difference .across fin sample	0 to 430 Pa (0 to 1.73 in.H_2O)	± 6.23 Pa (0.03 in.H_2O)

The accuracy of measured parameters are used to calculate the uncertainty of the derived parameters, i.g. humidity ratio and mass flow rate. The accuracy of measured parameters and uncertainty of derived parameters are used to estimate the overall uncertainty of the heat transfer rate.

5.4.1 Uncertainty of humidity ratio

The air humidity ratio at inlet and outlet of the fin sample is estimated from the dew point temperature measurement described in previous section. The source of uncertainty for humidity ratio is the accuracy of the dew point meter (±0.2°C or 0.36°F). The uncertainty was calculated using uncertainty propagation calculation in Enginnering Equation Solver (EES). The uncertainty was calculated within the operating range and the result is ±1.67% of the humidity ratio reading as seen in Table 6 below.

Table 6: Uncertainty of humidity ratio

T_{dew}				Humiditiy ratio (W)		% Uncertainty
°C		°F		kg water/kg air or lb water/lb air		
Value	Uncertainty	Value	Uncertainty	Value	Uncertainty	
-0.34	0.2	31.39	0.36	0.00367	0.000061	1.66
-0.48	0.2	31.13	0.36	0.00363	0.000060	1.66
-0.63	0.2	30.87	0.36	0.00358	0.000060	1.66
-0.77	0.2	30.61	0.36	0.00354	0.000059	1.67
-0.92	0.2	30.35	0.36	0.00350	0.000058	1.67
-1.07	0.2	30.08	0.36	0.00345	0.000058	1.67
-1.21	0.2	29.82	0.36	0.00341	0.000057	1.67
-1.36	0.2	29.56	0.36	0.00337	0.000056	1.67
-1.50	0.2	29.30	0.36	0.00333	0.000056	1.67
-1.65	0.2	29.04	0.36	0.00329	0.000055	1.68

5.4.2 Uncertainty of air face velocity

The face velocity in the experiment is calculated from the volumetric flow rate and frontal area of the fin sample as seen in Equation (1). The air volumetric flow rate is estimated from static pressure difference as described in the previous section. Therefore, the main parameter that affects the uncertainty is the accuracy of pressure transducer is ±40 Pa (0.16 in.H_2O). The uncertainty analysis was done by using the experimental data from fin sample 2 with -5°C fin temperature. The uncertainty was calculated in EES program. The result of the uncertainty analysis can be seen in Table 7. At the beginning of the test, the uncertainty of air face velocity was estimated to be ±4.5% of the reading. As the face velocity decreased the uncertainty increased and reached ±63% at the end of the test. The uncertainty of the face velocity increased significantly towards the end of the frosting test because the pressure readings across the nozzle became considerably smaller than the full scale range of the pressure transducer. The uncertainty of the pressure transducer had a significant impact on the air face velocity measurements if the air flow velocity during the frosting period reduced to more than 50% of its initial value at the beginning of the test.

Table 7: Uncertainty of air face velocity

Δp				Face velocity (mdot)				% face velocity	% uncertainty
Pa		Inch H2O		m/s		ft/min			
Value	Uncertainty	Value	Uncertainty	Value	Uncertainty	Value	Uncertainty		
444.6	40.06	1.78	0.16	1.497	0.067	295	13	100.00	4.48
452.1	40.06	1.82	0.16	1.510	0.067	297	13	100.87	4.41
448.2	40.06	1.80	0.16	1.503	0.067	296	13	100.40	4.45
440	40.06	1.77	0.16	1.490	0.067	293	13	99.53	4.53
442.8	40.06	1.78	0.16	1.494	0.067	294	13	99.80	4.50
436.7	40.06	1.75	0.16	1.484	0.068	292	13	99.13	4.57
433.6	40.06	1.74	0.16	1.479	0.068	291	13	98.80	4.60
426.4	40.06	1.71	0.16	1.466	0.069	289	13	97.93	4.68
417.4	40.06	1.68	0.16	1.451	0.069	286	14	96.93	4.78
404.6	40.06	1.62	0.16	1.428	0.070	281	14	95.39	4.93
376.9	40.06	1.51	0.16	1.379	0.073	271	14	92.12	5.29
353.2	40.06	1.42	0.16	1.335	0.075	263	15	89.18	5.65
324.9	40.06	1.30	0.16	1.281	0.079	252	15	85.57	6.14
301.4	40.06	1.21	0.16	1.234	0.082	243	16	82.43	6.63
269.5	40.06	1.08	0.16	1.167	0.087	230	17	77.96	7.41
228.5	40.06	0.92	0.16	1.075	0.094	212	19	71.81	8.75
177.6	40.06	0.71	0.16	0.948	0.107	187	21	63.31	11.27
137.4	40.06	0.55	0.16	0.834	0.122	164	24	55.69	14.60
106.5	40.06	0.43	0.16	0.734	0.139	145	27	49.04	18.86
63.5	40.1	0.25	0.16	0.567	0.181	112	36	37.87	31.95
33.52	40.06	0.13	0.16	0.412	0.259	81	51	27.52	62.94

5.4.3 Uncertainty of heat transfer rate

The uncertainty analysis for heat transfer rate is done for both methods (enthalpy method and conduction method). Experimental data for fin sample 2 with -5°C (23°F) fin temperature was used to analyze the uncertainty of the heat transfer rate.

5.4.3.1 Uncertainty of heat transfer rate using enthalpy method

The heat transfer rate calculated using enthalpy method is dependent on the accuracy of the air side measurement. In the ESS calculation, uncertainty of each parameters was included for the estimation of the overall uncertainty in the heat transfer rate using enthalpy method. The uncertainty is listed in Table 8 below.

Table 8: Uncertainty of different parameters for enthalpy method

Parameters	Uncertainty
ΔP for flow rate calculation	±40 Pa (0.16 in. H2O)
Dry bulb temperature at inlet	± 0.67°C (1.21°F)
Dry bulb temperature at outlet	± 0.28°C (0.5°F)
Humidity ratio at inlet	± 1.67%
Humidity ratio at outlet	±1.67%

The frosting test on sample 2 with -5°C (23°F) fin temperature last for 48 minutes. For simplification, in the EES calculation, only 20 data points out of the 48 minutes test with increment of approximately 2.4 minutes were used. The result of the uncertainty analysis done by EES code can be seen in below. From the table below, the uncertainty of the heat transfer is slightly higher at the beginning of the test due to the fact that the air side temperature difference across the fin sample was smaller. As the fan started and pulled the air flow into the fin sample, air accelerated to full speed and exchanged heat with the fins. Due to the thermal inertia of the test apparauts few minutes were needed before a quasi-steady state conditions was achieved. As soon as the air at the inlet reached a quasi-steady state, the uncertainty was about 12%. The uncertainty was also dependent on the control of the TECs that was used to set the conditions for the fin temperature. The uncertainty varied beween 10% to 13% during the majority of the frosting experiments. Towards the end of each test, the uncertainty of heat transfer rate became significantly larger due to the effect of the uncertainty in flow rate measurements. The average uncertainty throughout the entire test period was approximately 16.5%.

Table 9: Uncertainty of heat transfer rate (enthalpy method)

Time (min)	% flow rate	q_{total}				% uncertainty
		Watt		Btu/hr		
		Value	Uncertainty	Value	Uncertainty	
0.0	100.00	12.31	1.843	42.00	6.29	14.97
2.5	100.88	18.74	1.943	63.94	6.63	10.37
4.8	100.44	18.39	1.931	62.75	6.59	10.50
7.2	99.52	17.74	1.908	60.53	6.51	10.76
9.6	99.82	16.8	1.894	57.32	6.46	11.27
12.1	99.12	15.75	1.87	53.74	6.38	11.87
14.4	98.77	14.93	1.854	50.94	6.33	12.42
16.9	97.94	14.29	1.834	48.76	6.26	12.83
19.3	96.94	13.88	1.815	47.36	6.19	13.08
21.7	95.45	13.49	1.792	46.03	6.11	13.28
24.0	92.12	13.84	1.769	47.22	6.04	12.78
26.4	89.19	14.17	1.752	48.35	5.98	12.36
28.8	85.56	13.99	1.723	47.74	5.88	12.32
31.2	82.41	13.69	1.7	46.71	5.80	12.42
33.6	77.94	13.37	1.683	45.62	5.74	12.59
36.0	71.77	12.88	1.685	43.95	5.75	13.08
38.5	63.33	12.07	1.752	41.18	5.98	14.52
40.9	55.71	11	1.877	37.53	6.40	17.06
43.3	49.06	9.623	2.007	32.84	6.85	20.86
45.7	37.87	7.7	2.5	26.26	8.68	33.07
47.9	27.53	6.078	3.855	20.74	13.15	63.43

5.4.3.2 Uncertainty of heat transfer rate using conduction method

The heat transfer rate using conduction method is mainly dependent on the accuracy of the thermocople readings. In the ESS calculation, uncertainty on each parameter was included to estimate the overall uncertainty in the heat transfer rate. The uncertainty is listed in Table 10 below.

Table 10: Uncertainty of different parameters for conduction method

Parameters	Uncertainty
Dry bulb temperature at inlet	± 0.67°C (1.21°F)
Temperature at the cold side of TEC	± 0.63°C (1.13°F)
Temperature of the fin	± 0.43°C (0.77°F)

Identical to the enthalpy method, the uncertainty analysis for conduction method only took 20 data point with increment of 2.4 minutes. The result of the uncertainty analysis by EES code can be seen in Table 11 below. As seen in the table, the uncertainty of the heat transfer rate is a constant number throughout the test. This causes the % uncertainty to be low at the beginning of the test. On the other hand, once the frost starts accumulating on the fin sample the ammount of cooling load required to maintain the fin temperature become less, hence the % uncertainty increased accordingly. The average % uncertainty throughout the entire test is approximately 8%.

Table 11: Uncertainty of heat transfer rate (conduction method)

Time (min)	% flow rate	q_{total}				% uncertainty
		Watt		Btu/hr		
		Value	Uncertainty	Value	Uncertainty	
0.0	100.00	16.72	1.01	57.05	3.45	6.05
2.5	100.88	18.00	1.01	61.42	3.45	5.62
4.8	100.44	18.50	1.01	63.12	3.45	5.46
7.2	99.52	17.24	1.01	58.83	3.45	5.86
9.6	99.82	16.54	1.01	56.44	3.45	6.11
12.1	99.12	13.62	1.01	46.47	3.45	7.42
14.4	98.77	13.55	1.01	46.23	3.45	7.46
16.9	97.94	12.92	1.01	44.08	3.45	7.83
19.3	96.94	12.85	1.01	43.85	3.45	7.87
21.7	95.45	13.13	1.01	44.80	3.45	7.70
24.0	92.12	14.21	1.01	48.49	3.45	7.11
26.4	89.19	13.79	1.01	47.05	3.45	7.33
28.8	85.56	13.44	1.01	45.86	3.45	7.52
31.2	82.41	13.57	1.01	46.30	3.45	7.45
33.6	77.94	13.62	1.01	46.47	3.45	7.42
36.0	71.77	13.37	1.01	45.62	3.45	7.56
38.5	63.33	12.72	1.01	43.40	3.45	7.95
40.9	55.71	10.00	1.01	34.11	3.45	10.11
43.3	49.06	8.72	1.01	29.76	3.45	11.59
45.7	37.87	8.26	1.01	28.17	3.45	12.24

5.5 CONCLUSION

This chapter describes the test procedure, data reduction, and uncertainty analysis of the experiment. The test procedure explains in details the method used to conduct every frost experiment. The data reduction demonstrates method used to compute heat transfer rate of the microchannel fin sample. Lastly, the uncertainty analysis is done for the heat transfer performance. The result of the uncertainty is summarized in Table 12 below.

Table 12: Summary of Uncertainty Analysis

Parameters	Uncertainty
Fin temperature	± 0.43°C (0.77°F)
TEC surface temperature (cold side)	± 0.63°C (1.13°F)
Inlet air condition	
- Inlet dry bulb temperature	± 0.37°C (0.67°F)
- Inlet humidity ratio	± 1.67%
Air mass flow rate/Air volumetric flow rate/Air face velocity	
- ΔP nozzle	± 40 Pa (0.16 in. H2O)
- Uncertainty at the beginning	±4.49%
- Uncertainty at the end	± 62.93%
Outlet air condition	
- Outlet dry bulb temperature	± 0.28°C (0.50°F)
- Outlet humidity ratio	± 1.67%
Pressure drop	± 6.2 Pa (0.02 in. H2O)
Frost thickness	± 0.03 mm (1.2×10^{-3} in)
Frost mass	± 0.2 gr (0.44×10^{-3} lb)
Heat transfer rate	
Enthalpy method	
- Uncertainty at the beginning	± 12%
- Uncertainty at the end	± 63%
- Average uncertainty	± 16.5%
Conduction method	
- Uncertainty at the beginning	± 6%
- Uncertainty at the end	± 12%
- Average Uncertainty	± 8%

CHAPTER VI

EXPERIMENTAL VALIDATION

6.1 INTRODUCTION

The verifications on the instrumentation accuracy, signal processing, and data recording were demonstrated through two steps. The first step was by performing calorimeter tests on the test apparatus. This calorimeter test are intended to verify that all the sensors were properly installed, and connected to DAQ system used in the lab. Additionally, the tests were done to obtain total thermal resistance and heat gain due to temperature difference that used in heat transfer rate (conduction method) as explained in the previous chapter. The second step of experimental validation was done by performing heat balance test. The heat balance tests were performed on one of the fin sample. This test was intended to verify the heat balance between heat transfer using conduction method and enthalpy method.

6.2 CALORIMETER TESTS

Calorimeter tests were performed on the experimental apparatus at the early phase of this project. The main objective for calorimeter tests was to ensure the connectivity of the instrument to the data acquisition system used in the experiment was good. The calorimeter tests were performed in two different tests. The first test was done to measure the thermal resistance of the experimental setup, while the second one was performed to obtain the correlation of heat gain due to temperature difference between fin temperature and inlet air temperature. Both the thermal resistance and heat gain correlation were used in the heat transfer rate (conduction method) calculation.

6.2.1 Measurement of thermal resistance (R)

The first step on the calorimeter test was done to obtain the total thermal resistance (ΣR). The total thermal resistance (ΣR) that estimated in this test was compute for materials in between T_{fin} and T_{cold}. The test was conducted directly on the actual test apparatus with using fin sample number 3 without any airflow passing through the fin sample. An electrical heater was used in this test. The electrical heater was connected to volt meter to monitor the power consumption.. The overall test setup is illustrated in Figure 19.

The test procedures used for the test are:

1. Installed the heater at one side of the fin sample.
2. Insulated the entire assembly to prevent heat loss to the ambient air.
3. Started the DAQ system to start monitoring and recording the fin temperature (T_{fin}) and TEC surface temperature (T_{cold}).
4. Powered the electrical heater to 5 watts and wait for the temperature readings to reach steady state.
5. Kept the test to run for a period of time while all the temperature readings are recorded.
6. Analyzed the collected data to calculate for the total thermal resistance (ΣR) using Equation (15) with assumption that the power consumed by the electrical heater was fully converted to heat (q).

$$\boldsymbol{\Sigma R} = \frac{\boldsymbol{T_{fin} - T_{cold}}}{\boldsymbol{q_{electrical}}} = \frac{\boldsymbol{T_{fin} - T_{cold}}}{5\,Watts} \tag{15}$$

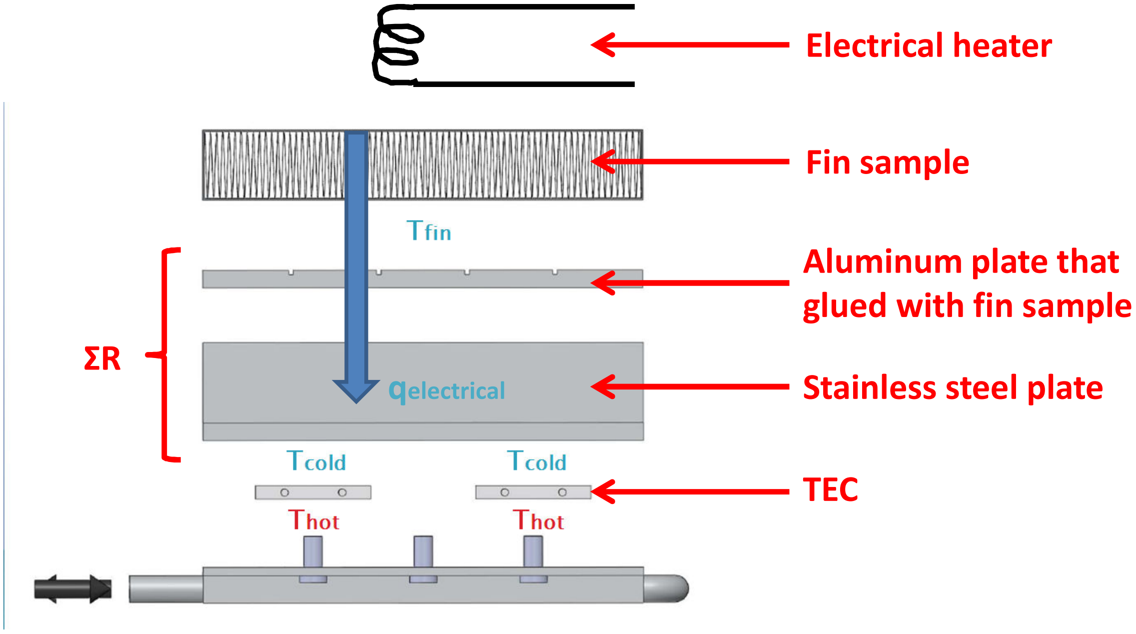

Figure 19: Calorimeter test to estimate the total thermal resistance

The test result showed that the DAQ system worked flawlessly in recording 12 hours of data continuously. The temperature difference between the T_{fin} and T_{cold} during the calorimeter test showed a constant 3.93°C (39.07°F). Using Equation (15), the total thermal resistance (ΣR) from the calorimeter tests was calculated to be 0.79 K/Watt (0.42 R-hr/Btu). As seen in Figure 19, the total thermal resistance obtained in this test is for both of the TECs. Therefore, to modify the thermal resistance for calculating the heat transfer rate for one of TEC is by multiplying the experimental ΣR value by 2 which become 1.58 K/Watt (0.83 R-hr/Btu). This ΣR value was used to calculate the heat transfer rate (conduction method) for all the fin samples tested in the experiment.

6.2.2 Measurement of heat gain

The second step of calorimeter test was done to investigate the heat gain of the test apparatus for the conduction heat transfer. The heat gain is introduced into the test apparatus because of the fin temperature that is colder than the ambient temperature. The heat gain in the calorimeter test was estimated by the relation of temperature difference between the T_{cold} and T_{fin}. The test was conducted in the similar manner as the frosting test. The fan inside the tunnel was turned on to simulate the airflow passing through the fin sample. The difference between the frosting test and this test is the fin sample was heated using the electrical heater with the same configuration as the previous calorimeter test (Figure 19).

The test procedures used for this test are:

1. Installed the heater at one side of the fin sample.
2. Insulate the entire assembly to prevent heat gain to the ambient air.
3. Started the DAQ system to start monitoring and recording temperatures and flow rate across the fin sample.
4. Turned the fan inside the tunnel and adjust the fan to provide air face velocity of 1.5 m/s (295 ft/min) on the fin sample which is the exact same condition on the actual frost test. The air condition inside the tunnel was kept at the ambient condition throughout the test.
5. Powered the electrical heater to 5 watts (17.1 Btu/hr) and wait for the temperature readings to reach steady state.
6. Kept the test to run for a period of time while all the temperature readings are recorded.
7. Analyzed the collected data using method introduced below.

The data processing is done by following these steps:

1. Extracted the inlet air temperature (T_{in}), fin temperature (T_{fin}) and TEC surface temperature (T_{cold}) from the data.
2. Calculate the heat transfer rate using Equation (12) with ΣR equal to 0.79 K/W (0.42 R-hr/Btu).
3. As mention in the test procedure, the electrical heater's input was set to 5 Watts. Using the calculated heat transfer in step 2 and 5 Watts of heat input, the heat gain can be calculated as shown in Equation (16) below.

$$q_{conduction,gain} = q_{conduction} - 5\,Watts\ (17.1\ \text{Btu/hr}) \tag{16}$$

The overall heat gain calculated above was calculated only for half of the test apparatus. Therefore, the heat gain was multiplied by 2 to consider the heat gain for the overall test apparatus.

4. The temperature difference between the fin temperature (T_{fin}) and inlet air temperature (T_{in}) was calculated.
5. The heat gain and the temperature difference calculated in step 3 and 4 were plotted as shown in Figure 20.
6. The function between heat gain with temperature difference was estimated using the curve fit.

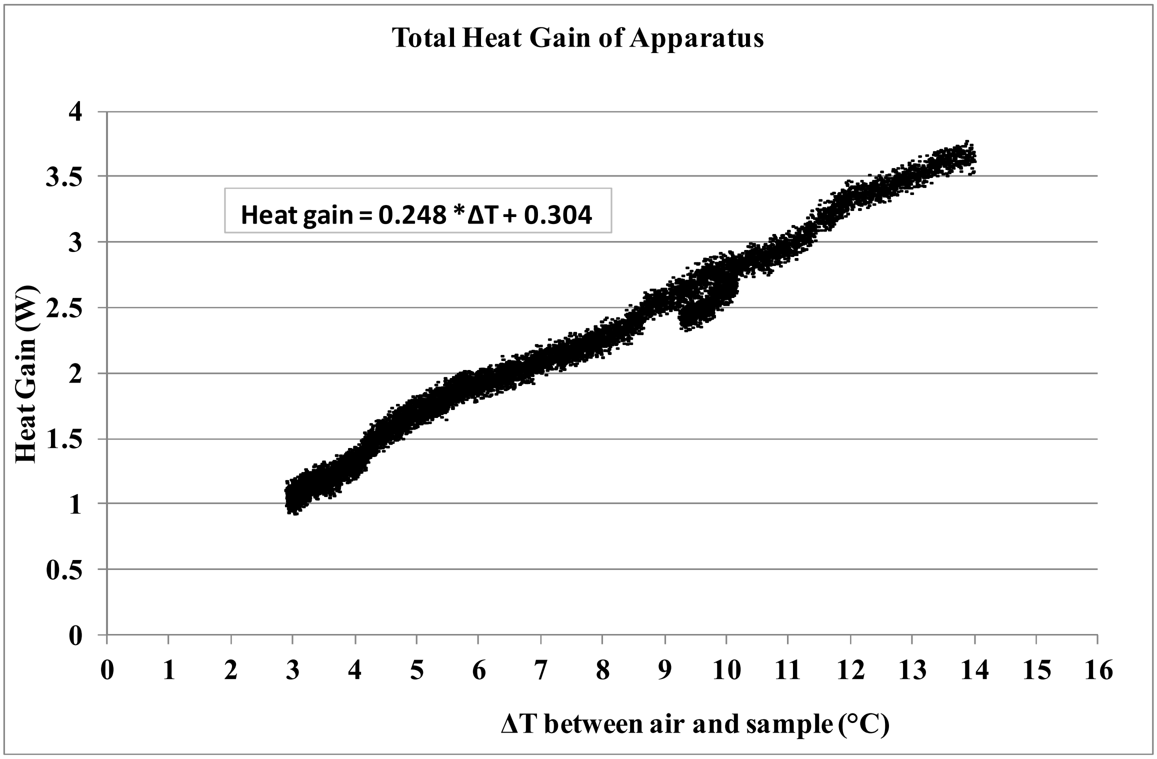

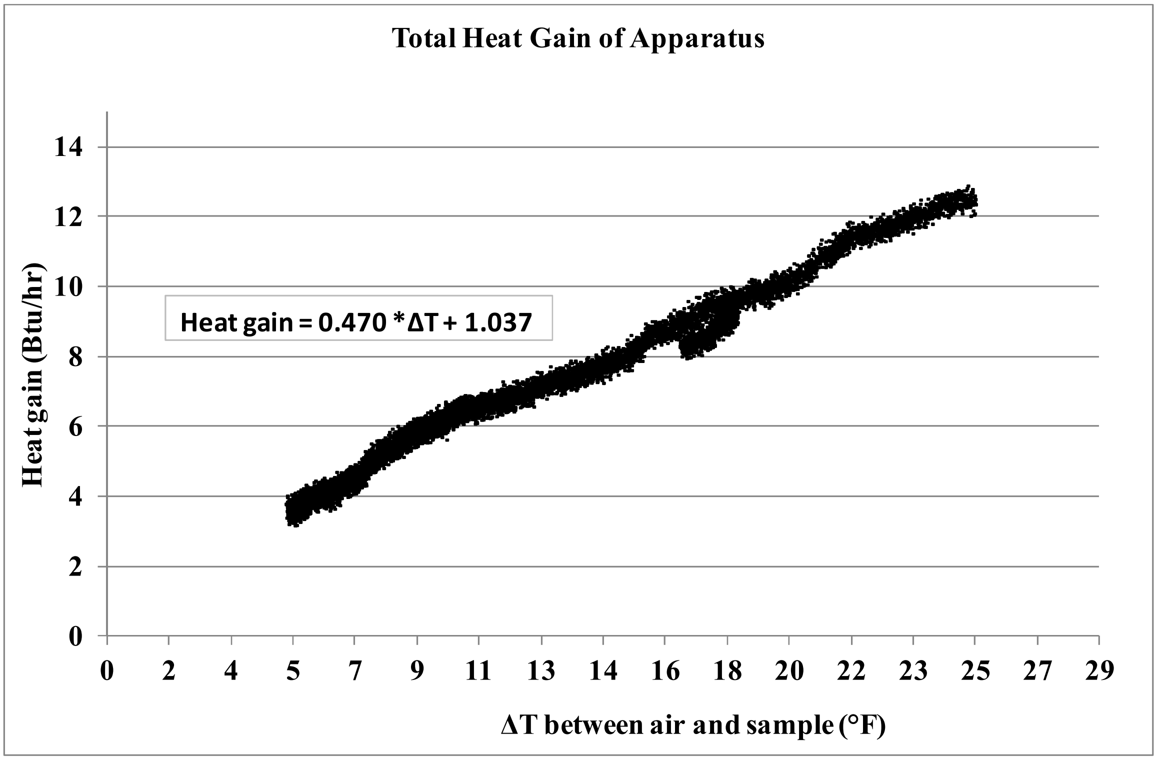

Figure 20: Heat gain of apparatus with function of temperature difference

The function between heat gain and temperature difference can be seen in Figure 20.

6.3 HEAT BALANCE TEST

Heat balance test for the experimental measurement validation was done on fin sample 2. The heat balance is calculated using Equation (17) shown below.

$$\boldsymbol{Heat\ balance}\ (\%) = \frac{q_{conduction,total} - q_{air,total}}{q_{conduction,total}} \times 100\% \tag{17}$$

The heat balance test was performed on two tests of sample 2. These tests were dry test and frost test. The dry test was performed by cooling the fin sample while keeping the fin sample dry (without frost deposition on the fin) throughout the test period. On the other hand, the frost test was performed by cooling the fin sample to the set fin temperature and allows the frost to grow on the fin sample as described in the previous chapter.

6.3.1 Heat balance on dry test

Heat balance balance for the dry test in the early stage of the project is imporant because it can used as one of the tool to evaluate the accuracy of heat transfer measurement used in the experiment. The dry test is done in the similar manner with the frosting test described in the testing procedure. The only difference is that in the dry test, the fin sample is kept dry throughout the experiment. The fin sample was cooled until the difference between fin temperature and inlet dry bulb temperature is approximately 10°C (50°F). The air temperature at the inlet of the fin sample was kept at the ambient temperature approximately at 22 to 24°C (71.6 to 75.2°F) by not conditioning the air inside the tunnel. Once the test had reached steady state condition, the test was continued for one hour while the data was recorded. The preliminary dry test was conducted on fin sample 2. The test condition for dry test is shown in Table 13 below.

Table 13: Dry test condition

Test condition	Set point
Dry bulb temperature at inlet	22.5°C (72.5°F)
Humidity ratio at inlet	0.0058 kg-water/kg-air
Fin temperature	12.5°C (54.5°F)
Air face velocity	1.5 m/s (295 ft/min)

The calculation of heat transfer rate for both enthalpy and conduction methods are explained in detail in the previous chapter for data reduction. The heat transfer rate during the dry test is presented in Figure 21 below. It is shown that the heat transfer rate calculated using both methods are close to each other.

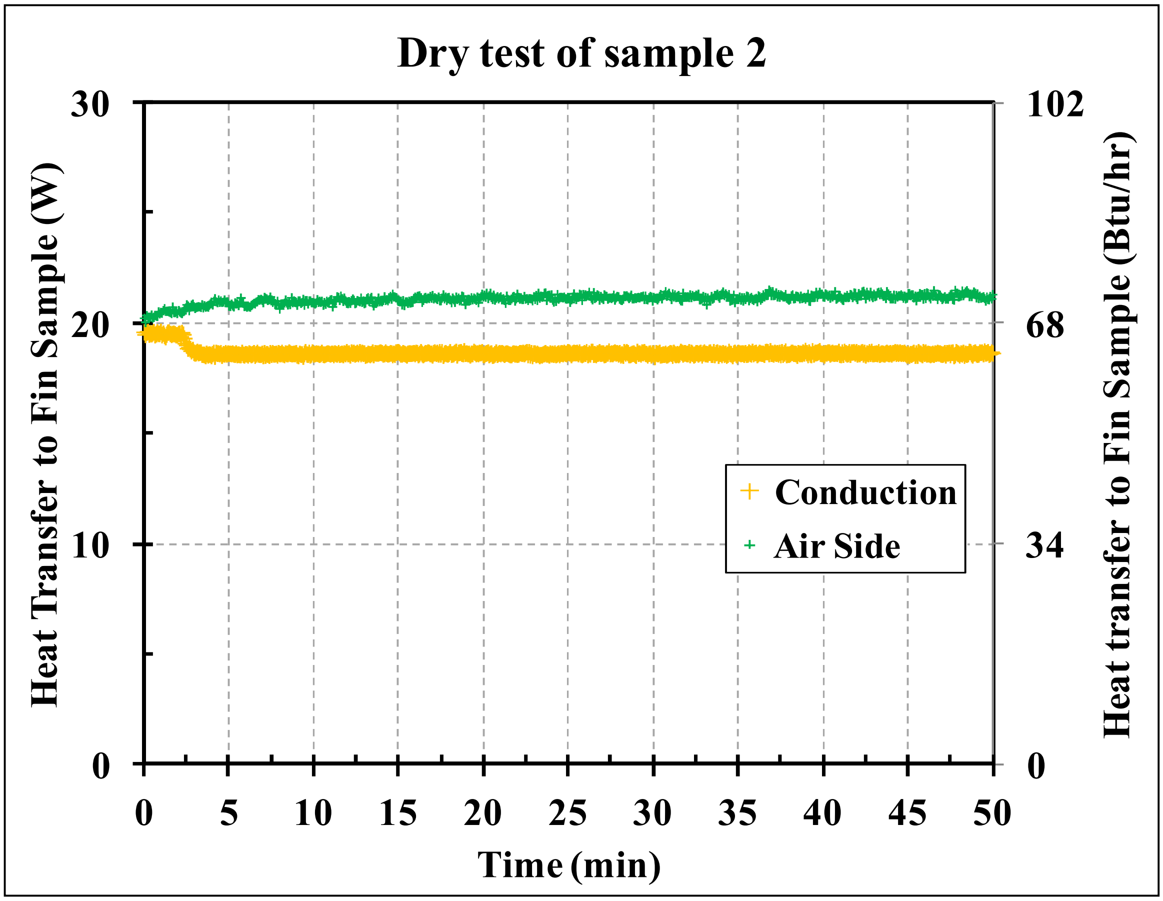

Figure 21: Heat transfer rate for dry test (sample 2)

The heat balance on the dry test is calculated using Equation (17) and the result is shown in Figure 22. The heat balance in the dry test is pretty constant after the test reach steady state condition and the average value of the heat balance throughout the test is about 13%. This value of heat balance is acceptable for our experiment because the heat transfer rate measured during the experiment is really small. Moreover, the uncertainty for each method is pretty big (8% for conduction method and 10% for entalpy method).

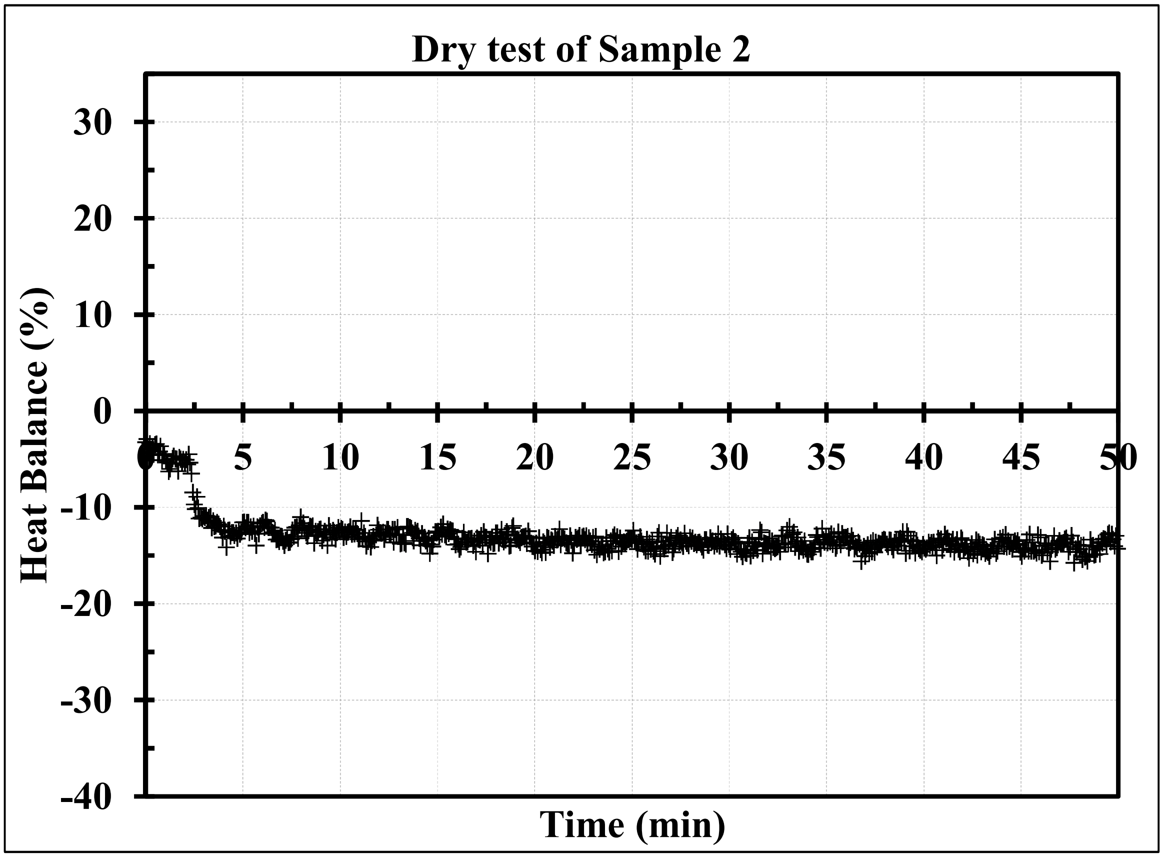

Figure 22: Heat balance for dry test (sample 2)

6.3.2 Heat balance on frost test

Additional heat balance test was performed on frost test for fin sample 2. Frost test is the typical test that was conducted in this experiment as described in test procedure section. The test was carried out by maintaining the sample's fin temperature at the desired condition while keeping the ambient air at the set point. The selected condition for both fin temperature and ambient air would allow the frost growth on the fin sample. The test was performed until the frost on the microchannel has blocked the airflow passage and reduced the airflow rate to 25% of the initial flow rate. In the experimental validation, additional heat balance for frost test is crucial because it would indicate the different performance of heat transfer measurement during the frost test comparing to the dry test. The test condition for frost test is shown in Table 13 below.

Table 14: Frost test condition

Test condition	Set point
Dry bulb temperature at inlet	1.67°C (35°F)
Humidity ratio at inlet	0.00348 kg-water/kg-air
Fin temperature	-5°C (23°F)
Air face velocity	1.5 m/s (295 ft/min)

The calculation of heat transfer rate for both enthalpy and conduction methods are explained in detail in the previous chapter for data reduction. The heat transfer rate during the dry test is presented in Figure 23 below. It is shown that the heat transfer rate calculated using both methods are similar. The heat transfer rate using conduction method is less stable due to the method of calculation assumming the steady state condition. Additionally, conduction heat transfer is also heavily dependent on the control of TEC. For example, the suddent drop in heat transfer at minutes 43 is the effect of reduction of the TECs capacity momentarilly to maintain the condition of fin temperature.

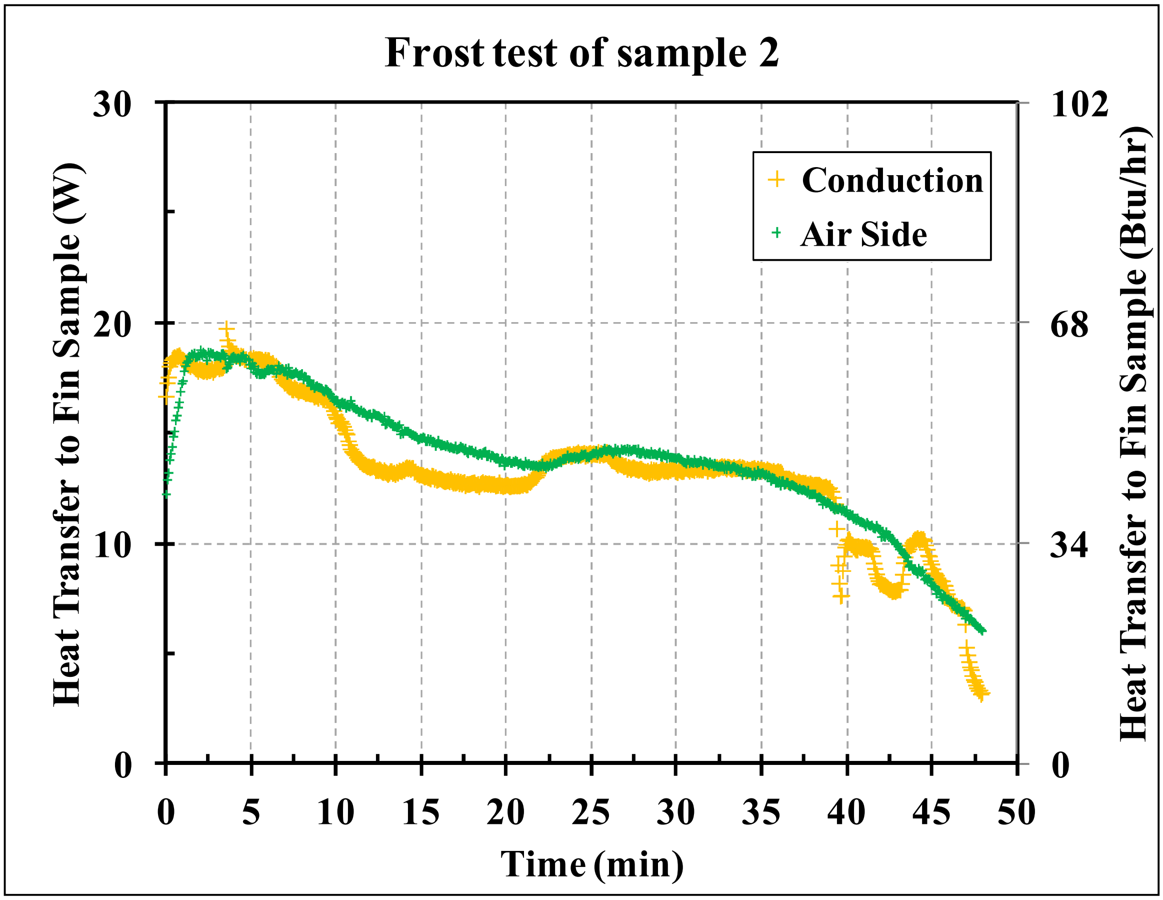

Figure 23: Heat transfer rate for frost test (sample 2)

The heat balance on the dry test is calculated using Equation (17) and the result is shown in Figure 24. There are more fluctuation observed in the heat balance for frosting test in comparison with the dry test. This phenomena is expected because the nature of frosting test that is transient. Moreover the control on the TEC affect the heat balace significantly. Due to the test procedure that requires the fin temperature to be constant throughout the test, whenever the drastic adjustment was done to the TEC (turning the TEC on or off significantly), the conduction heat transfer will changed significantly as seen in Figure 23 at minutes 43. The conduction heat transfer at this point drop significantly because the power supply to the TEC was turned off momentarilly and hence the heat balance was increased from about 5% to -30%. Aside from the heat balance fluctuation due to TEC control, the overall heat balance during the entire frost test period is within ±10% which consider to be pretty good.

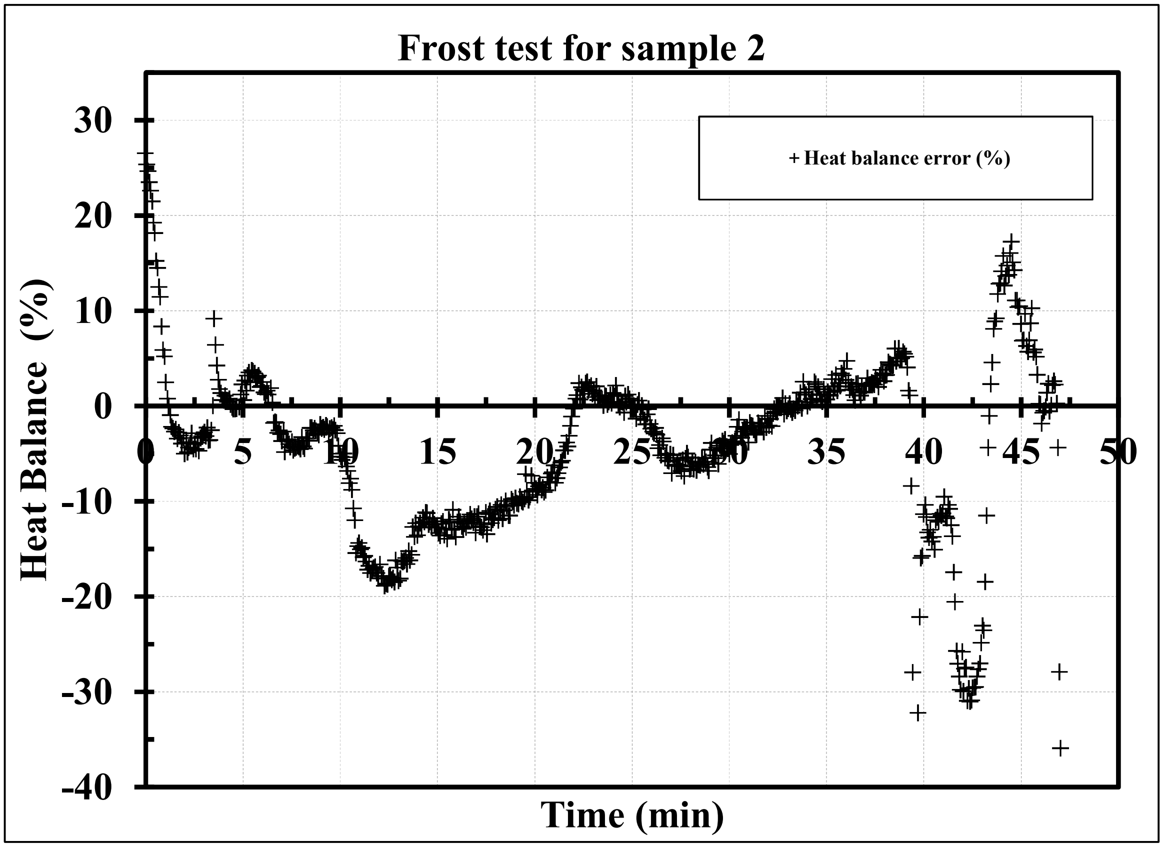

Figure 24: Heat balance for dry test (sample 2)

As mentioned in the earlier section, the heat transfer rate for the conduction method is calculated by assuming steady state condition while the actual state during the frosting experimenet was transient and dynamic. The steady state assumption was used in this experiment to reduce the complexity of the heat transfer calculation. Due to this assumption, the conduction heat transfer rate experiences a time delay compared to the air side heat transfer. To compensate for the time delay, the comparison between air side heat transfer and conduction heat transfer is done through integration of the capacity curve over time. The integration of conduction heat transfer rate is 10.65 W·hr (36.34 Btu) and the air side heat transfer rate is 11.08 W·hr (37.81 Btu). The comparison between the two methods shows 4% difference, despite the luctuation in the instantanoues heat balance curve. This comparision demonstrates that heat transfer rate measured during the frosting experiments were accurate.

6.4 CONCLUSION

The experimental validation that perfomed through calorimeter tests and heat balance tests showed that the installed sensors and DAQ system performed flawlessly throughout all of the tests. The calorimeter tests provided crucial information for heat transfer rate calculation using conduction method. The tests provided the total thermal resistance of the experimental setup which used in the conduction heat transfer rate (neglecting heat gain) and also the heat gain of the experimental setup with a function of temperature difference. Additionally, the heat balance tests were performed for dry test and frost test in one of the fin sample. The heat balance tests revealed the accuracy of heat transfer measurement in both steady state condition (dry test) and transient condition (frost test). The heat balance tests also showed that the entalpy method to calculate heat transfer rate for the fin sample is preffered. The frost test in sample 2 shown that the conduction heat transfer experienced time delay due to the method of calculation, and it is also heavily dependent on the the control of the TEC. Hence, the heat transfer rate curve had significant fluctuation in comparison to the enthalpy method.

CHAPTER VII

TEST RESULTS AND DISCUSSION

Frost growth on louvered folded fins was investigated by conducting a series of experiments in a parametric fashion and by varying the fin temperature, air inlet humidity, and air inlet face velocity such that only one variable was modified at a time while all other operating parameters were unvaried. A summary of the test conditions during the experiments is provided in Table 3.

7.1 IMPACT OF FIN TEMPERATURE ON FROSTING PERFORMANCE

The effect of fin temperature on the frost thickness growth for sample 4 is shown in Figure 25. The frost thickness is measured on the front leading edge of the fin, and it was the main parameter that caused air flow blockage. On the back side of the fins, on their trailing edges, there was no visible frost for the entire frosting period or for all the samples. This observation suggested that the blockage of the airflow occurred at the front face of the coils. Data of Figure 25 shows that decreasing the fin temperature results in decreasing of frosting time. The frosting time was defined as the time measured right after the pull down period, that is, from the instant the fins reached the set point temperature at the beginning of the test, to the instant the air velocity decreased below 0.25 m/s (50 fpm). For this test, the fin temperatures were -11, -8, and -5°C (12, 17.6, and 23°F), and the frosting times were 13 minutes for -11°C (12°F) fin temperature, 25 minutes for the -8°C (17.6°F) fin temperature and about 80 minutes for the

-5°C(23°F) fin temperature. The test at T_{fin}= -8°C (17.6°F) was selected as the baseline case since previous work suggested that this surface temperature is the closest one to the fin surface temperature in actual outdoor evaporators coils with microchannel heat exchangers during frosting conditions specified in the AHRI standards (Heating test conditions at 35/33 db/wb). The data in Figure 25 show that if the fin temperature is decreased by 3°C (~5.4°F), the frosting time is reduced by approximately 80%, that is, from 25 to 13 minutes. The fin thickness on the leading edge at the end of the frosting period was about 0.58 mm (0.020 inches) and the measurement error, which was fairly constant for all data points, is reported only for one data point in Figure 25 for clarity. The data at - 5°C (23°F) fin temperature were quite surprising. Although frost started to accumulate rapidly at the beginning of the test there is a clear variation of the slope in the thickness data for the - 5°C (23°F) case. At this fin temperature the frosting time is significantly extended. This is likely due to the fact that the actual temperature of the fin edge might be quite close to the freezing point for a fin-base temperature of - 5°C (23°F). In addition there seems to be a frost densification effect near the freezing point as confirmed by the frost mass measurements reported next in Figure 26.

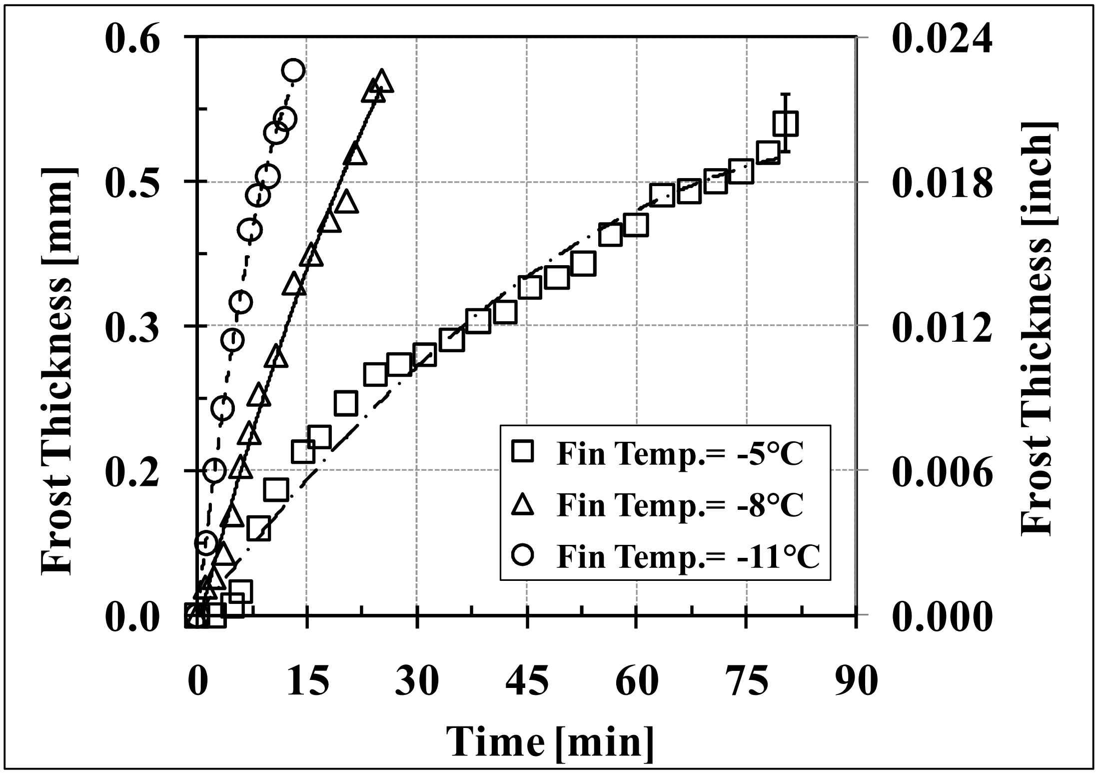

Figure 25: Frost thickness on fin sample 4 for different fin temperature.

The mass of frost grows linearly with time as shown in Figure 26. For a fin temperature of -8°C (17.6°F) there are four different data points, which were taken at different time intervals. All data points lie near a linear trend with no measurable time delay for the formation of the frost on the fin surfaces. This result suggests that the water vapor in the air stream immediately starts frosting on the fin surfaces. At the lowest fin temperature of -11°C (12°F) the frost weight at the end of the frosting period was about 3 grams while at the highest fin temperature of -5°C (23°F) the frost weight was more than 6 grams. This result is consistent with the previous findings from the literature (Yonko and Sepsy 1967; Hayashi et al. 1977; Östin and Andersson 1991; Mao et al. 1992; Mao et al. 1993; Sahin 1994) and support the fact that there is a densification phenomenon of the frost when the surface of the fins is just below the freezing point.

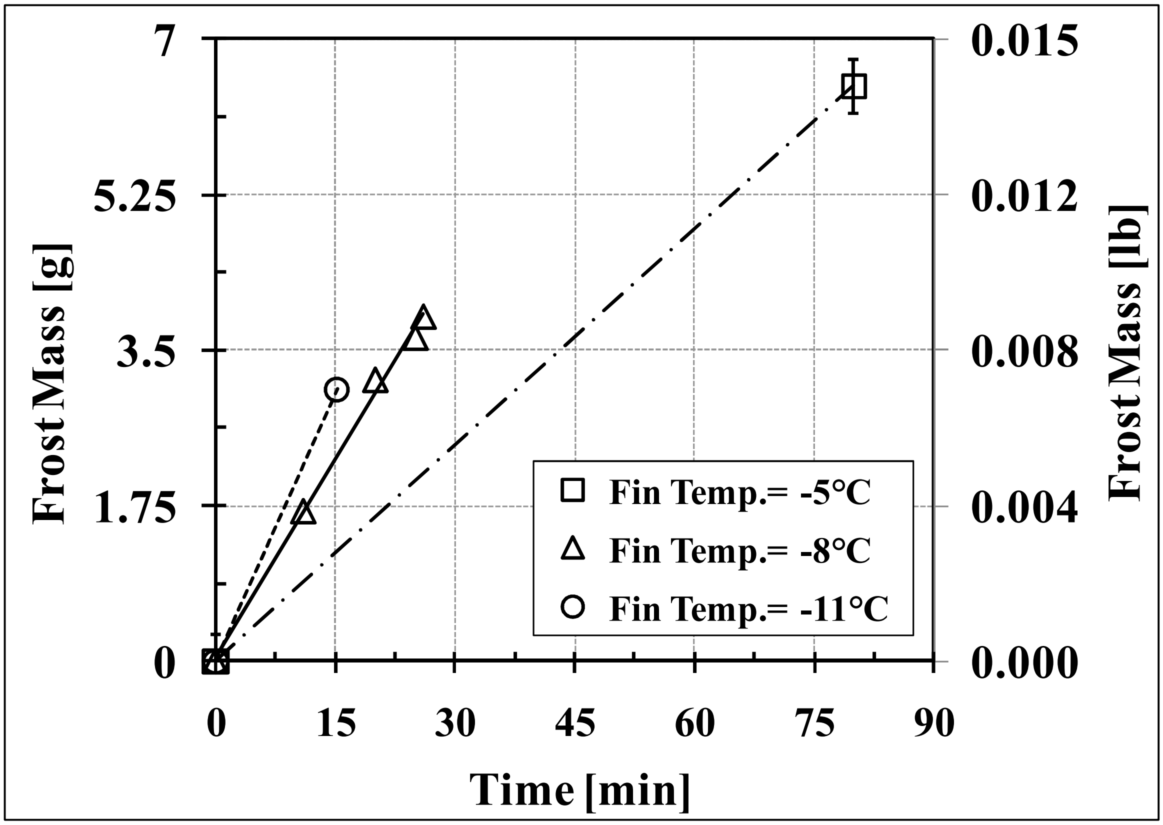

Figure 26: Frost weight on fin sample 4 for different fin temperature.

The effect of frost densification can also been observed in the measurements of the air-side pressure drop, which are shown in Figure 27. These measurements should be considered along with the frost thickness values, which measure obstruction to the air flow at the leading edge of the fins (reported previously in Figure 25). The data in Figure 27 support that the increase of the air pressure difference across the fins is caused by the increase of the frost thickness at the leading edge, which blocks the air flow. Second, by focusing on a single leading edge frost thickness, for example to 0.5, and by considering Figure 25, this thickness occurred at about 10, 20 and 73 minutes after the start of the frosting period for the three fin temperatures of -11, -8, and -5°C (12, 18, and 23°F). The corresponding pressure drops in Figure 27 are 200, 212, and 224 Pa (0.8, 0.85, and 0.9 inches H20) at the times of 10, 20 and 73 minutes for the three fin temperatures. If the frost thickness is the same for all three cases then the air flow blockage differs because of the internal porosity of the frost and due to frost-air film interface surface characteristics. At -5°C (23°F), that is, when the fin surface temperature was closer to the freezing point, the data series (c) in Figure 27 confirm that the densification of the frost occurred and it imposed a more severe barrier to the air flow. The air-side pressure drop was slightly higher than for fin temperature of -8 and -11°C (18 and 12°F) if equal frost thickness on the leading edge of the fins is considered.

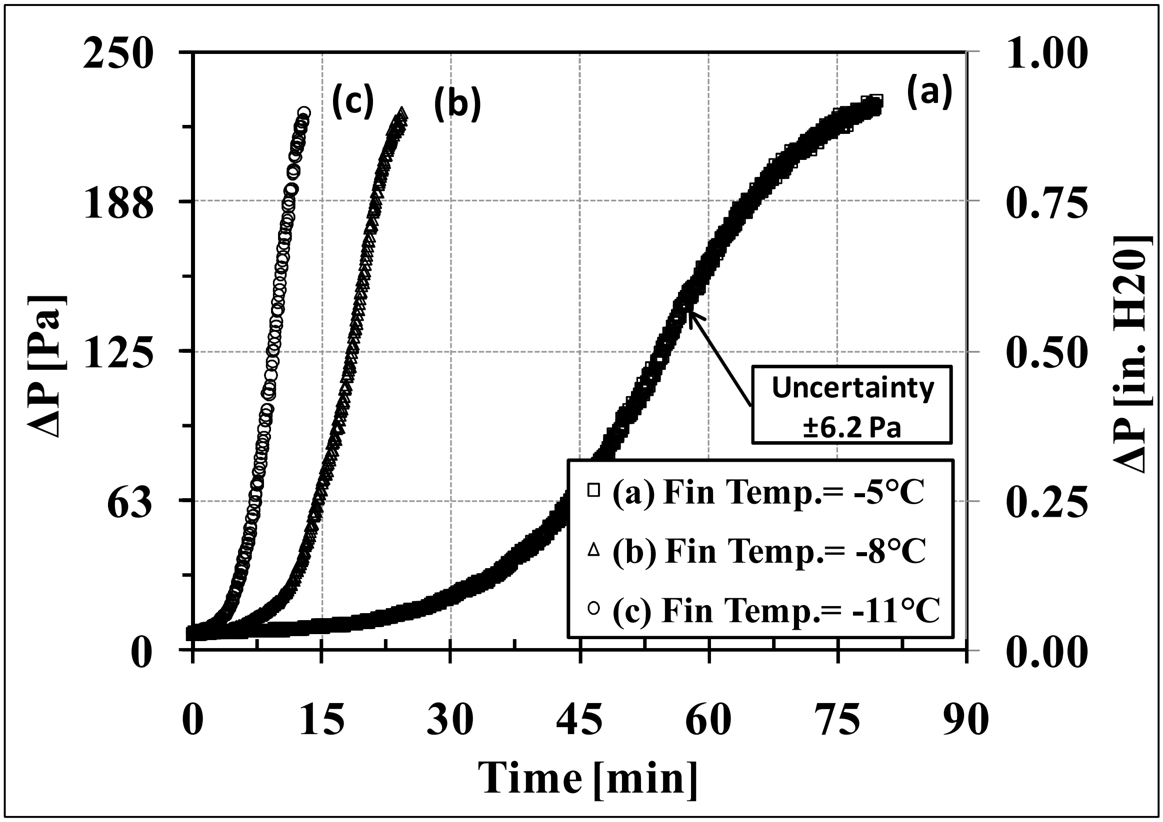

Figure 27: Pressure drop across the fin sample 4 for different fin temperature.

The fin sample capacity ratio, expressed as the ratio of the instant heat transfer rate during frosting operations to the initial heat transfer rate at the beginning of the test, is shown in Figure 28. The trends clearly indicate severe capacity degradation as frost accumulated on the fins. The initial capacity was different for the various fin temperatures and at -8°C (17.6°F) and -11°C (12°F) the heat transfer rate dropped drastically after only 20 and 11 minutes of frosting operation, respectively. The capacity decrease was due to air flow blockage, which decreased the air velocity and thus penalized the ability to exchange heat by convection at the air-frost interface boundary layers. If one takes 60% of the capacity drop as the parameter to initiate the defrost cycle, the frosting times would be 63 minutes, 20 minutes, and only 11 minutes for fin temperatures of -5°C, -8°C, and -11°C (23, 17.6, and 12°F). Experimental results for other fin densities, fin depths and fin heights provided similar results. Overall, the data showed a strong dependence of the frosting performance on the fin surface temperature.

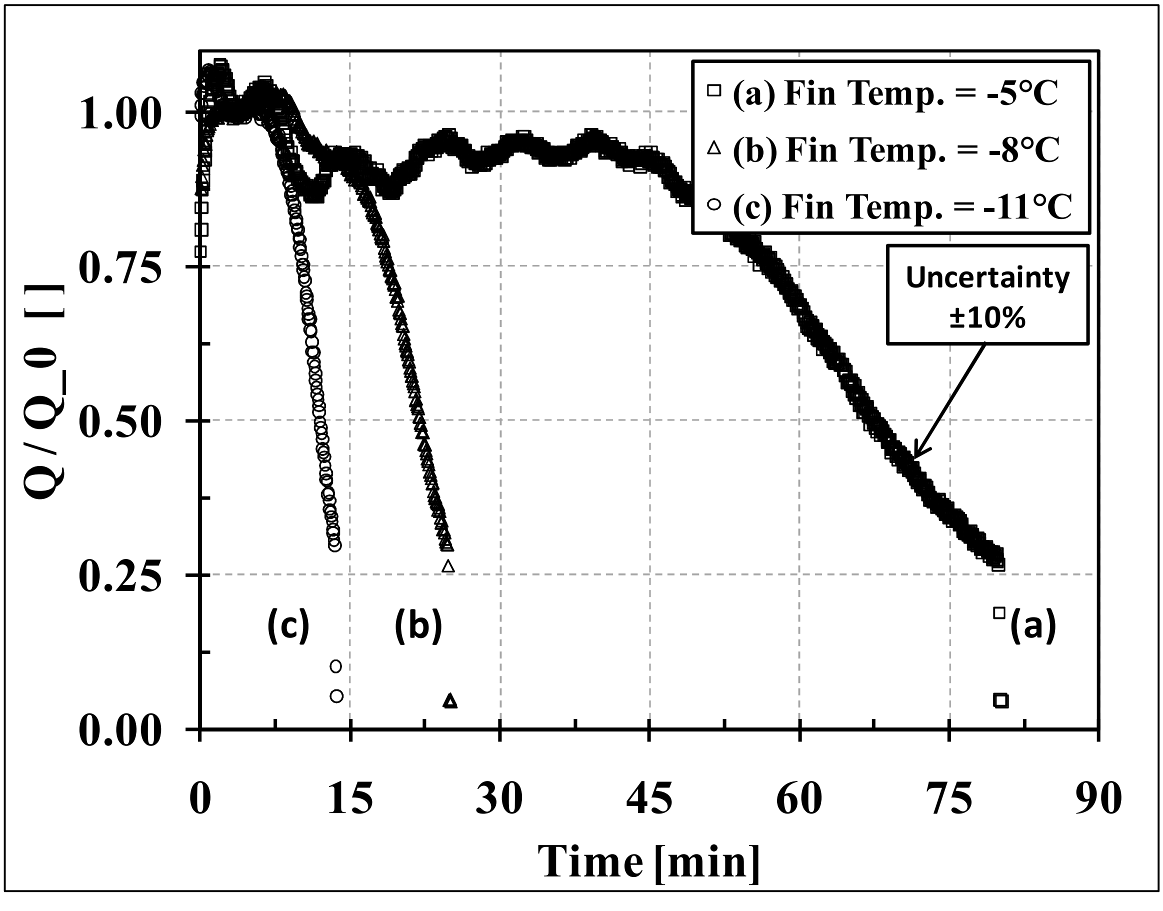

Figure 28: Capacity ratio of fin sample 4 for different fin temperature.

7.2 IMPACT OF INLET AIR HUMIDITY ON FROSTING PERFORMANCE

To estimate the effect of humidity on frost growth, tests were conducted at constant fin temperatures of -8°C (17.6°F) and at entering face velocity of 1.21 m/s (238 fpm). The relative humidity set points were 72%, 82%, and 92% with resulting absolute water vapor content of 3, 3.5 and 3.9 grams of water vapor per one kg of dry air respectively. Table 15 summarizes the results from the experiments and gives the final frost mass after termination of the tests. From the findings of Table 15 ones observes that the humidity has a peculiar effect on the frost growth. While the data at 82% and 92% R.H. (~3.5 and 3.9 absolute humidity) have similar frost mass and frosting period, a decrease of only 10% in relative humidity, that is, a decrease of the absolute humidity from 3.5 to 3 grams of water vapor per one kg of dry air, extended the frosting time to about 120 minutes. A lower ambient humidity yielded a slow frost deposition process, and the mass of the frost accumulated at the end of the cycle was almost double that the one accumulated from tests at R.H. of 82% and 92%. Additionally, it is observed that the initial capacities (Q_0) for different ambient humidity conditions are identical which suggest the reduction in entering air humidity can significantly extend the frosting period without penalizing the capacity.

Table 15: Frosting time and frost mass at different humidity ratio

Air relative humidity (%)	Frosting Time	Frost weight		Q_0	
		gram	lbm	Watt	Btu/hr
72%	120	7.07	0.0156	25.90	88.38
82%	24.8	3.88	0.0085	26.94	91.94
92%	20.4	3.46	0.0076	26.79	91.42

7.3 IMPACT OF AIR FACE VELOCITY ON FROSTING PERFORMANCE

For the velocity factor, tests were conducted at a constant fin temperature of -8°C (17.6°F) and a constant humidity of 3.5 grams of water vapor per one kg of dry air (~82%R.H.). The initial face velocity at the inlet of the fin sample were 0.8, 1.2, and 1.6 m·s-1 (157, 236 and 315 fpm), as shown in the second series of experiments reported in Table 16. For the lower face velocity of 0.8 m·s-1 (157 fpm), the frosting time was actually slightly longer than for a face velocity of 1.2 m·s-1 (236 fpm). On the other hand if the face velocity is increased to 1.6 m·s-1 (315 fpm) the, frosting time is also increased to about 34.6 minutes. When the velocity was 1.6 m·s-1 (315 fpm) the mass of frost accumulated on the fins was significantly higher, but the thickness on the front leading edge was similar to thicknesses for velocities of 1.2 and 0.8 m·s-1 (236 and 157 fpm). This finding suggests that at 1.6 m·s-1 (315 fpm) the water vapor was carried further into the coil before reaching saturation at the frost air film interface. As a consequence, the rate of frost growth at the leading edge of the fin was reduced but a larger amount of the frost accumulated inside the fin when compared to the case at face velocity of 1.2 m·s-1 (236 fpm).

Table 16: Frosting time and frost mass at different velocity

Air face velocity	Frosting Time	Frost weight		Q_0	
		gram	lbm	Watt	Btu/hr
0.8	29.2	3.35	0.0074	17.54	59.84
1.2	24.8	3.88	0.0085	26.94	91.94
1.6	34.6	5.31	0.0117	30.75	104.92

7.4 EFFECT OF GEOMETRY ON THE FROSTING PERFORMANCE

For the different samples that were tested in the experimental apparatus, the frosting time was measured from the onset of frosting to the time when the fin sample was completely blocked with frost. An alternative definition of frosting time could be derived from the ratio of the heat transfer capacity during frosting time to the initial heat transfer capacity of the fin sample, namely Q/Q0 as shown in Figure 31 where the samples are defined in Table 1. The capacity ratio Q/Q0 provides the degradation of heat transfer due to frost growth on the fin surfaces. In Figure 31 the frosting time was calculated at a Q/Q_0 ratio of 0.6, that is, when the capacity of the fin sample decreased by 40% with respect to its initial capacity. The results of the frosting test for different fin geometries are summarized in Table 19. This table also includes the inlet air condition and fin temperature for each of the samples.

7.4.1 Effect of fin density on the frosting performance

Samples 1 through 3 have identical geometries aside from the fin density. Figure 29 and Table 17 shows that samples 1, 2, and 3 have frosting time of 54.3 minutes, 19.3 minutes, and 12.8 minutes at the baseline temperature of Tfin=-8°C (~18°F). Unfortunately sample 1 was available only with corrugated flat fins, that is, without any louvers. Even though its frosting time was higher than the ones for samples 2 and 3, the actual initial capacity of sample 1 was considerable lower. For samples 2 and 3, which have very similar geometries and similar louvered fins, an increase of fin density from 13.6 to 20.3 fin per inch (FPI) reduced the frosting period from 19.3 minutes to about 12.8 minutes, that is more than a 34% in reduction of the frosting time when T_{fin}=-8°C (~17.6°F). The reduction of frosting time was dependent on the fin temperature, and the curves for sample 2 and sample 3 in Figure 29 diverge as the fin temperature approaches the freezing point.

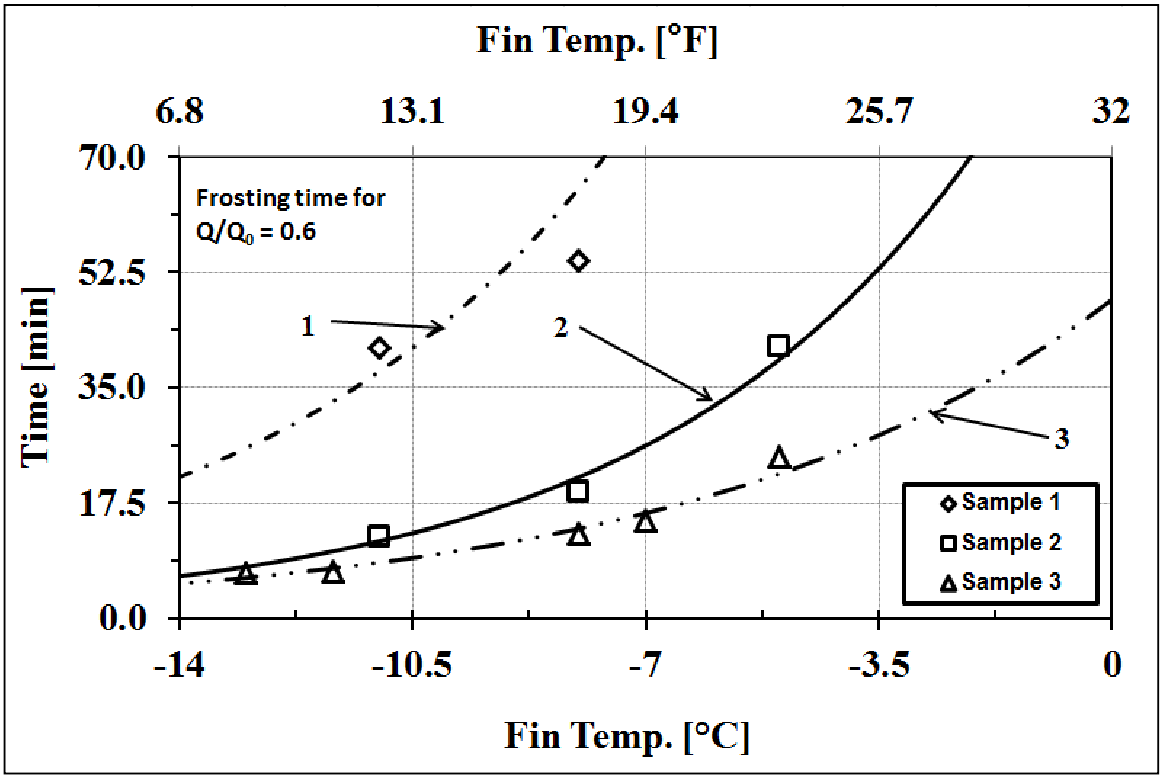

Figure 29: Frosting time for fin samples with different fin density

Table 17: Result of frosting test for fin samples with different fin density

FIN SAMPLE	FIN TEMPERATURE [°C] (°F)	FIN DENSITY [fins per inch, FPI]	FIN HEIGHT [mm] (inch)	FIN DEPTH [mm] (inch)	FROSTING TIME @ $Q/Q_0 = 0.6$ (Minutes)	Q_0 [Watt] (Btu/hr)
1	-5 (23.0) -8 (17.6) -11 (12.2)	10.4 (flat fin)	8 (0.315)	27 (1.063)	124.8 54.3 41.0	11.56 (39.44) 17.07 (58.24) 23.00 (78.48)
2	-5 (23.0) -8 (17.6) -11 (12.2)	13.6	8 (0.315)	27 (1.063)	41.4 19.3 12.4	18.01 (61.44) 24.30 (82.92) 28.83 (98.38)
3	-5 (23.0) -7 (19.4) -8 (17.6) -12 (10.4) -13 (8.6)	20.3	8 (0.315)	26 (1.063)	24.4 14.8 12.8 7.2 6.8	17.97 (61.32) 24.47 (83.50) 26.20 (89.39) 31.27 (106.68) 34.48 (117.66)

7.4.2 Effect of fin height on the frosting performance

Samples 4 and 5 both have the same fin density, very similar fin depths of 25 and 27 mm, but different fin heights of 10 and 13 mm, respectively. Sample 5 had approximately 20% to 30% higher capacity compare to sample 4. This suggests that as the fin height and fin depth increased, the capacity also increases. At the higher fin temperature of -5°C (23°F), sample 4 has higher frosting time when compared to sample 5, i.e., sample 5 has a frosting time of 37.8 minutes and sample 4 had 63.4 minutes, which is more than 68% extension. At fin temperature of about -14 to -7°C (6.8 to 19.4°F) the frosting time of both samples is quite similar. This observation suggests that the increasing the fin depth and fin height extends the heat transfer area. This would increase the heat transfer rate but decrease the frosting time. This phenomenon was measurable only if the fin temperature was above -7°C (19.4°F), that is, closer to the freezing point.

Another comparison can be made between samples 3 and 5 to see the effect of fin density and fin height. Sample 3 and 5 both have similar fin depth, but they have different fin density and fin height. The fin density of samples 3 and 5 was 20.3 FPI and 19.6 FPI, and fin height was 8 mm and 13 mm, respectively. At a fin temperature of about -5°C (23°F), samples 3 and 5 have frosting times of 24.4 minutes and 37.8 minutes. An increase of fin height from 8 mm to 13 mm would increase the heat transfer area. If similar fin height is maintained, a reduction of FPI from 20.3 to 19.6 would decrease the heat transfer area and at the same time, augment the space for frost accumulation before flow blockage. Between the extension of fin height and the reduction of FPI, fin density seems to have a major effect on the frosting time since sample (with at 19.6 FPI) had longer frosting time than sample 3 (with 20.3 FPI). At the same time sample 3 had approximately 24% lower initial capacity than sample 5. This indicates that higher fin heights with lower FPI are better for frosting operating conditions.

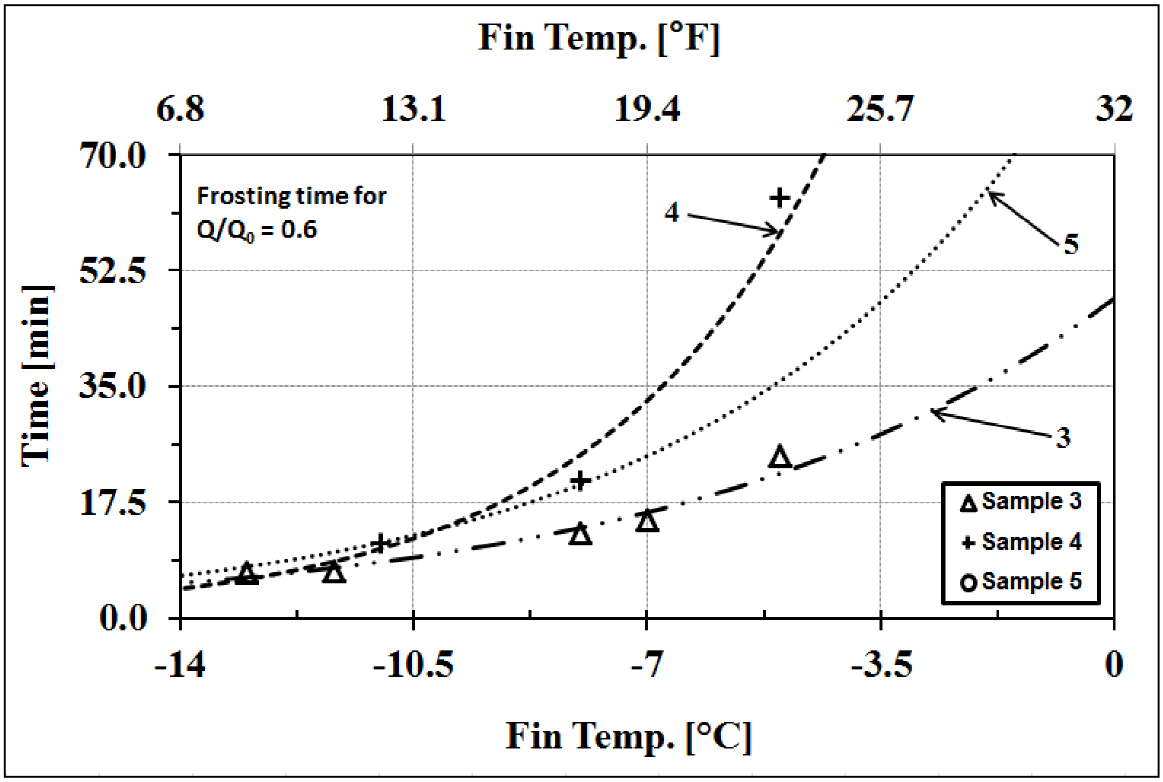

Figure 30: Frosting time for fin samples with different fin height

Table 18: Result of frosting test for fin samples with different fin height

FIN SAMPLE	FIN TEMPERATURE [°C] (°F)	FIN DENSITY [fins per inch, FPI]	FIN HEIGHT [mm] (inch)	FIN DEPTH [mm] (inch)	FROSTING TIME @ $Q/Q_0 = 0.6$	Q_0 [Watt] (Btu/hr)
3	-5 (23.0)	20.3	8 (0.315)	26 (1.063)	24.4	17.97 (61.32)
	-7 (19.4)				14.8	24.47 (83.50)
	-8 (17.6)				12.8	26.20 (89.39)
	-12 (10.4)				7.2	31.27 (106.68)
	-13 (8.6)				6.8	34.48 (117.66)
4	-5 (23.0)	19.4	10 (0.394)	25 (0.984)	63.4	17.54 (59.84)
	-8 (17.6)				20.8	26.94 (91.94)
	-11 (12.2)				11.4	30.75 (104.92)
5	-5 (23.0)	19.6	13 (0.512)	27 (1.063)	37.8	23.53 (80.29)
	-8 (17.6)				18.2	32.93 (112.37)
	-11 (12.2)				12.0	40.18 (137.10)

7.4.3 Effect of fin depth on the frosting performance

Samples 6 and 7 have the same fin height of 8 mm, similar fin density of 18.5 FPI and 17.5 FPI, but different fin depths of 30 and 19 mm, respectively. At higher fin temperature of -5°C (23°F), sample 6 had approximately 15% higher capacity compare to sample 7. This suggests that as the fin depth and fin density increased, the capacity also increases. This increase in capacity on sample 6 penalized the frosting time. At -5°C (23°F) fin temperature, sample 6 has frosting time of 31.5 minutes compare to sample 7 has 37.4 minutes, which is more than 18% reduction. On the other hand, at lower fin temperature (-8 and -11°C), the capacity difference between samples 6 and 7 become significant. Sample 6 had approximately 40 to 45% higher capacity compared to sample 7, while the frosting time reduced by 24% and 7% at -8 and -11°C respectively.

Another comparison was made between samples 3 and 6 to see the effect of fin density and fin depth. Samples 3 and 6 both have similar fin height, but different fin depth and fin density. The fin height of samples 3 and 6 was 26 and 30 mm, and fin density was 19.4 and 18.5 FPI respectively. At higher fin temperature (-5°C), the frosting time of fin samples 3 and 6 was 24.4 and 31.5, which indicate that the frosting time experienced reduction of 22%. Meanwhile, the capacity of sample 6 was higher by 8% when compared to sample 3. At lower fin temperature (-8 and -11°C), the capacity difference between samples 3 and 7 become significant. Sample 3 had approximately 17 and 25% higher capacity compared to sample 3, while the frosting time did not show any significant difference at -8 and -11°C respectively. This phenomenon suggested that increasing fin height results in higher the overall heat transfer rate and the slight increase in fin density augment the frosting time. The capacity improvement became more sensitive at a lower fin temperature, while the frosting time is more sensitive at a higher fin temperature.

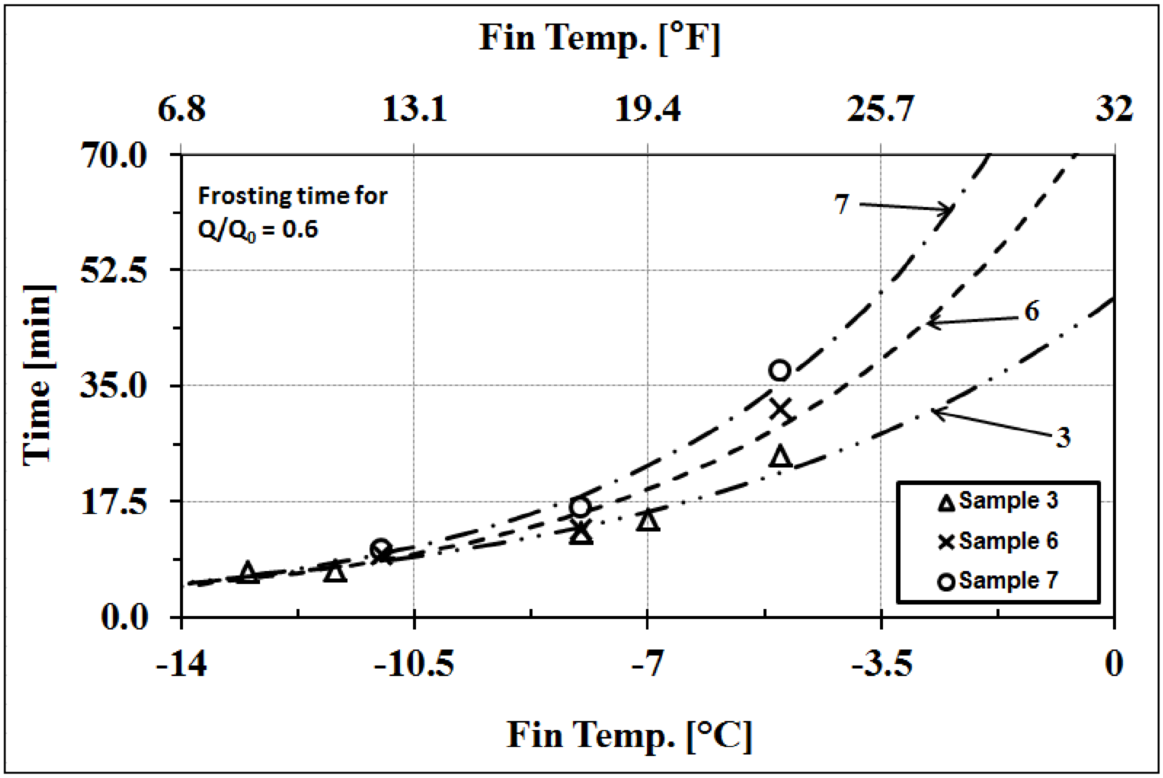

Figure 31: Frosting time for fin samples with different fin depth

Table 19: Summary of frosting test for different fin deptha

FIN SAMPLE	FIN TEMPERATURE [°C] (°F)	FIN DENSITY [fins per inch, FPI]	FIN HEIGHT [mm] (inch)	FIN DEPTH [mm] (inch)	FROSTING TIME @ $Q/Q_0 = 0.6$	Q_0 [Watt] (Btu/hr)
3	-5 (23.0)	20.3	8 (0.315)	26 (1.063)	24.4	17.97 (61.32)
	-7 (19.4)				14.8	24.47 (83.50)
	-8 (17.6)				12.8	26.20 (89.39)
	-12 (10.4)				7.2	31.27 (106.68)
	-13 (8.6)				6.8	34.48 (117.66)
6	-5 (23.0)	18.5	8 (0.315)	30 (1.181)	31.5	19.46 (66.40)
	-8 (17.6)				13.4	30.62 (104.49)
	-11 (12.2)				9.5	39.00 (133.07)
7	-5 (23.0)	17.5	8 (0.315)	19 (0.748)	37.4	16.87 (57.57)
	-8 (17.6)				16.6	21.03 (71.77)
	-11 (12.2)				10.1	27.56 (94.02)

The frosting time is more sensitive to the fin temperature of the leading edge when the wall temperature was -5°C (23°F) because the fin leading edge temperature might be closer to the freezing point. In other words small deviations of the fin base surface temperature from the nominal value of -5°C (23°F) might have resulted in substantial variations of the actual fins edge temperature just below the freezing point of the water vapor. This theory seems to be confirmed by the fact that at the lower fin temperature of -11°C (12°F) the frosting times of all seven samples were close to each other For similar fin-base temperature the actual fin temperature along the leading edge of the fins is slightly higher if the fin height increased.

7.3 CONCLUSION

This section presents the experimental part of frost growth on flat and louvered folded fins adopted in microchannel heat exchangers. From the experiments, it was observed that the frost mass grew linearly with respect to time. The frost thickness accumulated on the leading edge of the fin sample was determined to be the main cause of the air flow blockage across the fins. The air flow blockage led to significant reduction in the heat transfer rate of the fin sample. The growth rate of frost thickness on the leading edge of the fins was also strongly dependent on the fin surface temperature.

Parameters such as fin temperature, air humidity, and air face velocity were tested in the experiments to observe the effect on the performance of the microchannel coils. Fin temperature and air face velocity were observed to have significant impact on frost growth rate. At the higher fin temperature, which was about -5°C (23°F), the frosting period was drastically improved compared to the baseline case at the surface temperature of -8°C (17.6°F). This improvement was also observed at the lower humidity condition (72% of relative humidity) when compared to the baseline case of 82% of relative humidity.

Results of frosting time for different fin geometries were also presented in this section. Folded flat fins seemed to have higher frosting time due to lower heat transfer capacity when compared to folded louvered fins at the same microchannel tube wall surface temperature. For similar fin density, a reduction of the fin depth and fin height resulted to lower heat transfer capacity but higher frosting time. However, if the fin density increased and the fin height decreased then both frosting time and capacity decreased. This was due to the fact that the heat transfer area was reduced even if the fin density was augmented. For similar fin height, if the fin depth increased and the fin density decreased, then the capacity increased and the frosting time decreased. The improvement in capacity became significant at lower fin temperature (-8 and -11°C) while the frosting time became less significant at these condition. This suggested that the improvement on microchannel capacity can be done by increasing the fin depth especially if the microchannel is operating at lower fin surface temperature. The effect of fin density was predominant in determining the air flow blockage at about -5°C (23°F) for the microchannel tube surface temperature. When the microchannel tube surface temperature decreased below -10°C (14°F), the effect of fin geometries (fin height, fin depth, and fin density) on the frosting time became less significant.

CHAPTER VII

CONCLUSIONS

This thesis summarizes the experimental work conducted at Oklahoma State University (OSU) for measuring the frost performance of microchannel heat exchanger in heat pump applications. A new experimental apparatus was designed, constructed, and calibrated to simulate the operating condition of outdoor microchannel coils utilized in heating application during winter conditions in OSU laboratory. Along with the new experimental apparatus, microchannel fin samples were also cut out from commercially available coils in order to fit into the developed test apparatus. The sizes of the fin sample guaranteed uniform condition across the fin sample and enable the measurements of surface wall fin temperature, which was a major innovation of the test apparatus. The design of experimental test apparatus is presented in the thesis. The instrumentation is used to measure frost parameters such as; frost mass and frost thickness, heat transfer rate, and air-side pressure drop during the actual frosting operating conditions. Experimental validation was conducted to examine if the test apparatus and instrumentation worked properly. It was confirmed that the test apparatus had the capability to perform the frost experiments and the instrumentation also functioned properly.

A new experimental methodology is presented to measure frost thickness, frost mass, and fin surface temperature during actual frosting operating conditions. Frost mass was measured and the data in this work suggested that the frost mass grew linearly with time, that is, water vapor did not experience any measurable time delay before it started to frost and to accumulate on the fins surface. Frost thickness on the leading edge of the fins was observed to be non-linear with time and the growth rate was strongly dependent on the fin surface temperature. The frost thickness on the front leading edge of the fins was responsible for the air flow blockage across the fins and generated severe air pressure drops. The heat transfer capacity was also seriously penalized by the flow blockage.

Several experiments were conducted to quantify the impact of fin temperature, air humidity, and air face entering velocity on the frost growth rate on the louvered fins. Fin temperature and air humidity were found to have a predominant effect on frost growth rate. When the fin surface temperature approached near freezing point of about -5°C (23°F), the frosting cycle time was noticeably extended with respect to the baseline case, for which the surface temperature was about -8°C (17.6°F). An increase in the frosting time was also observed when the absolute humidity was varied from 3.5 to 3 gram of water vapor per kg of dry air and with similar air dry bulb temperature of 1.7°C (35°F).

The findings from my thesis suggested that the fin density is one of the main factors affecting the frosting period while fin depth and fin height had a second order of magnitude impact on the frosting time. Fin samples with similar fin density had comparable frosting time and the effect of both fin depth and fin height were measurable only when the fin temperature was about -5°C (23°F). Further tests on different fin geometries are needed and a larger set of fin geometries and fin surface coatings are recommended in future expansions of my thesis in order to provide further understanding of the frosting process on louvered folded fins of microchannel heat exchangers.

From these frosting experiments, I discovered that the main factor that prevents the heat transfer process during the frosting condition is the frost thickness that accumulates at the leading edge of the fin. The parameters that improve the frosting performance of microchannel coil are reduction of ambient humidity, reduction of fin density, and increase of fin depth. The reduction in the humidity of the air stream entering to the coil can provide significant extension of the frosting time, which is the actual heating time of the heat pump unit in operation during winter season. Reduction of the coils fin density provides considerable extension in frosting time and slight reduction in heat transfer capacity of the coil. The increase in fin depth enhances the heat transfer capacity of the coil especially at the lower fin temperature without significantly affecting the frosting time. This could improve the overall energy efficiency performance of the heat pump system during winter operating conditions.

REFERENCES

AHRI (2005). AHRI Standard 210/240-2005, Unitary air conditioning and air-source heat pump equipment. H. a. R. I. Air-Conditioning. Arlington, VA Air-Conditioning, Heating and Refrigeration Institute.

ASHRAE (2001). ANSI/ASHRAE 41.2-2001, Standard methods for laboratory airflow measurements. ASHRAE, ASHRAE.

Cai S. (2009) Design of an Experimental Facility for Measurement of Frost Growth on Heat Exchangers. Master Thesis Mechanical and Aerospace Engineering Department, Oklahoma State University, OK, USA.

Garimella, S. (2003). "Innovations in energy efficient and environmentally friendly space-conditioning systems." *Energy* **28**(15): 1593-1614.

Guo, X., C. Wang, W. Wang and C. Chen (2006). "Numerical simulation and experimental verification on dynamic performance of air source heat pump under frosting conditions." *Hsi-An Chiao Tung Ta Hsueh/Journal of Xi'an Jiaotong University* **40**(5): 544-548.

Hayashi, Y., A. Aoki, S. Adachi and K. Hori (1977). "Study of Frost Properties Correlating with Frost Formation Types." *Journal of heat transfer* **99**(2): 239-245.

Jacobi, A. M., Y. Park, Y. Zhong, G. Michna and Y. Xia (2005). High performance heat exchangers for air-conditioning and refrigeration applications (non-circular tubes). *Final Report*. ARI. Arlington, VA, ARTI-21CR/605-20021-01, Final Report for the Air-Conditioning and Refrigeration Technology Institute**:** 288.

Joardar, A., Gu, Z., and Jacobi, A., M. (2006). Off-cycle condensate drainage behavior of compact heat exchangers: assessment and enhancement. *International Refrigeration and Air Conditioning Conference at Purdue*, Purdue University, West Lafayette, IN.

Kim, J.-H. and E. A. Groll (2003). Performance comparisons of a unitary split system using microchannel and fin-tube outdoor coils. *ASHRAE Transactions* 109(2):219-229.

Kim, M.-H. and C. W. Bullard (2002a). "Air-side performance of brazed aluminum heat exchangers under dehumidifying conditions." *International Journal of Refrigeration* **25**(7): 924-934.

Kim, M.-H. and C. W. Bullard (2002b). "Performance evaluation of a window room air conditioner with microchannel condensers." *Journal of Energy Resources Technology, Transactions of the ASME* **124**(1): 47-55.

Mao, Y., R. W. Besant and J. Falk (1993). "Measurements and Correlations of Frost Properties with Laminar Airflow at Room Temperature over a Flat Plate." *ASHRAE Transactions* **99**(1): 739-745.

Mao, Y., R. W. Besant and K. S. Rezkallah (1992). "Measurement and Correlations of Frost Properties with Airflow over a Flat Plate." *ASHRAE Transactions* **98**(2): 65-78.

Moallem, E., Cremaschi, L., Fisher, D., E., (2010a). Experimental Investigation of Frost Growth on Microchannel Heat Exchangers. *13th International Refrigeration and Air Conditioning Conference at Purdue*, West Lafayette, IN (USA), Purdue Univ, paper no. 2416.

Moallem, E., Padhmanabhan, S., Fisher, D., E., Cremaschi, L. (2010b). Experimental study of onset and growth of frost on outdoor coils of air-source heat pump systems. *ASME-ATI-UTI Conference on Thermal and Environmental Issues in Energy Systems*, Sorrento, Italy, ASME.Na, B. and R. L. Webb (2004). "New Model for Frost Growth Rate." *International Journal of Heat and Mass Transfer* **47**: 925-936.

Ohkubo, H. (2006). "Advance of 'study on frosting phenomena'." *Refrigeration* **81**(942): 9.

Östin, R. and S. Andersson (1991). "Frost growth parameters in a forced air stream." *International Journal of Heat and Mass Transfer* **34**(4-5): 1009-1017.

Padhmanabhan, S., D. Fisher, E., , L. Cremaschi and J. Knight (2008). Comparison of frost and defrost performance between microchannel coil and fin-and-tube coil for heat pump systems. *12th Int. Refrigeration and Air Conditioning Conference at Purdue*, West Lafayette, IN (USA), Purdue Univ, paper no. R2202.

Peng, X., Z. He, Z. Xing and P. Shu (2003). "Operating characteristics of an air-source heat pump under frosting/defrosting conditions." *Proceedings of the Institution of Mechanical Engineers, Part A: Journal of Power and Energy* **217**(6): 623-630.

Sahin, A. Z. (1994). "An experimental study on the initiation and growth of frost foramation on a horizontal plate." *Experimental Heat Transfer: An International Journal* **7**(2): 101-119.

Shin, J., A. V. Tikhonov and C. Kim (2003). "Experimental Study on Frost Structure on Surfaces With Different Hydrophilicity: Density and Thermal Conductivity." *Journal of Heat Transfer* **125**(1): 84-94.

Thomas, L., H. Chen and R. Besant, W. (1999). "Measurement of Frost Characteristics on Heat Exchanger Fins." *ASHRAE Transactions*: 283-293.

Xia, Y., P. S. Hrnjak and A. M. Jacobi (2005). Air-side thermal-hydraulic performance of louvered-fin, flat-tube heat exchangers with sequential frost-growth cycles. *ASHRAE Transactions* **111**(1):487-495.

Xia, Y., Y. Zhong, P. S. Hrnjak and A. M. Jacobi (2006). "Frost, defrost, and refrost and its impact on the air-side thermal-hydraulic performance of louvered-fin, flat-tube heat exchangers." *International Journal of Refrigeration* **29**(7): 1066-1079.

Yonko, J. D. and C. F. Sepsy (1967). "An Investigation of the Thermal Conductivity of Frost While Forming on a Flat Horizontal Plate." *ASHRAE Transactions* **73, Part 1**(Paper No 2043): 1.1-1.11.

Zhang P. and P.S. Hrnjak (2010a). "Effect of some geometric parameters on performance of PF^2 heat exchangers in periodic frosting." *International Journal of Refrigeration* **33**: 334-346.

Zhang P. and P.S. Hrnjak (2010b). "Air-side performance of a parallel-flow parallel-fin (PF^2) heat exchanger in sequential frosting." *International Journal of Refrigeration* **33**: 1118-1128.

Zhong, Y., Jacobi, A., M., and Georgiadis, J., G.. (2006). Condensation and wetting behavior on surfaces with micro-structure: super-hydrophobic and super-hydrophilic. *International Refrigeration and Air Conditioning Conference at Purdue*, Purdue University, West Lafayette, IN, paper no. R100.

APPPENDICES

APPENDIX A: UNCERTAINTY OF THERMOCOUPLE

The uncertainty analysis on temperature reading that use more than one thermocouples are not straight forward due to the non-uniform temperature distribution. The method that used to analyz the uncertainty is the approach provided by Johson et al. 1998. The technique is to combine the uneven temperature distribution and the uncertainty on termocouple reading as seen in equation belows. The overall fin temperature will be the average of the eight thermocouples and the uncertainty will be B_T ($T_{fin} = T_{avg} \pm B_T$).

$$B_{T,distribution} = \frac{T_{max} - T_{min}}{n} = \frac{(T_{max,reading} + dT) - (T_{min,reading} - dT)}{n}$$

$$B_{T,uniform} = \frac{\Delta T_{uniform}}{n} = \frac{2 \cdot dT}{n}$$

$$B_T = \sqrt{{B_{T,distribution}}^2 + {B_{T,uniform}}^2}$$

Where:

- $B_{T,distribution}$ = Bias uncertainty resulting from uneven temperature distribution (°C)
- $T_{max,reading}$ = Maximum thermocouple reading out of eight thermocouples (°C)
- $T_{min,\ reading}$ = Minimum thermocouple reading out of eight thermocouples (°C)
- dT = Uncertainty of thermocouple measurement (°C)
- n = The total number of measuring points in the grid
- $B_{T,uniform}$ = Bias uncertainty resulting from even temperature distribution (°C)
- BT = Overall uncertainty of the fin temperature (°C)

APPENDIX B: HUMIDITY RATIO CALCULATION

EES code that used to calculate for humidity ratio:

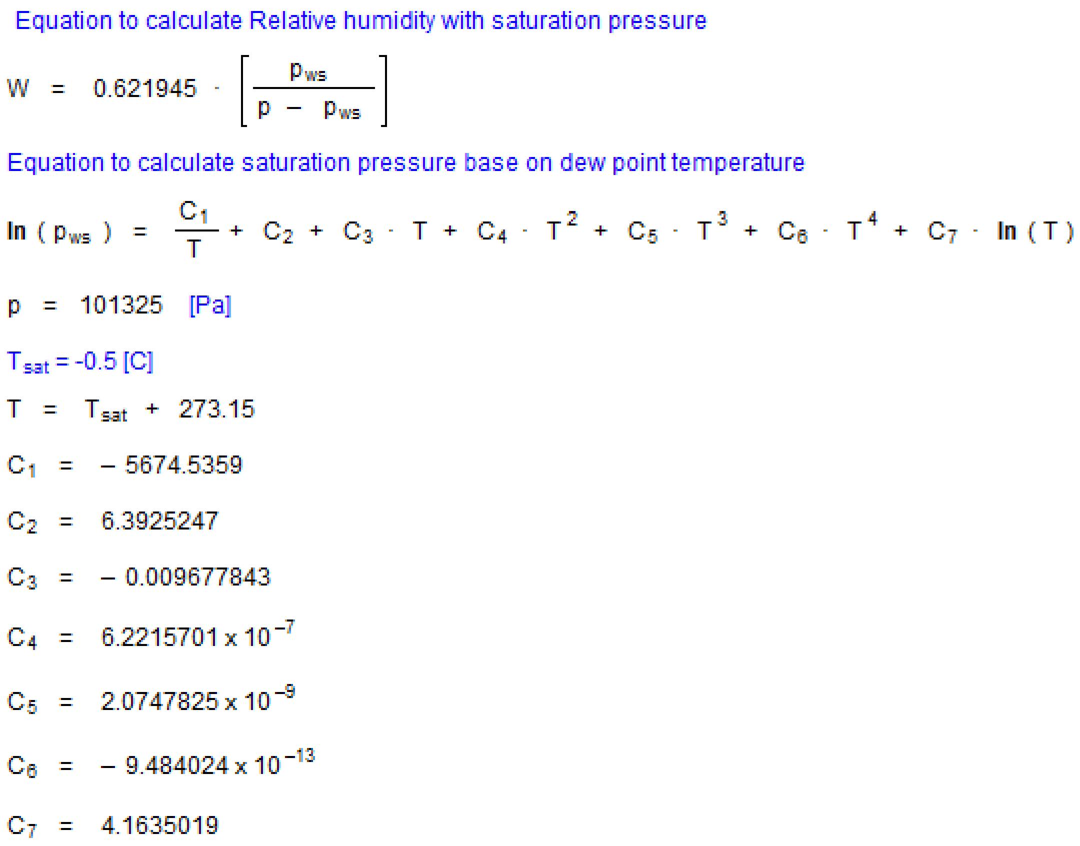

Equation to calculate Relative humidity with saturation pressure

$$W = 0.621945 \cdot \left[\frac{p_{ws}}{p - p_{ws}} \right]$$

Equation to calculate saturation pressure base on dew point temperature

$$\ln (p_{ws}) = \frac{C_1}{T} + C_2 + C_3 \cdot T + C_4 \cdot T^2 + C_5 \cdot T^3 + C_6 \cdot T^4 + C_7 \cdot \ln (T)$$

$p = 101325$ [Pa]

$T_{sat} = -0.5$ [C]

$T = T_{sat} + 273.15$

$C_1 = -5674.5359$

$C_2 = 6.3925247$

$C_3 = -0.009677843$

$C_4 = 6.2215701 \times 10^{-7}$

$C_5 = 2.0747825 \times 10^{-9}$

$C_6 = -9.484024 \times 10^{-13}$

$C_7 = 4.1635019$

APPENDIX C: MASS FLOW RATE CALCULATION

EES code that used to calculate for mass flow rate:

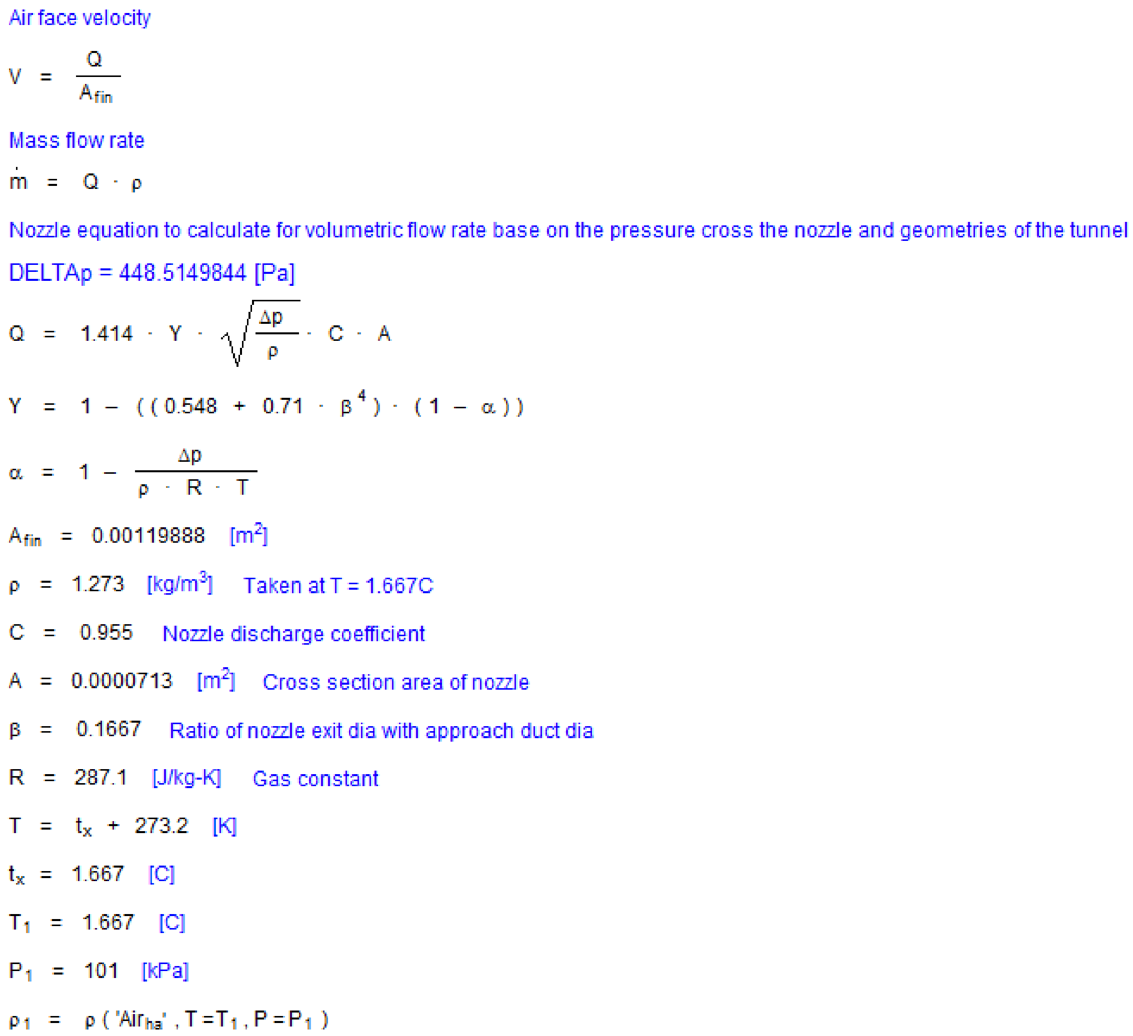

Air face velocity

$$V = \frac{Q}{A_{fin}}$$

Mass flow rate

$$\dot{m} = Q \cdot \rho$$

Nozzle equation to calculate for volumetric flow rate base on the pressure cross the nozzle and geometries of the tunnel

DELTAp = 448.5149844 [Pa]

$$Q = 1.414 \cdot Y \cdot \sqrt{\frac{\Delta p}{\rho}} \cdot C \cdot A$$

$$Y = 1 - ((0.548 + 0.71 \cdot \beta^{4}) \cdot (1 - \alpha))$$

$$\alpha = 1 - \frac{\Delta p}{\rho \cdot R \cdot T}$$

$A_{fin} = 0.00119888$ [m^2]

$\rho = 1.273$ [kg/m^3] Taken at T = 1.667C

$C = 0.955$ Nozzle discharge coefficient

$A = 0.0000713$ [m^2] Cross section area of nozzle

$\beta = 0.1667$ Ratio of nozzle exit dia with approach duct dia

$R = 287.1$ [J/kg-K] Gas constant

$T = t_x + 273.2$ [K]

$t_x = 1.667$ [C]

$T_1 = 1.667$ [C]

$P_1 = 101$ [kPa]

$\rho_1 = \rho\,(\text{'Air}_{ha}\text{'}, T = T_1, P = P_1)$

APPENDIX D: HEAT TRANSFER RATE (ENTHALPY METHOD) CALCULATION

EES code used to calculate heat transfer rate with enthalpy method:

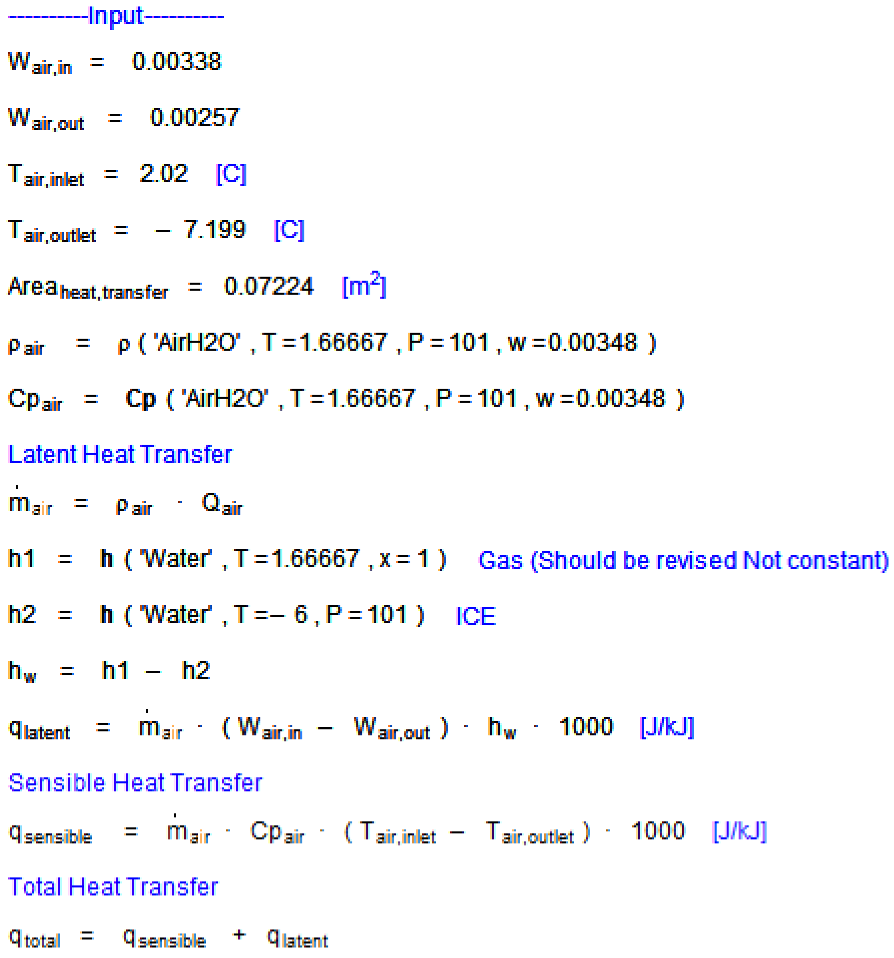

----------Input----------

$W_{air,in} = 0.00338$

$W_{air,out} = 0.00257$

$T_{air,inlet} = 2.02$ [C]

$T_{air,outlet} = -7.199$ [C]

$Area_{heat,transfer} = 0.07224$ [m^2]

$\rho_{air} = \rho$ ('AirH2O' , T = 1.66667 , P = 101 , w = 0.00348)

$Cp_{air} =$ **Cp** ('AirH2O' , T = 1.66667 , P = 101 , w = 0.00348)

Latent Heat Transfer

$\dot{m}_{air} = \rho_{air} \cdot Q_{air}$

h1 = **h** ('Water' , T = 1.66667 , x = 1) Gas (Should be revised Not constant)

h2 = **h** ('Water' , T = – 6 , P = 101) ICE

$h_w = h1 - h2$

$q_{latent} = \dot{m}_{air} \cdot (W_{air,in} - W_{air,out}) \cdot h_w \cdot 1000$ [J/kJ]

Sensible Heat Transfer

$q_{sensible} = \dot{m}_{air} \cdot Cp_{air} \cdot (T_{air,inlet} - T_{air,outlet}) \cdot 1000$ [J/kJ]

Total Heat Transfer

$q_{total} = q_{sensible} + q_{latent}$

APPENDIX E: HEAT TRANSFER RATE (CONDUCTION METHOD)

EES code used to calculate heat transfer rate with conduction method:

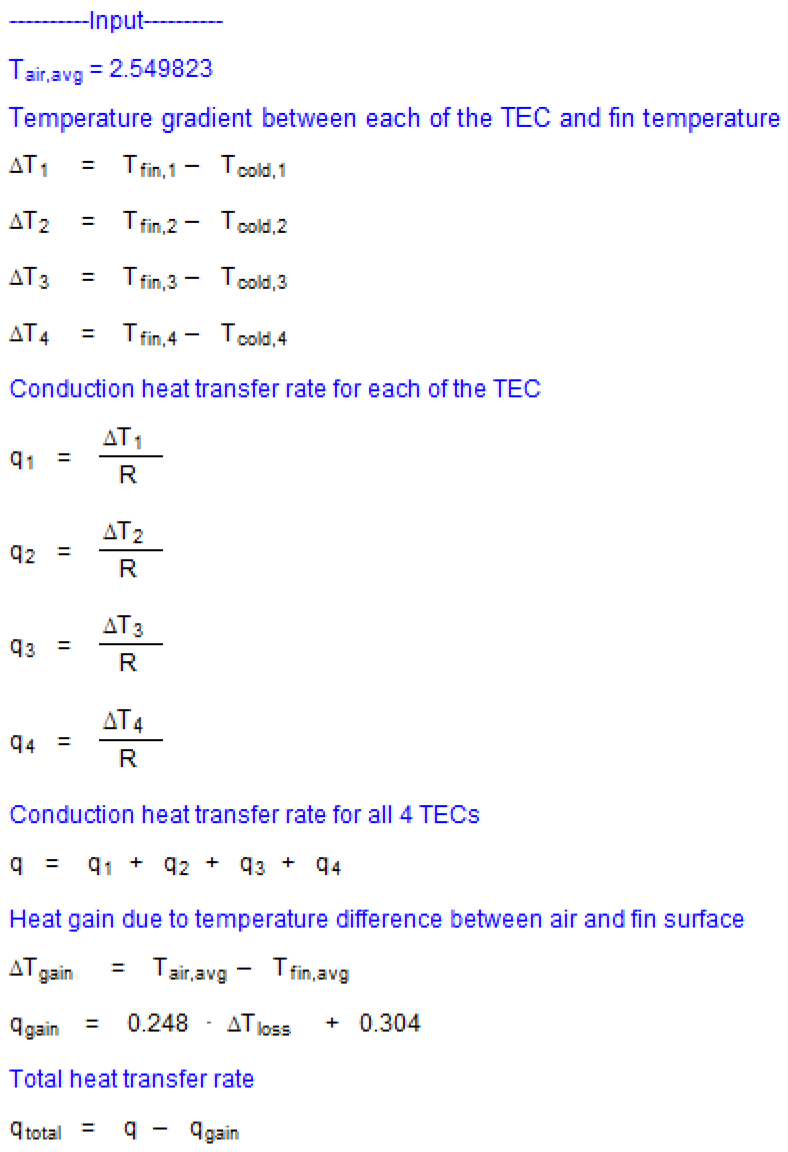

----------Input----------

$T_{air,avg} = 2.549823$

Temperature gradient between each of the TEC and fin temperature

$\Delta T_1 = T_{fin,1} - T_{cold,1}$

$\Delta T_2 = T_{fin,2} - T_{cold,2}$

$\Delta T_3 = T_{fin,3} - T_{cold,3}$

$\Delta T_4 = T_{fin,4} - T_{cold,4}$

Conduction heat transfer rate for each of the TEC

$$q_1 = \frac{\Delta T_1}{R}$$

$$q_2 = \frac{\Delta T_2}{R}$$

$$q_3 = \frac{\Delta T_3}{R}$$

$$q_4 = \frac{\Delta T_4}{R}$$

Conduction heat transfer rate for all 4 TECs

$q = q_1 + q_2 + q_3 + q_4$

Heat gain due to temperature difference between air and fin surface

$\Delta T_{gain} = T_{air,avg} - T_{fin,avg}$

$q_{gain} = 0.248 \cdot \Delta T_{loss} + 0.304$

Total heat transfer rate

$q_{total} = q - q_{gain}$

APPENDIX F: UNCERTAINTY OF MASS FLOW RATE

The mass flow rate in the experiment is calculated from the volumetric flow rate and frontal area of the fin sample as seen in Equation (11). The air volumetric flow rate is estimated from static pressure difference as described in the previous section. Therefore, the main parameter that affects the uncertainty is the accuracy of pressure transducer is ±40 Pa (0.16 in.H2O). The uncertainty analysis was done by using the experimental data from fin sample 2 with -5°C fin temperature. The uncertainty was calculated in EES program. The result of the uncertainty analysis can be seen in table below. At the beginning of the test, the uncertainty of mass flow rate was estimated to be ±4.5% of the reading. As the flow rate decreased the uncertainty increased and reached ±63% at the end of the test. The uncertainty of the mass flow rate increased significantly towards the end of the frosting test because the pressure readings across the nozzle became considerably smaller than the full scale range of the pressure transducer. The uncertainty of the pressure transducer had a significant impact on the flow rate measurements if the air flow velocity during the frosting period reduced to more than 50% of its initial value at the beginning of the test.

Δp				mass flow rate (mdot)				% flow rate	% uncertainty
Pa		Inch H2O		kg/s		lb/s			
Value	Uncertainty	Value	Uncertainty	Value	Uncertainty	Value	Uncertainty		
444.6	40.06	1.78	0.16	0.002285	0.000103	0.005038	0.000226	100.00	4.49
452.1	40.06	1.82	0.16	0.002305	0.000102	0.005082	0.000224	100.88	4.41
448.2	40.06	1.80	0.16	0.002295	0.000102	0.005060	0.000225	100.44	4.45
440	40.06	1.77	0.16	0.002274	0.000103	0.005013	0.000227	99.52	4.53
442.8	40.06	1.78	0.16	0.002281	0.000103	0.005029	0.000226	99.82	4.50
436.7	40.06	1.75	0.16	0.002265	0.000103	0.004993	0.000228	99.12	4.57
433.6	40.06	1.74	0.16	0.002257	0.000104	0.004976	0.000229	98.77	4.60
426.4	40.06	1.71	0.16	0.002238	0.000105	0.004934	0.000231	97.94	4.68
417.4	40.06	1.68	0.16	0.002215	0.000106	0.004883	0.000233	96.94	4.78
404.6	40.06	1.62	0.16	0.002181	0.000108	0.004808	0.000237	95.45	4.93
376.9	40.06	1.51	0.16	0.002105	0.000111	0.004641	0.000246	92.12	5.29
353.2	40.06	1.42	0.16	0.002038	0.000115	0.004493	0.000254	89.19	5.65
324.9	40.06	1.30	0.16	0.001955	0.000120	0.004310	0.000265	85.56	6.15
301.4	40.06	1.21	0.16	0.001883	0.000125	0.004151	0.000275	82.41	6.63
269.5	40.06	1.08	0.16	0.001781	0.000132	0.003926	0.000291	77.94	7.42
228.5	40.06	0.92	0.16	0.001640	0.000144	0.003616	0.000317	71.77	8.76
177.6	40.06	0.71	0.16	0.001447	0.000163	0.003190	0.000360	63.33	11.27
137.4	40.06	0.55	0.16	0.001273	0.000186	0.002806	0.000410	55.71	14.60
106.5	40.06	0.43	0.16	0.001121	0.000212	0.002471	0.000466	49.06	18.87
63.5	40.1	0.25	0.16	0.000865	0.000276	0.001908	0.000609	37.87	31.94
33.52	40.06	0.13	0.16	0.000629	0.000396	0.001387	0.000873	27.53	62.93

VITA

Tommy Hong

Candidate for the Degree of

Master of Science/Arts

Thesis: MEASUREMENTS OF FROST GROWTH ON LOUVERED FOLDED FINS OF MICROCHANNEL HEAT EXCHANGERS

Major Field: Mechanical Engineering

Biographical:

Tommy Hong, graduate research assistance at Oklahoma State University for two years. He has three years of experience in programming, designing, constructing, and collecting along with analyzing experimental data. Previously, he worked on construction of Low Temperature Psychrometric Chamber and currently working on experimental works to investigate frost growth on microchannel heat exchanger. Tommy has a bachelor's degree in Aerospace and Mechanical Engineering from Oklahoma State University. He was awarded Magna Cum Laude honarary and won second place in American Institute of Aeronautics and Astronautics (AIAA) Student Design/Build/Fly Competition organization.

Education:

Completed the requirements for the Master of Science in Mechanical Engineering at Oklahoma State University, Stillwater, Oklahoma in December, 2011.

Completed the requirements for the Bachelor of Science in Aerospace and Mechanical Engineering at Oklahoma State University, Stillwater, Oklahoma in May 2009.

Experience:

Employed by Oklahoma State University, Department of Mechanical and Aerospace Engineering, as a graduate research and teaching assistant from August 2009 to present.

Professional Memberships:

ASHRAE student membership

Name: Tommy Hong　　　　Date of Degree: December, 2011

Institution: Oklahoma State University　　　　Location: Stillwater, Oklahoma

Title of Study: MEASUREMENTS OF FROST GROWTH ON LOUVERED FOLDED FINS OF MICROCHANNEL HEAT EXCHANGERS

Pages in Study: 98　　　　Candidate for the Degree of Master of Science

Major Field: Mechanical Engineering

Scope and Method of Study:

Frosting tests were conducted on seven different microchannel heat exchanger geometries to investigate capacity degradation and rate of frost growth. Every fin sample was tested with three different fin temperature conditions with air entering the fin sample at 1.7°C (35°F) dry bulb temperature and wet bulb temperature of 0.6°C (33°F), which yield entering relative humidity of about 82% and absolute humidity of 0.0035 kg-water/kg-air. The air face velocity on fin sample at the beginning of the test was set to 1.5 m/s (295 fpm) for fin sample 1, 2, 3, 6, and 7. The air face velocity was varied at 0.8, 1.2, and 1.6 m/s (157, 236, and 315 fpm) on fin sample 4. Fin sample 5 face velocity was set to 1 m/s (197 fpm). Additionally, the effect of humidity content in the air was investigated on sample 4 where the humidity ratio was varied from 72% to 92%.

Findings and Conclusions:

The experimental results suggested that fin temperature and air humidity had a predominant effect on frost growth rate. Meanwhile, air velocity was peculiar and further investigations are recommended in the future. The frost tests on different fin geometries (fin height, fin depth, and fin density) recommended that folded flat fins seemed to have higher frosting time due to a lower heat transfer capacity when compared to folded louvered fins at the same fin temperature. Meanwhile, the effect of frosting time for different geometries were significant when the fin temperature is warmer in the experimental case is at -5°C (23°F). On the other hand, when the fin temperature decreased below -10°C (14°F) the effect of fin geometries on the frosting time became less significant. The impact of the frosting time and heat transfer rate is due to different fin geometries which are presented in this thesis.

ADVISER'S APPROVAL: Dr. Lorenzo Cremaschi